Identification of Mechanical Properties of Nonlinear Materials and Development of Tactile Displays for Robotic Assisted Surgery Applications

Siamak Arbatani

A thesis
in
The Department
of
Mechanical Engineering

Presented in Partial Fulfillment of the Requirements
For the Degree of Doctor of Philosophy
Concordia University
Montréal, Québec, Canada

April 2016

Concordia University
School of Graduate Studies

This is to certify that the thesis prepared

By: **Mr. Siamak Arbatani**

Entitled: **Identification of Mechanical Properties of Nonlinear Materials and Development of Tactile Displays for Robotic Assisted Surgery Applications**

and submitted in partial fulfillment of the requirements for the degree of

Doctor of Philosophy (Mechanical Engineering)

complies with the regulations of this University and meets the accepted standards with respect to originality and quality.

Signed by the final examining commitee:

Dr. Javad Dargahi	Thesis Supervisor
Dr. Saeed Sokhanvar	Co-supervisor
Dr. Mahdi Tavakoli Afshar	External Examiner
Dr. Amin Hammad	External to Program
Dr. Youmin Zhang	Examiner
Dr. Sivakumar Narayanswamy	Examiner

Approved _____
Chair of Department or Graduate Program Director

_____ 20 _____ _____
Rama Bhat, Ph.D.,ing., FEIC, FCSME, FASME, Interim Dean
Faculty of Engineering and Computer Science

Abstract

Identification of Mechanical Properties of Nonlinear Materials and Development of Tactile Displays for Robotic Assisted Surgery Applications

Siamak Arbatani, Ph.D.
Concordia University, 2016

This PhD work presents novel methods of mechanical property identification for soft nonlinear materials and methods of recreating and modeling the deformation behavior of these nonlinear materials for tactile feedback systems.

For the material property identification, *inverse modeling* method is employed for the identification of hyperelastic and hyper-viscoelastic (HV) materials by use of the spherical indentation test. Identification experiments are performed on soft foam materials and fresh harvested bovine liver tissue. It is shown that reliability and accuracy of the identified material parameters are directly related to size of the indenter and depth of the indentation. Results show that inverse FE modeling based on MultiStart optimization algorithm and the spherical indentation, is a reliable and scalable method of identification for biological tissues based on HV constitutive models.

The inverse modeling method based on the spherical indentation is adopted for realtime applications using *variation* and *Kalman filter* methods. Both the methods are evaluated on hyperelastic foams and biological tissues on experiments which are analogous to the robot assisted surgery. Results of the experiments are compared and discussed for the proposed methods. It is shown that increasing the indentation rate eliminates time dependency in material behavior, thus increases the successful recognition rate. The deviation of an identified parameter at indentation rates of $V =$ 1, 2 and 4 mm.sec^{-1} was found as 28%, 21.3% and 7.3%. It is found that although the Kalman filter method yields less dispersion in identified parameters compared to the variance method, it requires almost 900 times more computation power compared to the variance method, which is a limiting factor for increasing the indentation rate. Three bounding methods are proposed and implemented for the Kalman filter

estimation. It was found that the Projection and Penalty bounding methods yield relatively accurate results without failure. However, the Nearest Neighbor method found with a high chance of non-convergence.

The second part of the thesis is focused on the development of tactile displays for modeling the mechanical behavior of the nonlinear materials for human tactile perception. An accurate finite element (FE) model of human finger pad is constructed and validated in experiments of finger pad contact with soft and relatively rigid materials. Hyperfoam material parameters of the identified elastomers from the previous section are used for validation of the finger pad model. A magneto-rheological fluid (MRF) based tactile display is proposed and its magnetic FE model is constructed and validated in Gauss meter measurements. FE models of the human finger pad and the proposed tactile display are used in a model based control algorithm for the proposed display. FE models of the identified elastomers are used for calculation of control curves for these elastomers. An experiment is set up for evaluation of the proposed display. Experiments are performed on biological tissue and soft nonlinear foams. Comparison between curves of desired and recreated reaction force from subject's finger pad contact with the display showed above 84% accuracy.

As a complementary work, new modeling and controlling approaches are proposed and tested for tactile displays based on linear actuators. Hertzian model of contact between the human finger pad and actuator cap is derived and curves of material deformation are obtained and improved based on this model. A PID controller is designed for controlling the linear actuators. Optimization based controller tuning approach is explained in detail and robust stability of the system is also investigated. Results showed maximum tracking error of 16.6% for the actuator controlled by the PID controller. Human subject tests of recreated softness perception show 100% successful recognition rate for group of materials with high difference in their softness.

Acknowledgments

I would like to take the opportunity and greatly and deeply thank my supervisors, Professor Javad Dargahi and Doctor Saeed Sokhanvar, for their nonstop supports, suggestions and direction. I would like to thank them for all their contributions, guidance, remarkable ideas and encouragement. I would also like to thank members of my defense committee, Professor Youmin Zhang, Professor Narayanswamy Sivakumar and Professor Amin Hammad, who have helped me throughout my PhD program.

I also want to thank administrative, professional and technical staff at Concordia University: Leslie Hossein, Sophie Mérineau, Charlene Wald, Gilles Huard, Dan Juras, Robert Oliver, Peter Sakaris and Rudi Krueger.

Warm and heartful thanks go to all my friends and lab-mates at Concordia University: Masoud Kalantari, Roozbeh Ahmadi, Mehdi Ardavan, Ehsan Shareghi, Alireza Hassanbeiglou, Mostapha Marzban, Ehsan Zahedi, Masoud Razban, Amir Hooshiar and MohammadReza Rejali. Definitely, I could not have had better friends and colleagues.

My deepest heartfelt gratitude goes to my wife, Ladan Zamirian. She supported and encouraged me during my PhD study until I finish it; I am really grateful for having her in my life. I would also like to express my profound gratitude to my father Younes, my mother Roghi, and my brother Bobak. Words simply can not express my love for my family. They have been with me every step of the way and I could not have achieved it without them.

Lastly, I would like to thank Concordia University and whole staff for preparing such an environment and opportunity for me to carry on my studies to the doctoral level.

Contents

List of Figures

List of Tables

List of Symbols

Symbol	Meaning
U	Energy Density (J/m^3)
λ_i	Principal Stretches
J	Total Volume Ratio(Current Volume/Reference Volume)
J^{el}	Elastic Volume Ratio
J^{th}	Thermal Volume Ratio
ϵ^{th}	Linear Thermal Expansion Strain
μ_0	Initial Shear Modulus (Pa)
K_0	Initial Bulk Modulus (Pa)
ν_i	Poisson's Ratio
τ	Time (s)
G	Shear Modulus (Pa)
K	Bulk Modulus (Pa)
g_∞	Shear Modulus at Time Infinity (Pa)
k_∞	Bulk Modulus at Time Infinity (Pa)
f_{obj}	Objective Function
P_{FEM}	Indentation Force Calculated from the FE Analysis (N)
P_{Exp}^{meas}	Indentation Force Measured in Indentation Experiment (N)
f_t	Indentation Force Measured at Time t (N)
f_t^i	Indentation Force Calculated From i^{th} Combination of Material Parameters at Time t (N)
E	Error Vector
E_{th}	Threshold Error
x_n	A Posteriori State Estimate
x_{n-1}	A Priori State Estimate
H_n	Function of Exact Relation Between the State Parameters and and the Measured Variables
K_n	Kalman Gain Matrix
y_n	Noisy Observation
P_n	Measurement Covariance Matrix
R_n	Error Covariance Matrix
C_p	Penalty Coefficient
$\|B\|$	Magnetic Flux Density (T)
H	Magnetic Field Strength (A/m)
σ_y	Yield Strength (Pa)
F_r	Reaction Force (N)
K_P	Proportional Coefficient
K_I	Integral Coefficient
K_D	Derivative Coefficient
K_N	Filter Coefficient

List of Abbreviations

Abbreviation	Definition
HV	Hyper-viscoelastic
FE	Finite Element
MRF	Magnetorheological Fluid
PM	Permanent Magnet
PID	Proportional-Integral-Derivative
FDA	Food and Drug Administration
EMA	European Medicines Agency
SMA	Shape Memory Alloy
EAP	Electro-Active Polymer
MEMS	Micro-Electro-Mechanical Systems
VR	Virtual Reality
VE	Virtual Environment
MIRS	Minimally Invasive and Robotic Surgery
MIS	Minimally Invasive Surgery
MS	MultiStart
EVA	Closed Cell Ethylene-vinyl Acetate
B1	Closed Cell Sponge Neoprene
FGM	Functionally Graded Material
ICF	PVC/NBR Polymer
A2	Open Cell Polyether
LUT	Lookup Table
AWG	American Wire Gauge
ROI	Region of Interest
D/A	Digital to Analog Converter
A/D	Analog to Digital Converter
DAC	Data Acquisition Card
FSR	Force Sensing Resistor
PTF	Polymer Thick Film

Chapter 1

Introduction

Nowadays, development of tele-manipulation systems, e.g. robotic surgery, and virtual reality (VR) technologies in various fields, necessitates to equip them with improved interfaces (e.g., 3D vision and haptic feedback technology) which makes the human adoption effort as minimum as possible. The haptic feedback technology, which is introduced in the early 70s [1], is a touch feedback technology which takes the advantages of both tactile and kinesthetic feedback systems.

Kinesthetic receptors located in the muscles and joints, and tactile mechanoreceptors located in the glabrous skin, are parts of the human somatosensory system which percept the body motion and mechanical pressure or distortion respectively.

Traditional interfaces include visual feedback which is essential for a manipulation task but not sufficient. Efforts have been made in this regard to add the sense of touch to the human/machine interfaces. Accordingly, kinesthetic feedback is added to these interfaces, which delivers the force and torque feedbacks to muscles, tendons

and joints [2]. As a result, kinesthetic feedback makes the physical or virtual presence more immersive than only the visual feedback.

Although current kinesthetic feedback systems are mature and outperform human in kinesthetic perception [3], the kinesthesia is only a part of the somatosensory system, therefore it is not possible to render the complete sense of touch only by the kinesthetic feedback. A schematic hierarchy of the somatosensory system is presented in Fig. 1, which shows the kinesthetic and tactile feedbacks as sub-modality of the somatosensory system.

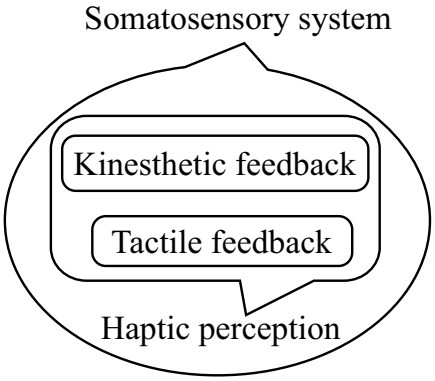

Figure 1: Hierarchy of the somatosensory system.

To assess the shape, size, texture and softness of physical and virtual objects which are necessary for accomplishment of complicated manipulation tasks in small workspaces and virtual environments (VE), tactile feedback as the other modality of the sense of touch, becomes necessary [4–6]. Impact of the tactile feedback in manipulation tasks have been widely investigated. Literature survey illustrates the effects of lack of the tactile feedback as underestimation of produced forces by muscles [4] and even opposite perception of the forces in absence of the tactile feedback [5, 6].

In tasks like grasping, the role of cutaneous receptors in adjusting the grip force is accurately studied [6, 7] and it is understood that in absence of the cutaneous or tactile feedback, the preliminary models of objects are no longer updated during the grasping task [6, 8].

Along with force perception, time synchronization and perception of transition between various phases of mechanical manipulation events (grasping, holding and discarding) are important. Mechanical events are determinant for control and planning of manipulation in human brain. Tactile feedback signals determine and categorize the various phases of mechanical events (actions) and mark the transition between them. Therefore, lack of contact information makes it difficult for brain to control the manipulation task smoothly. Contact information along with kinesthetic and vision are needed to obtain the body state and structure during a manipulation task [9, 10]. Timing is also important in various phases of dexterous manipulation tasks like grasping. It has been shown that lack of the tactile feedback affects duration of finger opening phase in grasping [11]. Elimination of tactile feedback prolongs the finger opening phase, and impairs grasping control as a result. It can be concluded that the tactile information is used in time optimization of various phases of manipulations tasks [12]. One step outward, the tactile feedback is tied to the real world activities, and is unavoidable component of human body's feedback system for dexterous movements.

State of the art research is mostly focused on critical applications of the tactile feedback. For example, grasping and pulling of soft tissues and detection of under

tissue vessels and anomalies by palpation in current robotic surgery systems are not satisfactory or even impossible due to the lack of tactile and kinesthetic feedbacks [13]. The issues due to the lack of force and softness feedbacks have been reported by experienced robotic assisted surgeons and have been suggested that providing even only force feedback would help in adjusting the forces applied on tissue during the robotic surgery [13].

Considering higher risk, long term training with VR facilities for new surgeons and exhausting operations due to continuous translation of hand movements only by visual feedback in the robotic surgery, integration of tactile and kinesthetic feedbacks (haptic feedback in general) to these devices would be the next step in this field. In order to alleviate the limitations of current VR/human and robot/human interfaces (including robotic assisted surgery, which is the main scope of this research work), various types of kinesthetic and tactile displays have been proposed and developed which are able to produce various tactile and kinesthetic modalities in limited workspaces with small instruments. Recently, integration of tactile and kinesthetic feedback devices is proposed as well [14]. An integrated multilevel feedback system consisting kinesthetic and tactile feedback beside three dimensional vision would be an ideal solution to address the current unimodal feedback systems.

Stimuli applied to the skin during palpation and perception of shape, texture and softness consists of a superposition of multiple components. Normal indentation

components stimulate slowly adapting type 1 (SA I) receptors[1], vibration stimulates rapidly adapting (RA) receptors[2] and lateral stretch stimulates SA II receptors[3] [15–17]. An ideal feedback device should be able to stimulate all types of mechanoreceptors in order to display spectrum of all the mechanical tactile modalities. Among various tactile modalities, those related to normal indentation (e.g. form and roughness) are of great interest for researchers of tactile feedback systems due to the ability of softness and 3D shape perception. Softness and shape perception are complex abilities which are originated from twisted kinesthetic and tactile perceptions. Palpation during an open surgery is done by the surgeon for detection of under tissue lumps and arteries. Therefore, it can be concluded that in the minimally invasive and robotic surgeries (MIRS) lack of the softness feedback weighs more than lack of the shape feedback.

[1]SA I receptors percept form and roughness on the skin.
[2]RA receptors percept flutter and slip on the skin.
[3]SA II receptors percept skin stretch.

1.1 Identification of Hyper-Viscoelastic Tissue by Inverse Indentation Modeling

Chapter 2 of the thesis deals with identifying the soft hyperelastic[4] and hyper-viscoelastic[5] constitutive model parameters by inverse modeling for use in FE modeling of biological tissues. MultiStart (MS) global optimization method is employed in the inverse modeling approach. The proposed method is tested on liver tissue as well as polymer based foams with nonlinear deformation behavior.

In this work, to reduce complexity of biological tissue testing, parameters of a suitable strain energy function for tissue like hyperelastic closed cell foams are identified in an inverse problem of indentation by employing a spherical indenter with relatively large depth of indentations. Then the proposed method is tested on liver tissue using a nonlinear HV material model. The problem is solved using MS global optimization approach which determines multiple starting points for optimization and reporting back the best locally optimal solution that it finds [18, 19]. In MS approach, first, map of objective function is produced and then the objective function is minimized using a Nelder-Mead simplex algorithm with initial estimates which are determined by minimum points in map of the objective function. Material parameters are then identified and evaluated based on the assumption of no Poisson's ratio effect and that there is no friction between the indenter and the material itself. Two main phases

[4]Hyperelastic constitutive model corresponds to ideally elastic material for which the stress-strain relationship is achieved from a strain energy density function. The hyperelastic material is explained in detail in section 2.2.

[5]Hyper-viscoelastic property is a combination of hyperelastic and viscous (time dependent) behavior. The viscoelastic behavior is explained in detail in section 2.3.

of the MS global optimization are presented in Figs. 2 and 3. Phase 1 is related to evaluation of the parameter space and phase 2 is selective local optimization step.

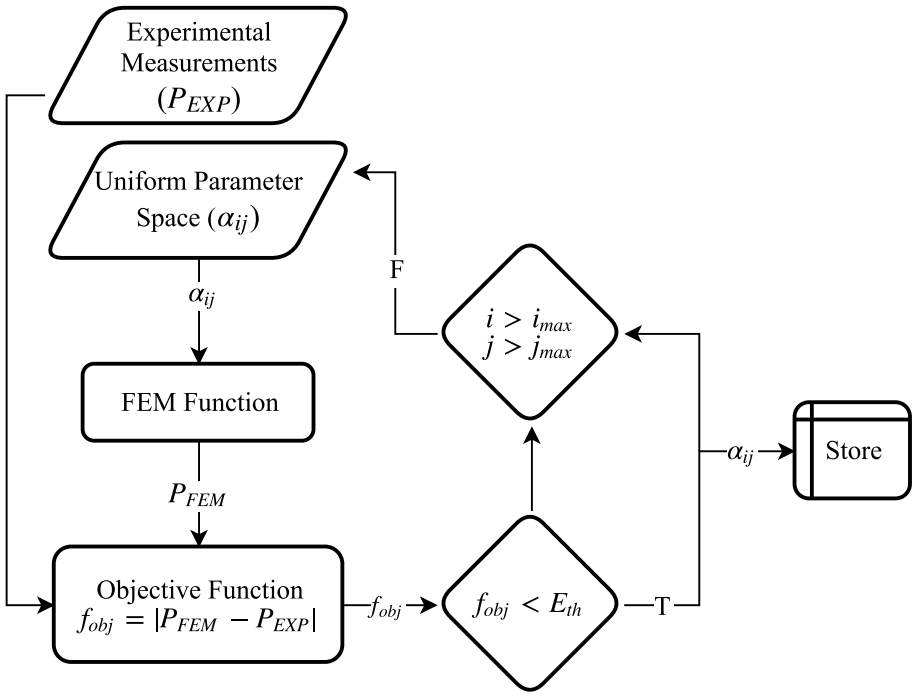

Figure 2: Flowchart of 1st phase of MS optimization for material parameter identification. Output of the objective function is compared with a desired threshold error value (E_{th}).

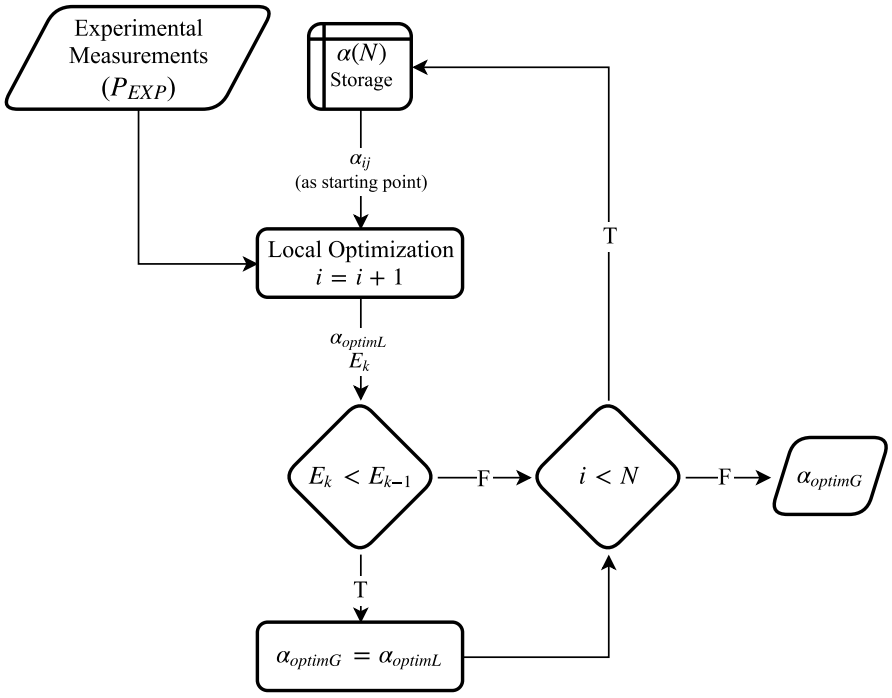

Figure 3: Flowchart of 2nd phase of MS optimization for material parameter identification. The optimal point from local optimization (α_{optimL}) with lowest optimization error value (E_k) is selected as the global optimum point (α_{optimG}).

Validity of the assumptions are evaluated with the proposed method as well. Sensitivity of the identified results to indenter size and indentation depth is studied and effect of these two parameters on identification results are discussed in detail.

Background

For medical applications, such as surgical simulation and recreation of tactile information during the robot assisted surgery and diagnostics, it is essential to obtain accurately the mechanical behavior of biological tissues [20, 21]. Soft tissues are nonlinearly viscoelastic and are usually modeled by variants of strain energy function [22,23].

Strain energy functions generally comprise several of the material's physical properties as well as parameters without any physical interpretation. Accurate identification of these parameters is often a challenging task. To determine these parameters, standard mechanical tests such as tensile, compression, shear and volumetric tests along with relaxation can be performed. Although these tests are repetitive, they require exacting control on sample geometry and test conditions. Furthermore, especially during the higher and maximum strain levels, physical restrictions may introduce errors in the test results. For example, friction in the compression test and strength of the adhesive at interface of the sample and loading plate during the shear test may cause bulging and give rise to erroneous test results. Demand in the engineering simulation field has led to utilization of optimization and state estimation algorithms within the simulation softwares for the purposes of design optimization and parameter identification by inverse modeling [24, 25].

Inverse modeling allows conversion of observed measurements of a physical system into constitutive parameters of its mathematical model [18]. Therefore inverse modeling of a well-defined mechanical test on a suitable mathematical model would result in acquiring optimum parameters which can be either standard material properties or those that are difficult to measure, such as friction.

Within various mechanical tests, the indentation test is of special interest for the parameter identification due to presence of intricate deformation. The indentation simulates compression and shear modes of deformation in a given sample at the same time [26]. Therefore, an inverse model of indentation test would guarantee parameter

retrieval through complex modes of deformation in such a sample. This is in contrast with controlled tests which are designed for generating either a particular stress or strain state in test specimens.

Inverse modeling, based on the indentation test, have been proposed and successfully employed for identification of linear and various nonlinear material models.

Nakamura et al. [27] introduced a technique based on the indentation test and Kalman filter for state (parameter) estimation of functionally graded materials[6] (FGMs). In this method, force or displacement of indentation is chosen as the parameters to be measured, and unknown parameters of material model are chosen as the state vector for the Kalman filter algorithm. To reduce computational cost, reference data source were generated from the FE model of indentation test by varying materials model parameters along with an interpolation algorithm. The Kalman filter algorithm estimates the optimum parameters of the material model and shows that there is only minimal difference between the FE model and instrumented indentation experiment. A similar procedure has also been successfully employed for identifying foam-based nonlinear material parameters by conducting the indentation test [28]. Although this method yields reliable material parameters, for material models with relatively higher number of parameters, the ratio of accuracy over computational cost would decrease because of the pre-evaluated and interpolated nature of reference data such as are observed during noisy measurements.

[6]In material science, functionally graded materials are characterized by variation in substructure or composition through bulk of the material.

Chen and Diebels [29,30] have employed spherical indentation along with the gradient based optimization algorithm for identification of hyperelasticity and viscoelasticity in small deformations. They have used Mooney-Rivlin and Maxwell models for modeling of the hyperelasticity and time dependency, respectively. They showed effectiveness of this method by measuring mechanical properties of extremely thin layers of viscoelastic polymers. Although the small deformation suffice for material parameter identification, some applications require material properties in large deformations such as tool tissue interaction in minimally invasive surgery. Severe geometric nonlinearity in large deformations would require calibration of the material model parameters in a broader range of deformation.

Zhang et al. [31] have thoroughly studied spherical indentation of hyperelastic soft materials. They have examined various constitutive models and established relations between the indentation load/depth and the initial shear modulus using the Hertzian contact model. They have also investigated the possibility of measuring other hyperelastic material properties using the inverse FE modeling, and existence, uniqueness, and stability of the solution based on Hadamard inverse function theorem [32]. They have shown that increasing the indentation depth may provide more reliable evaluation on hyperelastic material model parameters.

1.2 Real-time Soft Material Identification for Use in Minimally Invasive Robotic Surgery

In Chapter 3 of the thesis, a novel realtime parameter identification approach is proposed based on inverse finite element analysis and the mechanical test of indentation, which is, furthermore, suitable for real-time implementation. The idea behind this method is to calculate the mechanical parameters of tissue by using a parameter that is easy to measure, namely the indentation force. Among other mechanical tests, the indentation test is employed in this method due to its simplicity since only two parameters are measured and controlled. Also, because the indenter can be easily rolled on the surface of the contacted material, it can be used for continuous palpation.

As previously mentioned, direct implementation of inverse FE modeling methods are not practical for real time applications due to their high computation cost. Also, the need for measured parameters ahead of the calculations is also a limiting factor in real time applications. Therefore, in this research, pre-evaluated FE models are employed in order to overcome computation time barrier of the inverse FE analysis, for the application in real time parameter identification. Two methods are proposed for optimal parameter search based on calculating of the variance during the indentation and the Kalman filter method with its various parameter bounding algorithms. In this research, the proposed methods are explained in detail and implemented in a similar scenario to MIRS. Performance of the algorithms is evaluated statistically and presented in several experiments.

Background

Direct palpation in conventional surgery is fast, accurate and reliable for detecting the shape or consistency of any biological infrastructure, compared to the indirect feedback provided in current minimally invasive techniques that employs remote sensory and visual devices [33]. Changes in the stiffness, or Young's modulus, of soft tissue are closely related to its pathological state [34, 35] which can be quickly monitored by the surgeon using his/her sense of touch during the direct palpation. For instance, palpation is a standard monitoring procedure for detecting abnormalities such as tumors in and around all the major organs including the thyroid, prostate, breast, liver and pancreas [36]. According to some studies, one-third of all the breast tumors are detected by the palpation [37], and it is still the best way to detect liver tumors and metastasis by assessing the tissue softness [34, 38, 39]. As another example, in laparoscopic colectomy, lack of haptic feedback hugely limits the surgeon's performance when attempting to resection the colon and is also recognized as being the major cause of mishaps during operative procedures such as accidentally cutting arteries [40–44].

The absence of tactile and kinesthetic feedback is also the main drawback of MIRS operations which currently are in dire need of more accurate mechanical force feedback devices in order to confer a more realistic sense of touch to the surgeon's fingertips.

Advantageous, also, would be the advent of smart tools for graphical representation of tool tissue interaction or smart algorithms for identifying biological tissues

during surgical operations. Recent efforts have been made in the area of smart identification methods and tools. For instance, different palpation tools have been developed for obtaining nonlinear viscoelastic tissue parameters [45–48]. However, these and other proposed methods are still not suitable for real-time identification of the tissue parameters.

It can be debated that the state-of-the-art haptic feedback devices can recreate the sense of touch for the surgeon. A major technical challenge in the field of haptic feedback for MIRS systems is to provide sufficient haptic information to the surgeon without there being any compromise in maneuverability, dexterity.

Although direct palpation in an operating room is a qualitative method of diagnosis, in order to adopt the human ability of palpation in a smart algorithm that would be useful during the MIRS, the diagnosis should be performed quantitatively. However, since biological tissues possess nonlinear mechanical behavior, conventional mechanical tests (compression or tension) and properties (Young's modulus) would not be sufficient in themselves to identify or classify the pertinent tissues. For example, real-time tissue elastography is widely used for visualizing the tissue elasticity and classifying tissues based on standard schemes such as the Tsukuba elasticity score [49]. However, different scoring methods do not necessarily yield similar results and extraneous factors, such as the palpation rate and pressure, may well influence the elastography classification [50]. Researchers have shown that elastic models only approximate real soft tissue [51, 52]. In addition, the methods which are capable of accurately measuring the parameters of biological tissues are not compatible with

MIRS and, furthermore, real-time implementation of these methods is challenging in the realms of computation and mechanical complexity. For example, volumetric compression and tensile tests are not intra-operative friendly nor would it be computationally effective, at least for the purposes of real-time implementation, to perform a compression test and subsequent inverse modeling to determine the material properties.

1.3 Design and Model-Based Control of Magnetorheological Fluid-Based Softness Display

Chapter 4 presents the design and study of a magneto rheological fluid-based softness display. A high efficiency compact electromagnet design is presented which is capable of magnetically saturating the MR fluid used for softness recreation. The proposed display is simulated by using an FE model. Interaction of human finger pad with soft materials is modeled in order to achieve a proper control algorithm for the display. A control method is proposed for regulating the electrical current in the electromagnet of the softness display in order to mimic the mechanical behavior of nonlinear soft materials, in contact with a finger pad, by means of the MR fluid.

Background

In order to assess the shape, size, texture and softness of physical and virtual objects, it is often necessary to undertake complicated manipulation tasks in small workspaces

and VE. In order to accomplish this, it is necessary to employ tactile and kinesthetic feedback of which the impact and use of tactile feedback in manipulation tasks has been widely investigated. A survey of current literature illustrates the effects of lack of tactile feedback as underestimation, and even opposite perception of produced forces by muscles, due to the absence of tactile feedback [4–6]. In general, contact information along with kinesthetic and vision are necessary to obtain the body state and structure during a manipulation task [9, 10].

Research in the field of haptic feedback is mainly focused on the critical applications of tactile feedback. For example, anomalies exist in current robotic surgery systems when grasping and pulling soft tissues and attempting to detect arteries under tissue, due to the lack of proper tactile feedback. Indeed, this shortcoming has often been reported by experienced robot assisted surgeons [13]. Thus, in order to address this issue and to more accurately replicate tactile perception, an attempt to improve on various types of tactile displays have recently been made [14, 53].

This research work has shown the effect of finger pad deformation. This effect is considered in control of the proposed softness display based on a linear actuator [54]. Using the Hertz contact model, it has been shown that the finger pad deformation reduces magnitude of the force in force-displacement curves, which is used for controlling the linear actuator of the proposed tactile display (chapter 5 of this thesis). As a next step, compliance of soft material in contact with the finger pad is studied in this work. Within potential smart materials, MR fluid was of interest in this research for controlling both the contact force and contact area between the finger pad and

soft materials. An schematic of the proposed display system is presented in Fig. 4.

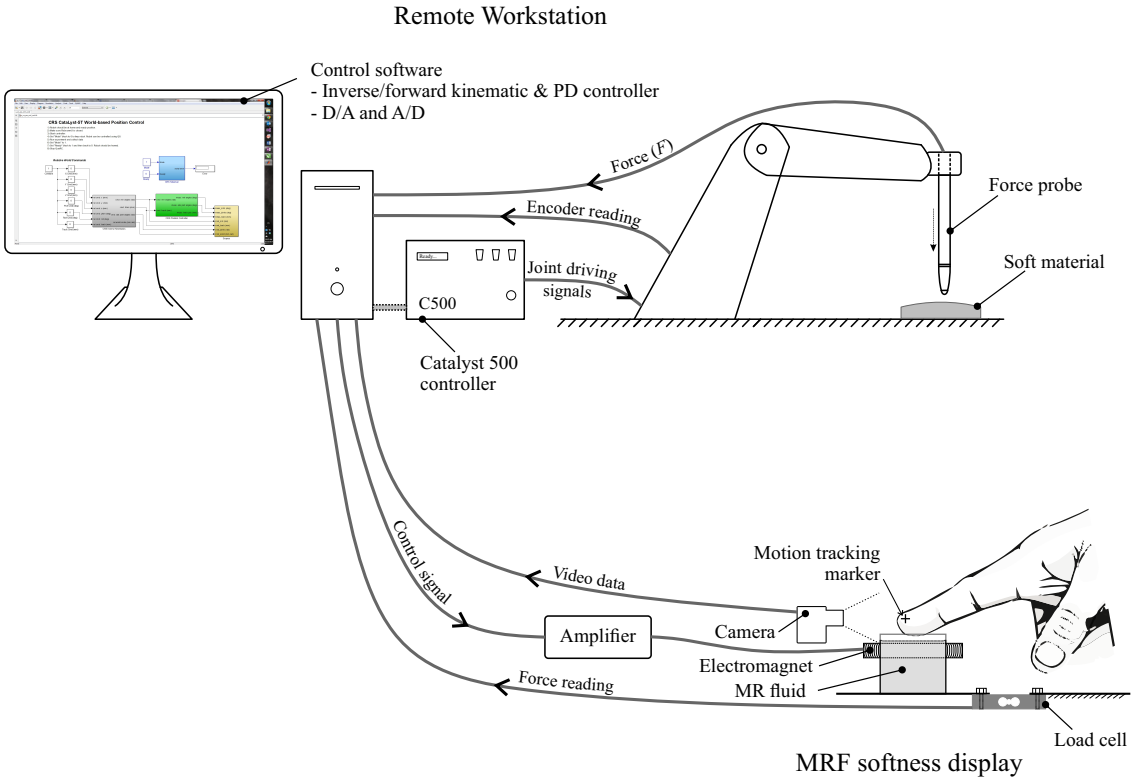

Figure 4: Schematic of the MRF base tactile display.

Applications of MRF in tactile feedback devices have been studied in literature. Sgambelluri et al. [55–58] studied the possibility of mimicking haptic perception by designing haptic interfaces based on MRF which are capable of reproducing the shape and compliance of virtual objects. They presented a few designs for their proposed device and modeled their designs by employing the FE method. An improved version of their developed device, called Haptic Black Box II (HBB II), consists of a plastic container for the MRF and a series of primary and secondary ferromagnetic cores positioned radially around and under the MRF container which dynamically adjusts the magnetic flux density inside the fluid. Their design allows precise control over

electrical current in coils and distance between the coils and the MRF container with a computer software. With this unique design, they have reported successful recreation of spatial shapes inside the MRF container by locally adjusting viscosity of the MRF.

In a recent research, Rizzo [59] proposed a combined system of permanent magnets (PM) to replace the excitation system (coils) in HBB II. Also, the plastic MRF container is replaced with a flexible balloon. In this design, the PMs and coils can be mechanically positioned using stepper motors which allows fine control of the magnetic field intensity inside the MRF. Stronger magnetic flux values were reported in the inner parts of the MRF as a result of using combined exciters.

1.4 Hertzian Model of Finger Pad Contact in Linear Actuator Based Tactile Display

Most tactile displays that have been introduced which are driven by a servomotor, or other type of linear actuator, use the spring model to simulate the softness. From a simplistic point of view, most materials can be modeled as a spring which, for small strains, is good for characterizing the softness of the material. However, in large deformations, the spring model cannot determine the behavior of the material with any exactness.

During the MIS, a surgical endoscope can apply large forces on tissues which results in a considerable amount of strain on those tissues. Based on the above facts, a tactile display system is proposed which takes the nonlinearity force-displacement

into account. This new tactile display comprises a linear actuator, a force sensor, and processing software. The system can reconstruct the softness of different materials based on the mechanical properties of those materials, and fingertip pulp deformation behavior. The data of the mechanical properties of the materials were measured and recorded. The effect of fingertip pulp deformation was applied to the material model and used by the processing software for reproducing the same properties by the tactile display. By calculating the dimension of the contact area, over which the force is applied, these stress-strain data can be transformed to force-compression which is used by the processing software to actuate the display. The data are saved in lookup table in the processing software which gathers information from the applied force to the shaft of a linear actuator and the position of the shaft. In conjunction with this information, and using the lookup table, the response of the material to the applied force is extracted from the table and used as the input to a PID controller which prepares necessary commands to the linear actuator to move the shaft. The experimental results showed that the developed tactile display can replicate the softness of materials very closely.

Chapter 5 is organized as follows. First, a description of the setup that we use for simulating the Young's modulus and softness display is presented. The the simulation algorithm is explained along with the PID controller, which is capable of reconstructing the tactile data. At the end, the experimental results are presented and discussed.

Background

Numerous research works have been undertaken on providing the surgeon with the means of applying force to sense softness, feel the pulse and detect abnormalities. The actuation technique is the key parameter of a physical tactile display which determines the whole system performance. For MIS and MIRS (minimally invasive robotic surgery) applications, the tactile display must conform to the medical device regulations imposed by the Food and Drug Administration (FDA) and the European Medicines Agency (EMA) while, at the same time, also meeting the physical requirements and other strictures that govern the safe and proper use of tactile displays in medical practice.

The minimum requirement of an ideal tactor (pin) type tactile display is that it must have a temporal resolution of 50 Hz, spatial resolution of 1 mm^{-2} and provide a minimum pressure of 50 $N.cm^{-2}$. Each actuator should be capable of indenting up to 4 mm with a height resolution of 10% (a power density of 10 $W.cm^{-2}$ with an actuator density of 1 per mm^2) [60–62]. The primary prerequisites for tactile displays for MIS and MIRS procedures, in order to make them suitable for integrating into current devices, are that they be small and quiet. In keeping with this, various actuation and stimulation techniques have been proposed. Pelrine et al. reported an electrostatic actuator composed of a polymeric elastic dielectric sandwiched between compliant electrodes [63]. In a similar design, Jungmann and Schlaak [64] used electrostatic actuators with elastic dielectrics as the tactile stimulator. By applying a voltage to the electrodes, the dielectric contracts in thickness and expands its area

due to the attracting charges on the electrodes. When the voltage is reduced, the dielectric returns to its initial shape and produce forces due to its stored elastic energy. One notable disadvantage of this actuator, certainly in medical applications, is its relatively high operation voltages (in orders of kilo Volts) which increases the risk of electrical interference in other devices. Yamamoto worked on a tactile display in which electrostatic force and friction control was employed in order to recreate surface roughness [65]. This device consisted of stator electrodes and a thin film slider upon which an aluminum conductive layer was deposited. The user places his index finger on the slider and moves it horizontally to obtain a certain tactile sensation. By applying various voltage patterns to stator electrodes, various friction distributions are generated on the slider which, in turn, is transferred to the fingertip so as to generate a surface roughness sensation which, therefore, makes it applicable only for surface roughness perception. Even though the main objective of a tactile display in medical applications is to recreate softness and contact force during the surgery, roughness feedback is also relevant in MIRS (e.g., gentle grasp with just enough pressure to avoid slip).

Ottermo et al. worked on fabricating a shape display using micromotors on the handle of an endoscopic grasper. They employed a 35 mm $\times$ 10 mm array of 15 $\times$ 4 piezoelectric sensors, in conjunction with a tactile display consisting of thirty-two micro motors, having a total size of 27 mm $\times$ 20 mm $\times$ 18 mm [66, 67]. This design, however, was limited by virtue of the fact that the actuator shaft was relatively large which decreased the tactor density in this display. Furthermore, the limited

force capacity of the actuators also restricted the ability to regenerate the mechanical deformation behavior of hard biological tissues. Wellman et al. used shape memory alloy (SMA) as the actuating element for a tactile shape display [68]. A 3D shape display, using an array of bars actuated by the SMA, is presented in [69]. Despite its many advantages in medical applications, SMA based actuators suffer from non-linear behavior and hysteresis during loading and unloading cycles. Hayward et al. [70] worked on a tactile display using an array of piezoceramics which stimulates the skin in its lateral mode by vibrating two active piezoelectric layers, also known as a bimorph. In another research work, Yun et al. [71] described the development of a piezoelectric based planar-distributed tactile system that only displayed textures. This proposed tactile display comprised a 6×5 pin array, actuated by thirty piezoelectric bimorphs. Another tactile stimulation method was proposed by controlling the suction pressure [72–74]. This method is based on the tactile illusion that we feel when something like a stick pushes up into the skin surface when we pull skin through a hole by lowering the air pressure.

In [75], a tactile display is proposed utilizing thermo-pneumatic micro pumps and micro valves which works based on sealed cavities in which one side is flexible. Each cavity is filled with a low boiling point liquid, such as methyl chloride, with a resistive heater built inside. When the heater increases the temperature inside the cavity, the pressure increases because of the gas resulting from the liquid-gas phase transition and the flexible side of the cavity becomes swollen [76, 77]. Though this design is simple and has many advantages, the response time in this actuation method

is long. In [78, 79] an electrocutaneous display is presented which directly stimulates sensory receptors within the skin with electrical current. An array of 5×6 electrodes is developed for generating pressure or vibration patterns without using any mechanical type of actuator.

Yamamoto et al. [80] developed a graphical overlay technique to display the location of hard objects hidden in soft tissue. While the phantom tissue is palpated using a surgical robot, the stiffness of a Hunt-Crossley model is estimated. At the same time, a visual overlay is created on a semi-transparent disc at the tissue surface by using hue-saturation-luminance. The hue corresponds to the stiffness at a palpated point and the saturation is calculated based on the distance from this point. Kalantari et al. [81] developed a 3D graphical tactile display for determining the presence of localized lumps. Their proposed algorithm reads the pressure distribution from 3×3 PVDF sensor arrays mounted on both jaws of a laparoscopic grasper and renders pressure distribution in three engineering views making the operator capable of detecting features that are hidden under the tissue. Graphical tactile displays that provide the surgeon with pressure distribution of contacted tissue are easy to implement on current MIS and MIRS devices. However, because such displays are based on indirect feedback through vision, they are therefore less efficient than direct stimulation. In [82], a tactile display device is designed based on the soft-actuator-based wearable technology. This device can provide stimulation on the human skin without any mechanical transmission. An electroactive polymer is used for the construction of the tactile display device. Another work which has been developed is a

pneumatically-driven balloon actuator array suitable for mounting on robotic surgical master controls [53, 83]. The inflation of hemispherical balloons increases the force on the skin and causes skin deformation. The actuator consists of an array of balloons formed from a spin coated silicone film placed over a molded substrate. Because it is small and fast due to its pneumatic driven mechanism, this display is suitable for MIS and MIRS applications despite the less than ideal shape of its pins (tactors) and non-uniform contact area. In [84] Kim et al. developed a multi-fingered tactile display module in which each comprises a 4×4 piezoelectric ultrasonic actuator array. Various types of texture information can be generated using a static indentation or through the vibration of each pin. In [85], Kimura et al. presented a 2-DOF (Degrees of Freedom) controlled softness display, capable of recreating the asymmetric softness of the contact area. Their proposed display consists of a flexible sheet as the contact surface and two DC motors which independently control the height of both sides of the flexible sheet and, consequently, the contact area. Liu [86] developed a real-time softness display by controlling the deformable length of an elastic beam element. Burch and Pawluk [87] presented a 2-D multifinger tactile display employing piezoelectric actuators as both contact and stimulator elements on each fingertip to reproduce and represent texture images. Cameron et al. [88] presented an electroactive polymer-based tactile display. They employed an Electro-Active Polymer (EAP) in the form of a cantilever to produce light touch through bending force and vibratory sensations to the fingertips by varying the sinusoidal waveform. In [89], a compact and wearable 3-DOF tactile display was developed and affixed on the fingertip. It was comprised

of two main parts, one fixed part on the backside of the finger which supported three DC motors, and the other active part on the fingertip which consisted of three wires whose lengths and strains were controlled by three DC motors. Watanabe et al. [90] proposed a tactile display using large displacement Micro-Electro-Mechanical Systems (MEMS) actuator arrays in which each was composed of a piezoelectric actuator and a hydraulic displacement amplification mechanism to achieve the minimum required stroke length of a tactile display element.

Small workspace on MIRS master controls and sensitive electrical instruments limit the number of tactile display technologies suitable for this application. Considering the current design of robotic surgical systems, only fast and small softness displays with a safe operational voltage and magnetic field would be suitable. Therefore, actuation techniques such as dielectric polymers, SMA, piezoelectric and electroactive polymers generally are not a good candidate for MIRS applications.

Chapter 2

Identification of Hyper-Viscoelastic Tissue by Inverse Indentation Modeling

Recently, in order to identify unknown parameters of a material, inverse FE modeling has been proposed and vastly employed [32, 91, 92]. Inverse modeling, within the context of material parameter identification problems, is an approach which attempts to achieve the most accurate model parameters with respect to fundamental physical experiments such as, for example, fitting the FEM numerical results to identical data from physical experiments.

In order to construct an accurate mathematical model of a biological tissue, it is necessary to thoroughly understand the nonlinear mechanical behavior of the tissue. In addition to the mathematical model (type of the strain energy function), accuracy

of the model directly depends on the identified material parameters. In this research work, inverse FE modeling technique is employed for identification of biological tissue with HV model and nonlinear elastic materials with hyperelastic model.

To investigate the effectiveness of this approach, the mechanical behavior of tissue-like polymeric foams as well as liver tissue have been studied. The liver tissue possess hyper-viscoelastic behavior, and the tested foams possess hyperelastic behavior which exhibits many of the features of biological tissues. The parameters of suggested hyperelastic and HV models are identified in an inverse problem of spherical indentation test.

An MS global optimization approach is employed based on the Nelder-Mead algorithm and the performance of this method is evaluated and compared to other alternatives such as the Kalman filter method and single element inverse FE models. Sensitivity of the results to parameters of indenter size and indentation depth is studied, and a hypothesis is proposed for prediction of variation in results due to changes in these parameters. Results showed that the employed MS global optimization approach produced accurate results with reasonable computational cost in comparison to single element model methods and pre-evaluated objective function methods such as the Kalman filter method.

2.1 Parameter Identification of Hyperelastic and Hyper-Viscoelastic Material Models by Inverse Modeling

As mentioned, accuracy of any FE model is strongly dependent upon not only the type of constitutive model used, but also on the accuracy of its parameters. Therefore, determination of material parameters through mechanical tests is a key step to provide data for the simulation of complex loading conditions. Many material constitutive models involve parameters often without physical meaning since they are not directly measurable. Therefore, indirect methods, like optimization, are required for identification of these parameters. For example, the Hyperfoam[1] strain energy potential function for foams involves the parameter α which has no physical definition and only specifies the shape and behavior of the stress/strain curves. It is necessary to perform an optimization to identify the parameter α for the Hyperfoam material model. Another example is parameters related to viscoelastic behavior definition by Prony series. Ratios of bulk and shear relaxation modulus, as well as the relaxation time constant can only be identified in a curve fitting or optimization operation on relaxation experiment data. Measurement of combined hyperelastic and viscoelastic or HV material model parameters in a simple single step experiment is almost impossible. In the following subsections, two suitable models for hyperelastic

[1]Hyperfoam is a type of hyperelastic strain energy function, which is suitable for modeling the soft foams

and viscoelastic behaviors are explained, next a method of parameter identification is proposed based on the inverse FE modeling for obtaining the HV model parameters in a single experiment.

2.2 Hyperelastic Behavior

High non-linear behavior of elastomeric foams and biological tissues is usually modeled using strain energy potential functions which define the strain energy stored in the material per unit of reference volume (volume in the initial configuration) as a function of the strain at that point in the material. Two most common strain energy functions used for foams and biological tissue are Hyperfoam and Ogden functions as shown in Eqs. 1 and 2, respectively:

$$U = \sum_{i=1}^{N} \frac{2\mu_i}{{\alpha_i}^2} \left[\hat{\lambda}_1^{\alpha_i} + \hat{\lambda}_2^{\alpha_i} + \hat{\lambda}_3^{\alpha_i} - 3 + \frac{1}{\beta_i} \left(\left(J^{el}\right)^{-\alpha_i \beta_i} - 1 \right) \right] \tag{1}$$

$$U = \sum_{i=1}^{N} \frac{2\mu_i}{{\alpha_i}^2} \left(\hat{\lambda}_1^{\alpha_i} + \hat{\lambda}_2^{\alpha_i} + \hat{\lambda}_3^{\alpha_i} - 3 \right) + \sum_{i=1}^{N} \frac{1}{D_i} \left(J^{el} - 1 \right)^{2i} \tag{2}$$

where energy density, U, is a function of temperature-dependent material parameters $\mu_i, \alpha_i, \beta_i, D_i$, principal stretches λ_i, and the elastic volume ratio, J^{el} . The following relationship exists between $\hat{\lambda}_i$, J^{el} and the thermal volume ratio J^{th} as shown in Eq. 3:

$$\hat{\lambda}_i = \left(J^{th}\right)^{\frac{-1}{3}} \lambda_i \rightarrow \hat{\lambda}_1 \hat{\lambda}_2 \hat{\lambda}_3 = J^{el} \tag{3}$$

According to Eqs. 4 and 5, the elastic volume ratio, J^{el}, is related to the total volume ratio, J, and the thermal volume ratio, J^{th} as shown:

$$J^{el} = \frac{J}{J^{th}} \tag{4}$$

$$J^{th} = \left(1 + \epsilon^{th}\right)^3 \tag{5}$$

where, ϵ^{th} is the linear thermal expansion strain. The coefficients μ_i are related to the initial shear modulus, μ_0, by:

$$\mu_0 = \sum_{i=1}^{N} \mu_i \tag{6}$$

β_i and D_i in the same manner are related to initial bulk modulus,K_0 , as shown in Eqs. 7 and 8:

$$K_0 = \sum_{i=1}^{N} 2\mu_i \left(\frac{1}{3} + \beta_i\right) \tag{7}$$

$$K_0 = \frac{2}{D_1} \tag{8}$$

β_i determines the degree of compressibility and is related to Poissons ratio, ν_i, as shown in Eq. 9:

$$\beta_i = \frac{\nu_i}{1 - 2\nu_i} \tag{9}$$

Closed cell foams are considered fully compressible, therefore parameters ν_i and consequently β_i are almost zero [93]. The validity of this assumption is investigated in section 2.10 of this research using the inverse modeling.

2.3 Viscoelastic Relaxation Behavior

Viscoelastic materials can be modeled by different rheological models. One of the basic rheological model is generalized Maxwell model or Prony series. This model, along with the potential energy functions, like Ogden function, allows modeling of large strain effects in a wide variety of nonlinear viscoelastic materials. Time dependent shear and bulk moduli in this model are shown in Eqs. 10 and 11:

$$G(\tau) = G_0 \left(g_\infty + \sum_{i=1}^{N_G} g_i e^{-\tau/\tau_i^G} \right) \tag{10}$$

$$K(\tau) = K_0 \left(k_\infty + \sum_{i=1}^{N_k} k_i e^{-\tau/\tau_i^K} \right) \tag{11}$$

where G and K are functions of shear and bulk modulus over time, τ is current time, G_0 and K_0 are shear and bulk modulus at time ($\tau = 0$), g_i and k_i are relative moduli related to term i, g_∞ and k_∞ are moduli related to time infinity. Assuming that the two deformation modes, bulk compression and shear strain, are closely related and relaxation occurs equally and simultaneously for both of the modes, then the relaxation times, τ_i^K and τ_i^G, would be equal [94]. The parameters, g_i, k_i and $\tau_i = \tau_i^G = \tau_i^K$ can be identified using a relaxation test and subsequent curve fitting, and

the parameters g_∞ and k_∞ can be identified at time $\tau = 0$ using the Eqs. 10 and 11 as shown in the following:

$$G_0 = G_0 \left(g_\infty + \sum_{i=1}^{N_G} g_i \right) \tag{12}$$

$$K_0 = K_0 \left(k_\infty + \sum_{i=1}^{N_K} k_i \right) \tag{13}$$

All the parameters of Prony series for Viscoelastic behavior can be obtained in standard relaxation tests by applying a sudden strain and measuring the stress over time.

2.4 Parameter Identification by Inverse Modeling

As mentioned, conventional determination of the hyperelastic and viscoelastic material parameters was carried out using standard mechanical tests which defines and guarantees formation of particular stress/strain fields on the test samples. Using these fundamental mechanical test results and single-element FE models, parameter determination was performed by means of simple curve-fitting methods [95] in commercial FE analysis software such as Abaqus [93]. However, standard mechanical tests require careful sample preparation to ensure formation of desired stress/strain fields in the sample. It has been shown that inverse problem theory can be employed for material parameter identification by modeling a specified experiment in full scale instead of scaling down to single-element models [96]. A general scheme to achieve material properties using inverse modeling is illustrated in Fig. 5. As shown in this

figure, in a problem of error function minimization, an optimizer finds the best set of parameters to satisfy a stopping criteria. The error function is defined as being the difference between experimental measurements and identical parameters in the mathematical model of that experiment.

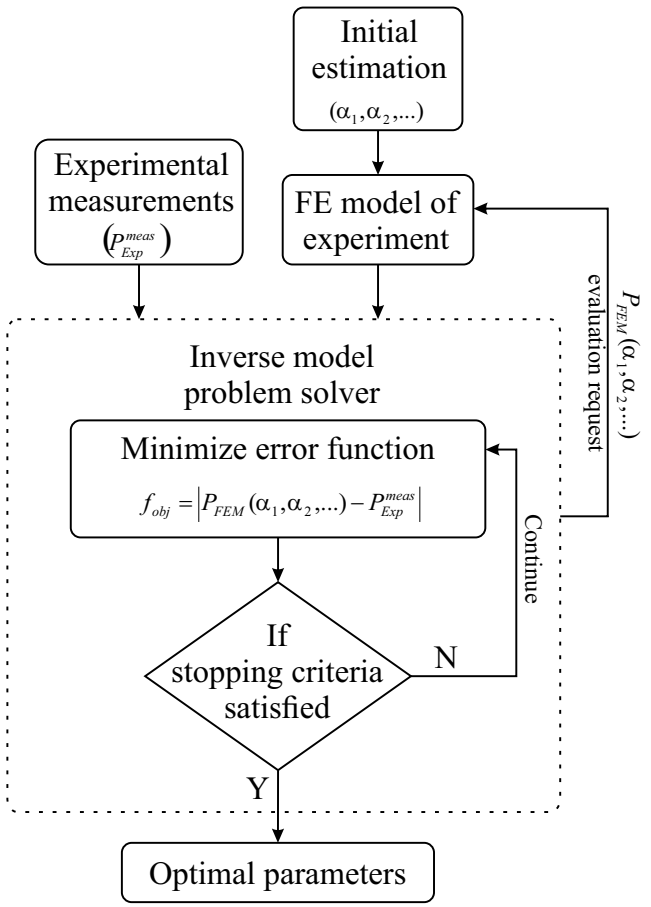

Figure 5: Inverse modeling parameter identification flowchart. α_i are optimization variables. P_{FEM} and P_{Exp}^{meas} are, respectively, scalar output of FEM and its counterpart from the experiment.

As instances of parameter identification by the inverse modeling, Schnur and Zabaras [97] combined an optimization code with a FE code for determining elastic

material properties. Gelin and Ghouati [98] coupled the code of a modified Levenberg-Marquardt method to an FE model. This was undertaken in order to determine the viscoplastic material parameters of aluminum alloys by minimizing the difference between the measured boundary displacement and the displacements calculated by the FEM.

Recently, with the advent of new optimization algorithms and FE modeling tools, in conjunction with improvements in computing power, new methods of identification by inverse modeling are widely being investigated and employed. Software packages such as Abaqus and LS DYNA are equipped with optimization modules although these modules are still only in the early development stage [24]. Also, third-party additions such as HEEDS MDO have recently been introduced in order to improve the inverse modeling capabilities of FEM packages.

2.5 MultiStart Global Optimization Approach

Computational cost is very important in applications such as parameter identification by the inverse FE modeling, where evaluating the objective function becomes computationally demanding. Therefore, the employed optimization algorithm should be more efficient in terms of parallelizability and the number of evaluations for achieving a result with reasonable accuracy. Within the context of mathematical optimization, local optimization methods are least computationally demanding. However these methods result in local minima which might not be same as global optimum point.

On the other hand there are global optimization methods which yield global optimum point, but with many number of evaluations on objective function. In order to achieve an adjustable trade-off between the computation cost and probability of the global solution, the MS method is employed in this research. The employed MS method generates uniformly distributed points in parameter space. Then the objective function is optimized using local optimizers with the generated points as initial points of the local optimizers. The main advantage of MS method is its high potential for parallelization. Both the steps of generating uniform parameter space and optimizing by means of local optimizers can be efficiently parallelized.

In this research, Nelder-Mead optimization approach is employed as the local optimizer for the MS global optimization method. The Nelder-Mead approach [99] belongs to class of direct search methods [100] and is very well known for its simplicity, low storage requirements and low number of function evaluations per iteration. This Nelder-Mead, or downhill simplex method, is usually used for minimizing a function with n variables, based on replacing the vertex with highest value of a general simplex with another point and examining the updated set of $(n + 1)$ vertices in n dimensions. Generally, this method is used for nonlinear optimization. Details of the Nelder-Mead optimization method is presented in Appendix A

2.6 Indentation Test

Of all the different conventional mechanical test methods, the indentation test is the simplest test to perform since it contains the least number of parameters that require to be measured. However, standard indentation tests only result in hardness of sample which is not, itself, an analytical mechanical property of the material and cannot be used for FE analysis. Several mathematical approaches have been proposed for determining a variety of material properties by indentation tests [101–104]. However, there is no general analytical method for identifying different properties using these tests. As mentioned earlier, inverse modeling can be used to extract the parameters of a material in a given constitutive model. In this study, indentation with spherical indenters is modeled by FE method as an analytical rigid indenter along with hyperelastic and HV materials, as shown in Fig. 6. The model is constructed in Abaqus CAE software using 4-node axisymmetric quadrilateral elements (CAX4R). Abaqus' explicit dynamic procedure along with Penalty contact algorithm are employed for solving the problem. The explicit dynamic procedure is based on Lagrangian FE formulations [105–108], which is suitable for problems involving large deformations and displacements. These formulations have been successfully applied to a broad range of nonlinear transient dynamic problems. An overview of the Lagrangian formulation is presented in Appendix B.

Indentation experiments were performed on closed cell foams and bovine liver tissue with two different indenter radiuses of $r = 4$ and 6 mm at constant indentation

rate of 1 mm.s^{-1}. An ElectroForce 3200 all-electric test instrument was employed to perform the indentation tests with displacement feedback and a sampling rate of 50 Hz. The schematic of the test setup is illustrated in Fig. 7. Indentation is performed up to a depth of 4 mm and the indentation force is acquired. Test results are presented in Fig. 8.

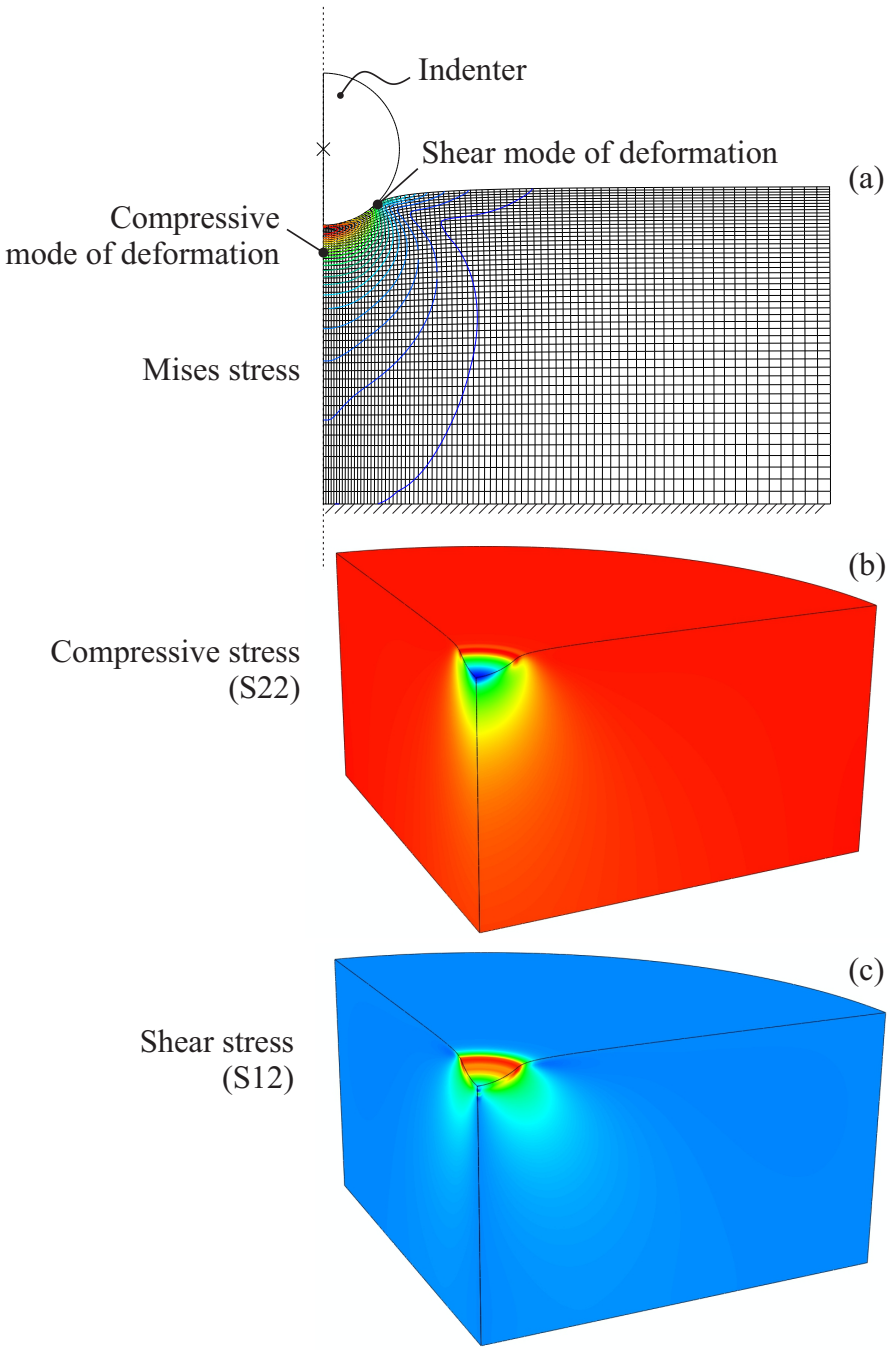

Figure 6: (a) Axisymmetric FE model of indentation is constructed using Abaqus FEM software using 4-node bilinear axisymmetric quadrilateral elements (CAX4R) for bulk material and an analytical rigid body for the indenter. Two dominant modes of deformation, (b) compressive and (c) shear, are shown in this figure.

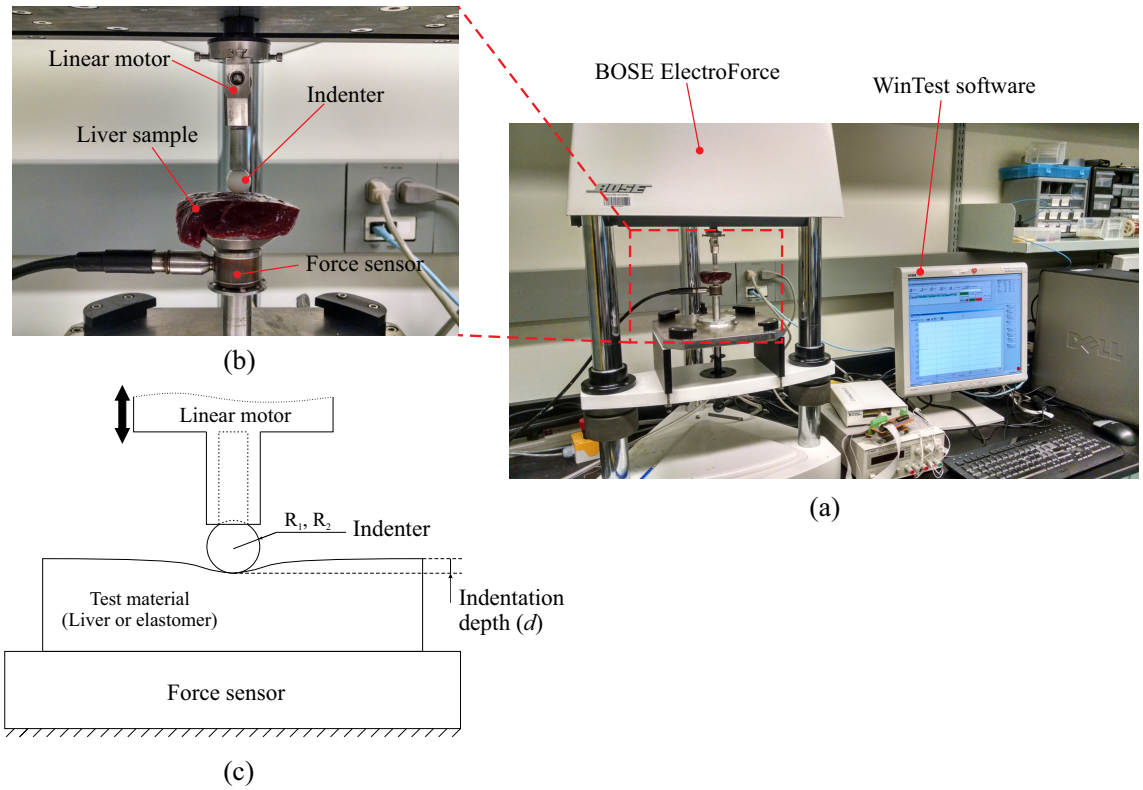

Figure 7: Indentation test setup. (a) A Bose ElectroForce 3200 test instrument is used for indentation experiments along with WinTest software for data acquisition. (b) Details of the test setup including liver sample, spherical indenter, force sensor and linear motor. (c) Schematic of the test setup.

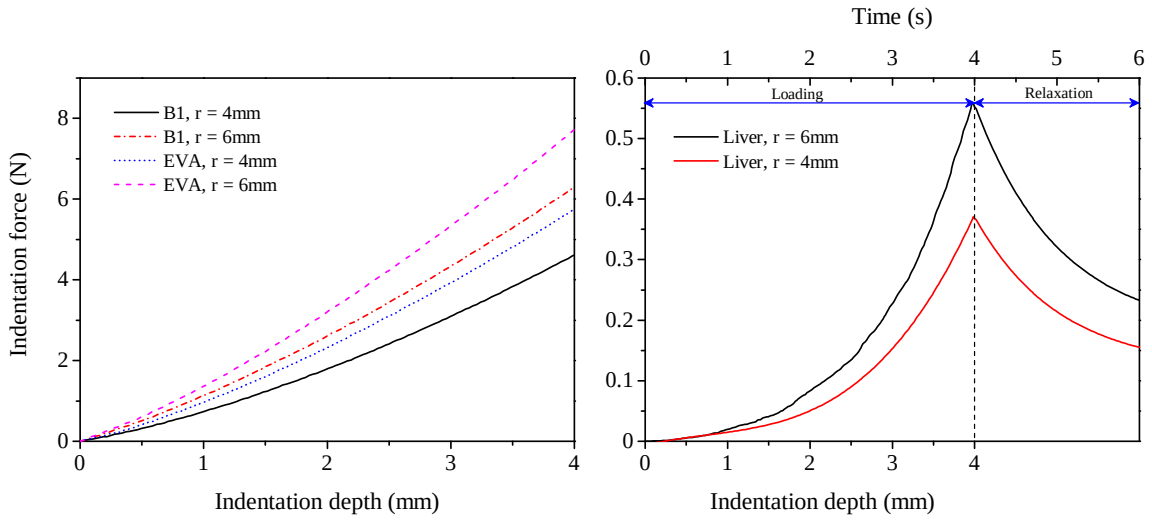

Figure 8: Indentation test results of closed cell ethylene-vinyl acetate (EVA), closed cell sponge neoprene (B1), products of PROFOM Canada, and bovine liver tissue. Indentation is performed with indenters of $r = 4$ mm and 6 mm radius. An average of three measurements is taken for each indentation test. An additional relaxation step is considered for the liver sample.

2.7 Objective Function and Global Evaluation

In order to identify the constitutive model parameters of elastomers in an inverse modeling problem, the error function is defined as shown in Eq. 14:

$$
\begin{aligned}
& f\left(\alpha, \mu, D, g, k, \tau, \right) = \sum\nolimits_{d_j} \sum\nolimits_{t=1}^{N} \left| P_t^{FEM}\left(\alpha_i, \mu_i, D_i, g_q, k_q, \tau_q\right) - P_t^{meas} \right| \\
& \alpha_i = \alpha_1, ..., \alpha_n \quad , \quad \mu_i = \mu_1, ..., \mu_n \quad , \quad D_i = D_1, ..., D_n \\
& g_q = g_1, ..., g_p \quad , \quad k_q = k_1, ..., k_p \quad , \quad \tau_q = \tau_1, ..., \tau_p \\
& j = 1, ..., m
\end{aligned}
\tag{14}
$$

where n is order of the strain energy function, p is order of the Prony series, m is number of spherical indenters used with different diameters, t is time of data collection,

P_t^{meas} is measured load in indentation test, P_t^{FEM} is calculated load in FE model of indentation, N is number of time steps and d_j represents diameter of the indenter. In this work, the strain energy functions with orders of $n = 1$ and 2 are studied. In order to consider a reasonable range of strain during the identification process, and acquire enough data points in indentation experiment, the indentation test was carried out up to depth of 4 mm (80% strain in elements around contact area) with a sampling rate of 50 Hz. Therefore, with the indentation rate of 1 mm.s^{-1}, a total number of 200 data points (N in Eq. 14) were acquired in both the experiment and the FE model of indentation.

2.8 Identification of Hyperelastic Model for Foams

The error function (Eq. 14) is evaluated in whole parameter space (combination of μ_i and α_i). Color maps of the objective function with two and four parameters (μ and α), as well as single and double indenters ($m = 1$ and 2 in Eq. 14) are presented in Fig. 9 and Fig. 10. These maps are plotted by evaluating the error function in a 12×12 grid of (α, μ) for first order energy function ($n = 1$) and $4 \times 4 \times 4 \times 4$ grid of $(\alpha_1, \mu_1, \alpha_2, \mu_2)$ for the second order energy function ($n = 2$) in reasonable ranges for α and μ. The global search over whole parameter space is performed systematically using the Nelder-Mead algorithm by following steps:

(a) Evaluation of the error function at user defined grid points of the parameter space.

(b) Determination of a threshold for error value (E_{th}) in order to identify candidate initial points for local optimizations.

(c) Identification of initial points based on the threshold value determined at step (b).

(d) Local optimizations using Nelder-Mead algorithm with identified initial points at step (c).

(e) Comparing and validating the optimized parameters.

Local optimizations using the Nelder-Mead method were performed with various initial points around possible regions of valid material parameters. In Fig. 9a and 9b, it can be observed that all the local optimizers converge to a unique point on the parameter space in ($n = 1$) case (two unknown parameters), but stationary points are not identical for different indenter radii. For example, as shown in Table 1 the initial shear modulus, μ_0, for EVA foam is identified as 0.22 MPa and 0.27 MPa when using indenters having radii of $r = 4$ and 6 mm, respectively. In order to resolve this discrepancy, an identification process is performed using two different indenter radii ($m = 2$) simultaneously.

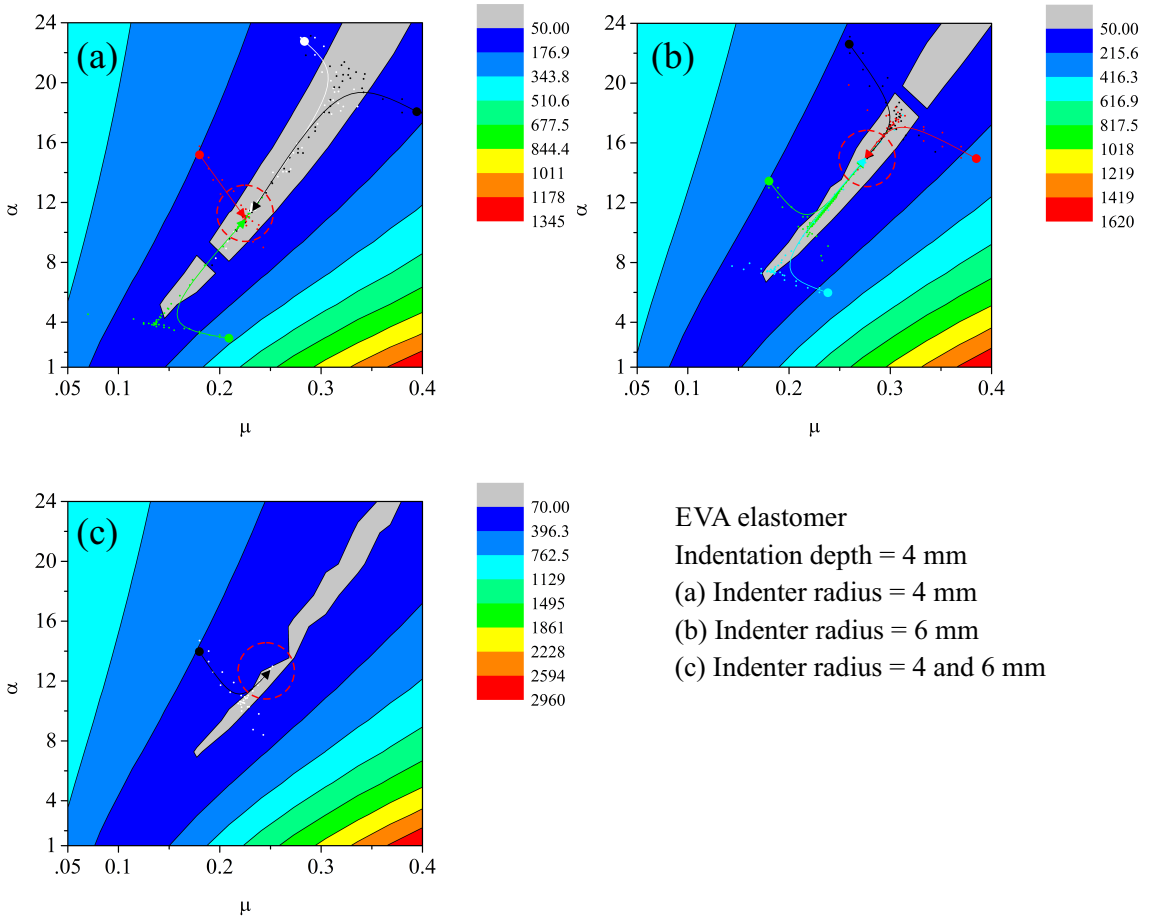

Figure 9: Color map of objective function using EVA and B1 elastomers. Optimization is performed from various starting points. Arrowed lines with various colors represent path of the optimization for each of the starting points. Relative error in the objective function acceptable for convergence (f_{tol}) is set to $f_{tol} = 10.0$ for local optimizations based on the Nelder-Mead algorithm.

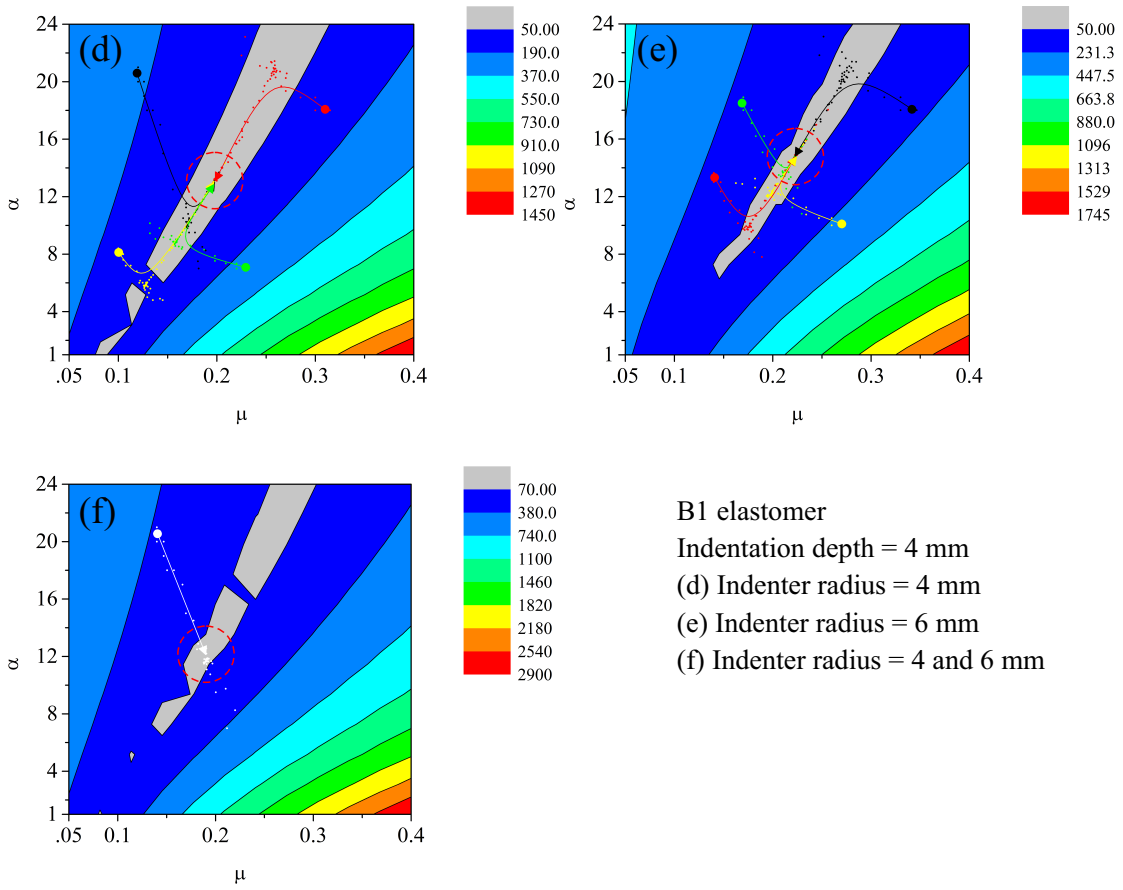

Figure 9: cont'd.

Table 1: 1st order Hyperfoam model ($N = 1$ in Eq. 1) parameter identification results for EVA and B1 foams. The indentation experiment was performed with two indenter radiuses, $r = 4$ mm and $r = 6$ mm in which the identification was performed using a single indenter and double indenter.

	EVA		B1	
Indenter radius (mm)	μ_s	α_s	μ_s	α_s
$r = 4$	0.220	10.526	0.193	12.711
$r = 6$	0.278	15.152	0.226	15.173
$r = 4$ and $r = 6$	0.245	12.424	0.188	11.1564

The color map of the objective function in Eq. 14 (with first order strain energy function, thus with two variable parameters ν and α) is shown in Fig. 9. Fig. 9a and 9b, respectively, shows EVA elastomer compressed by a 4 mm and 6 mm radius indenters. In Fig. 9c, both the 4 mm and 6 mm indenters was used. Fig. 9d and 9e shows B1 elastomer compressed by a 4 mm and 6 mm indenters. In Fig. 9f, both the 4 mm and 6 mm indenters was used for the B1 elastomer. The indentation depth, in all cases, was 4 mm. Various initial and end points of optimization with a Nelder-Mead local optimizer are presented for each problem. The valley of these objective functions is represented in gray color. Optimization with different initial points results in a unique end point for each problem which is downhill in all directions toward the optimum point.

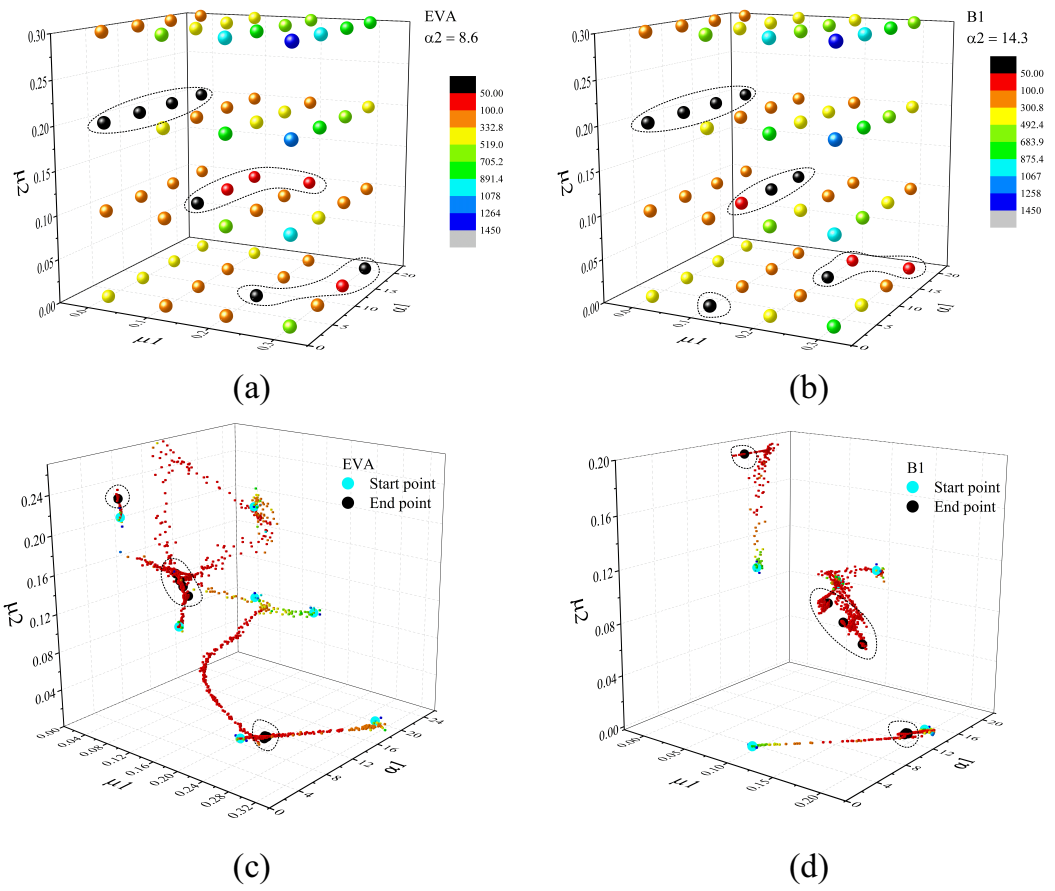

Figure 10: 3D representation of objective function with four parameters. (a) and (b) represent the evaluated sample parameter space. (c) and (d) represent path of the optimization as well as starting and end points. Relative error in the objective function acceptable for convergence is set to $f_{tol} = 10.0$ for local optimizations based on the Nelder-Mead algorithm.

Fig. 10 represents objective function in sample parameter space for second order strain energy function ($N = 2$ in Eq. 1, thus four unknown parameters) as well as several possible initial points for local optimization. Optimization paths, as well as initial and stationary points, are also represented. Results of local optimizations, with various starting points, for identification of 2^{nd} order strain energy function, as given in Table 2, show that the tested EVA and B1 foams have the material property of $N = 1$ in Eq. 1 (1^{st} order strain energy function). Three types of results for the

EVA foam can be distinguished from the results of the 2nd order energy function identification as follows:

1. $\mu_{1s} = 0.22$ MPa and $\mu_{2s} \approx 0$

2. $\mu_{2s} = 0.22$ MPa and$\mu_{1s} \approx 0$

3. $\alpha_{1s} = \alpha_{2s} = 10.52$, $\mu_{1s} = 0.094$ and $\mu_{2s} = 0.126$

Since there is no Poisson's ratio effect, replacing these identified parameters in 2nd order strain energy function ($N = 2$ in Eq. 1) results in 1st order energy function in all three types mentioned above. Therefore, it can be concluded that EVA and B1 foams are compatible with 1st order strain energy functions ($N = 1$ in Eq. 1).

Fig. 10a and 10b shows the 3D representation of objective function (f in Eq. 14) with four variable parameters α_1, μ_1, α_2, μ_2 and $\nu_1 = \nu_2 = 0$. Since these do not demonstrate the change in α_2, this parameter is arbitrarily selected to be 8.6 for EVA foam and 14.3 for B1 foam, which are close to final optimum point. Possible starting points for the local optimizer are inscribed by dashed line in graphs (c) and (d) of this figure, which present three initial and end points of optimization with the Nelder-Mead local optimizer for each problem. The implemented Abaqus software based Python code for the parameter identification by the Nelder-Mead algorithm is presented in Appendix C.

Table 2: 2^{nd} order Hyperfoam model parameter identification results $(\mu_{1s}, \alpha_{1s}, \mu_{2s}, \alpha_{2s})$ for EVA and B1 foams performed with a single indenter of 4 mm radius.

	μ_{1s}	α_{1s}	μ_{2s}	α_{2s}
EVA	0.221	10.65	3.75×10^{-4}	3.43
	0.220	10.52	1.13×10^{-4}	8.53
	6.45×10^{-4}	8.50	0.219	10.52
	0.094	10.52	0.126	10.52
	0.085	10.52	0.134	10.52
B1	0.001	12.69	0.192	12.72
	0.191	12.69	0.001	3.31
	0.192	12.72	0.001	15.81
	0.118	12.74	0.075	12.73
	0.192	12.68	0.001	22.69

2.9 Effect of Indentation Depth in Identified Parameters

As shown in Fig. 11, identified material parameters with the inverse model of the indentation test, vary depending upon indentation depth and indenter size. Upon closer observation, however, it is observed that the discrepancy decreases when the indentation depth is increased. Also, it can be seen that for each indenter size, the identified parameters at different indentation depths follows a linear trend.

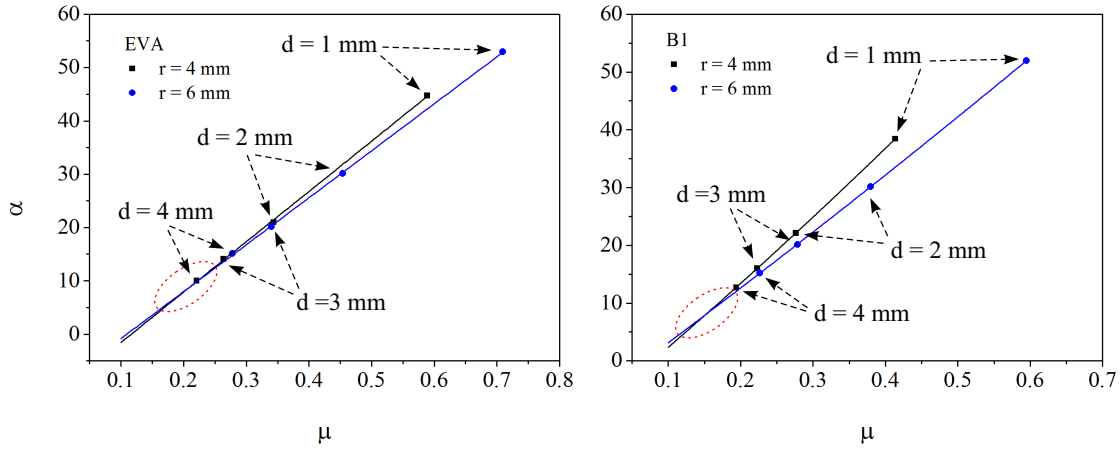

Figure 11: Effect of indentation depth (d) and indenter size (r) on the identified parameters for EVA and B1 foams. Identification is performed with different indentation depths and different indenter sizes.

This observation is in agreement with the Zhang's examination of the Hadamard inverse function theorem on the inverse FE based identification using the spherical indentation [31, 32]. The linear trend of identified parameters for each indenter size, within different depths of indentation, intersects close to the deepest identification points ($d = 4$ mm). Extrapolated values at this intersection point are as $\mu_{EVA} = 0.22$, $\alpha_{EVA} = 10.17$ for EVA foam and $\mu_{B1} = 0.15$, $\alpha_{B1} = 8.3$ for B1 foam. These values are used in the same FE model and comparisons of the indentation reaction force between the FE model and indentation experiment are shown in Fig. 12.

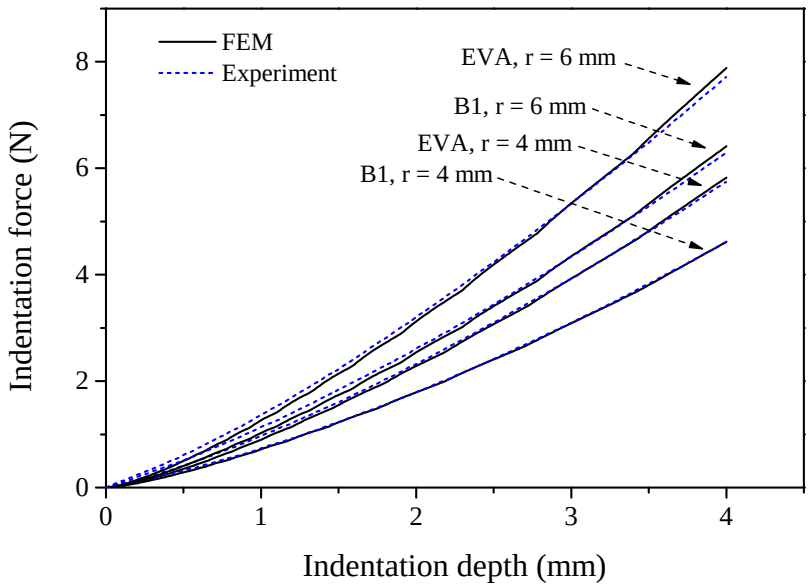

Figure 12: Comparison of the indentation reaction force between FE model and indentation experiment for EVA and B1 foams.

2.10 Identification of Poissons Ratio and Friction Coefficient

Two separate identifications are also performed by considering Poisson's ratio and the friction coefficient as unknown parameters. Initial Poisson's ratio and friction coefficient are selected as: $\nu_{init} = 0.1$ and $\mu^f_{init} = 0.1$ and the optimization problems are defined as:

$$f(\alpha, \mu, \nu) = \sum_{t=1}^{N} \left| {P_t}^{FEM}(\alpha, \mu, \nu) - {P_t}^{meas} \right| \tag{15}$$

$$f\left(\alpha, \mu, \mu^f\right) = \sum_{t=1}^{N} \left| {P_t}^{FEM}\left(\alpha, \mu, \mu^f\right) - {P_t}^{meas} \right| \tag{16}$$

Fig. 13a and Fig. 13b show identification of Poisson's ratio and the friction coefficient in an inverse modeling problem of indentation.

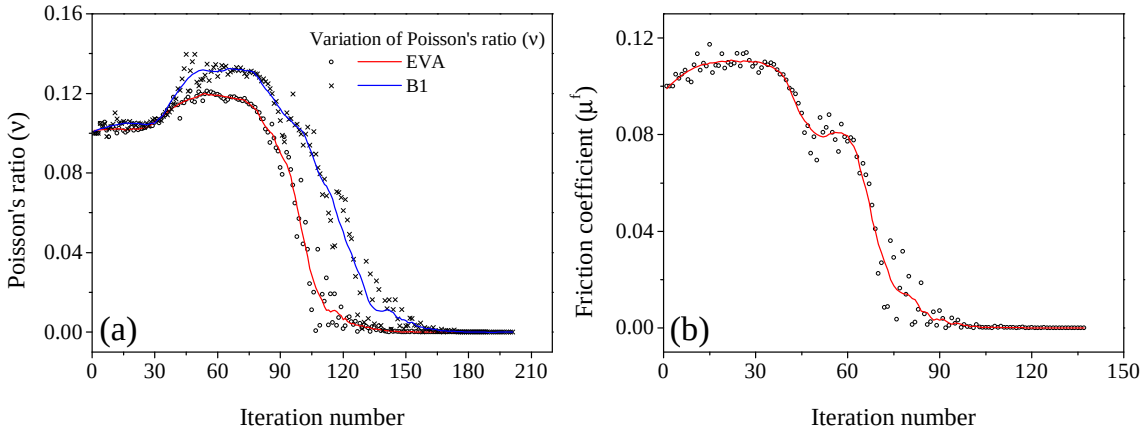

Figure 13: (a) Identification of Poisson's ratio in an inverse modeling problem. (b) Identification of the friction coefficient between the indenter and EVA foam in an inverse modeling problem. Relative error of $f_{tol} = 10.0$ is employed for the convergence.

As can be seen in Fig. 13a and Fig. 13b, identification of Poisson's ratio and the friction coefficient, together with other material model parameters, resulted in values of 8.0×10^{-4} and 4.6×10^{-4} respectively. These very small values prove the validity of the assumption that $\nu = 0$ and that there is no friction between the indenter and hyperelastic foam. These figures illustrate variation in Poisson's ratio and friction coefficient in an inverse modeling problem of indentation up to 4 mm with Hyperfoam material model and indentation test on EVA and B1 elastomers. Friction is modeled by penalty contact algorithm. An interpolated solid line is drawn between data points which are smoothed by a Savitzky-Golay filter with a window size of 25 points.

2.11 Identification of Hyper-Viscoelastic Model for Liver Tissue

The same identification process is employed for HV model of bovine liver tissue. Ogden and Prony series are employed for modeling hyperelastic and viscoelastic behavior, respectively. Reaction force of indentation is acquired in two steps, indenting up to 4 mm with indentation rate of 1 mm.s^{-1}, following by a relaxation step as a result of constraining the indenter at 4 mm depth. First order objective function ($N = 1$ in Eq. 14) is used which includes 6 parameters as (α, μ, D) for the Ogden model and (g, k, τ) for the Prony series. The parameter space is formed by a $3 \times 3 \times 3 \times 3 \times 3 \times 3$ grid of $(\alpha, \mu, D, g, k, \tau)$. Subsequent local optimizations are performed on candidate starting points using the Nelder-Mead method. Resulted parameters are as following:

$$\mu = 5.329 \times 10^{-4} \qquad \alpha = 21.8$$

$$D = 2.5 \qquad g = 0.822$$

$$k = 0.003 \qquad \tau = 0.999$$

Comparisons between the indentation reaction forces of experiments and FE model are shown in Fig. 14. A good agreement can be seen in the loading/relaxation curves achieved by the FE model and the experiment.

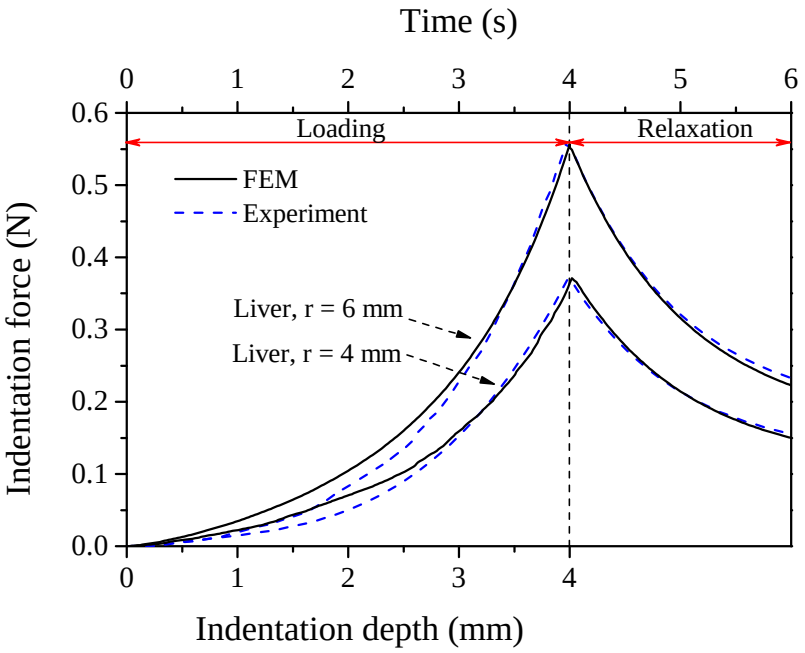

Figure 14: Comparison of the indentation reaction force between FE model and indentation experiment for bovine liver tissue. Relative error of $f_{tol} = 10.0$ is employed for the convergence.

2.12 Conclusions

In this work, an inverse model program of estimated hyperelastic and hyper-viscoelastic material parameters has been developed based on the FE model and experiment of indentation using spherical indenters. Global optimization with single and multi-objective function methods, based on the Nelder-Mead simplex algorithm, have been employed for solving these inverse problems. Parameters of a suitable hyperelastic model have been identified for two different closed cell foams, namely EVA and B1. The validity of assuming frictionless contact between the indenter and foams during these indentation tests, as well as zero Poisson's ratio for closed cell foams, have been demonstrated using the same inverse model problem. The effect of indentation depth

was also investigated in estimated parameters and a numerical relationship was observed and reported in results. The flexibility of this inverse method makes it suitable for general identification processes where direct measurements are not easily applicable. Applicability of this method is demonstrated on problem of hyper-viscoelastic material parameters identification for bovine liver tissue. It has, however, been shown that the accuracy of parameter identification using inverse indentation modeling is sensitive to both indentation depth and indenter size. It has also been shown that, by increasing the indentation depth, the difference between identified parameters using different indenter sizes decreases correspondingly. When comparing direct measurement methods and identification by single element models, identification using inverse modeling of indentation necessitates a great deal of computer time and hence is costly. Therefore, higher computational costs will inevitably be incurred with this model in order to obtain the material parameters with the same speed as those using direct measurement methods.

Chapter 3

Real-time Soft Material Identification for Use in Minimally Invasive Robotic Surgery

This chapter investigates the real-time methods by which it is possible to identify the parameters of biological tissues, which possess nonlinear mechanical properties, in order to identify tissues in contact with robot end effector during minimally invasive robotic surgery (MIRS). Two approaches are adopted, namely the variance calculation and the Kalman filter method based on inverse finite element modeling (FEM). Material parameters were identified in real time experiments of indentation. Indentations were performed at different rates with a robotic arm equipped with an indentation probe. The performance of both algorithms were assessed in material parameter identification and was found to yield a performance success rate of greater

than 90%. The two approaches were compared in terms of computation time and accuracy. The variance measurement method is suitable for real-time identification with all indentation rates. In comparison, the Kalman filter method requires higher real-time processing power for high indentation rates.

3.1 Material Parameter Identification with Inverse Finite Element Method and Indentation Test

As mentioned before, soft tissues possess nonlinear mechanical properties and are usually modeled by variants of strain energy functions [22, 23]. Since strain energy functions generally comprise several of the material's physical properties, as well as parameters without any physical interpretation, accurate identification is often a challenging task. To determine these parameters, standard mechanical tests such as tensile, compression, shear, and volumetric tests can be performed. However, these tests are repetitive and demand exact control on sample geometry and test conditions. Furthermore, especially during the higher and maximum strain levels, physical restrictions may introduce errors in the test results. For example, friction in the compression test and strength of the adhesive at the sample interface and loading plate, during the shear test, may cause bulging and give rise to erroneous test results. All this gives rise for the need to utilization of optimization and state estimation algorithms coupled to the simulation software for parameter identification by inverse modeling [24, 25]. Inverse modeling allows conversion of observed measurements of a

physical system into constitutive parameters of its mathematical model [18]. Therefore, inverse modeling of a well-defined mechanical test on a suitable mathematical model would result in acquiring optimum parameters which can be either material properties or those that are difficult to measure, such as friction. Within various mechanical tests, the indentation test simulates various modes of deformation in a given sample [26]. Therefore, an inverse model of indentation test would guarantee parameter retrieval through complex modes of deformation in such a sample. This is in contrast with controlled tests which are designed for generating either a particular stress or strain state in test specimens. In this research, an indentation test is employed along with a practical real-time inverse finite element modeling algorithm for material parameter identification.

3.2 Real-Time Parameter Identification

As mentioned in Chapter 2, a typical method of identifying parameters, based on the inverse finite element modeling, involves an objective or error function. The objective function is generally based on the difference of experimental measurements as opposed to their counterparts in the finite element model of the same experiment. The two methods used in this work are the variance measurement and the Kalman filter method, in which error functions are employed to measure the difference between the experiment and the numerical model.

3.2.1 Variance Measurement Method

The schematic of the parameter identification with FEM is shown in Fig. 5. As can be seen in this figure, this method necessitates evaluating the objective function in each step of the optimization process, as shown in the Minimize error function block. Since the objective function includes the FE model, each evaluation requires FE analysis of the model and requires a great deal of computing time so it is not, therefore, suitable for the real-time processing. In this research, an efficient method is proposed in which the computational work of the FE analysis was performed in advance wherein its parameter has already been determined. As previously mentioned, mechanical test of indentation is employed in this research for which the curves of force versus depth are generated using the FE model for the desired space of parameters which are intended to be identified. These curves are then saved in a storage matrix for purpose of comparison in a real-time scenario. In this method, the optimization (error minimization) step in inverse modeling has in fact been broken down to searching for the most similar curve from the storage matrix. In order to perform this search efficiently in real-time, a comparison and error measurement was performed simultaneously during the indentation process. A two-dimensional matrix was used for storing results of the FEM analysis. Contained in this matrix are the indentation force at certain time increments ($1\Delta t,\ 2\Delta t,\ 3\Delta t, \ldots, T$) at period T. Each row in this matrix represents time increments, and each column relates to a unique combination of material model parameters. The parameter space is constructed by dividing the range of the pertinent material model parameters provided for by a number of increments depending

on the desired precision. As an example, Fig. 15 represents the schematic of the real time objective or error function evaluation for a material model of two mechanical parameters, A and B.

In this example, the indentation force is calculated and measured in ΔT time increments by the FE analysis of the indentation model and performing a similar indentation experiment. The parameter space, in this example, is constructed by dividing parameters A and B into n and m parts, respectively. Each column of the storage matrix is related to a unique combination of the A and B parameter values (a and b). The error or objective function (E), is constructed by calculating the absolute difference between the calculated and measured curves of indentation force, as shown in Eq. 17:

$$E = \begin{bmatrix} |f_{1\Delta t} - f^1_{1\Delta t}| + |f_{2\Delta t} - f^1_{2\Delta t}| + |f_{3\Delta t} - f^1_{3\Delta t}| + \cdots + |f_T - f^1_T| \\ |f_{1\Delta t} - f^2_{1\Delta t}| + |f_{2\Delta t} - f^2_{2\Delta t}| + |f_{3\Delta t} - f^2_{3\Delta t}| + \cdots + |f_T - f^2_T| \\ |f_{1\Delta t} - f^3_{1\Delta t}| + |f_{2\Delta t} - f^3_{2\Delta t}| + |f_{3\Delta t} - f^3_{3\Delta t}| + \cdots + |f_T - f^3_T| \\ \vdots \\ \left|f_{1\Delta t} - f^{n\times m}_{1\Delta t}\right| + \left|f_{2\Delta t} - f^{n\times m}_{2\Delta t}\right| + \left|f_{3\Delta t} - f^{n\times m}_{3\Delta t}\right| + \cdots + \left|f_T - f^{n\times m}_T\right| \end{bmatrix} \quad (17)$$

where f_t is the experimentally measured value of the indentation force at time t and f^i_t is the calculated value of the indentation force from the FE model analysis related to i^{th} number of combination of material parameters at time t. Each row in this matrix is the absolute value of error, which represents the difference between the experimentally measured and calculated (FE analysis) curves of the indentation force.

The advantage of this method is that the error is calculated while the indentation is actually being performed. At the end of the indentation process, the error matrix was fully evaluated and the smallest valued element of this matrix represented the curve of interest that showed the minimum difference between the measured and calculated curves. Therefore, the material parameters corresponding to the minimum element of the matrix E would be potentially the closest parameter set for the indented material. A block diagram of this process is shown in Fig. 16.

The procedure shown in Fig. 16 is performed during the indentation process. Once the indentation process finishes, the error vector (E) is ready to determine the minimum element of the matrix and extracting its corresponding material parameters from a lookup table based on its index as the final identified parameters.

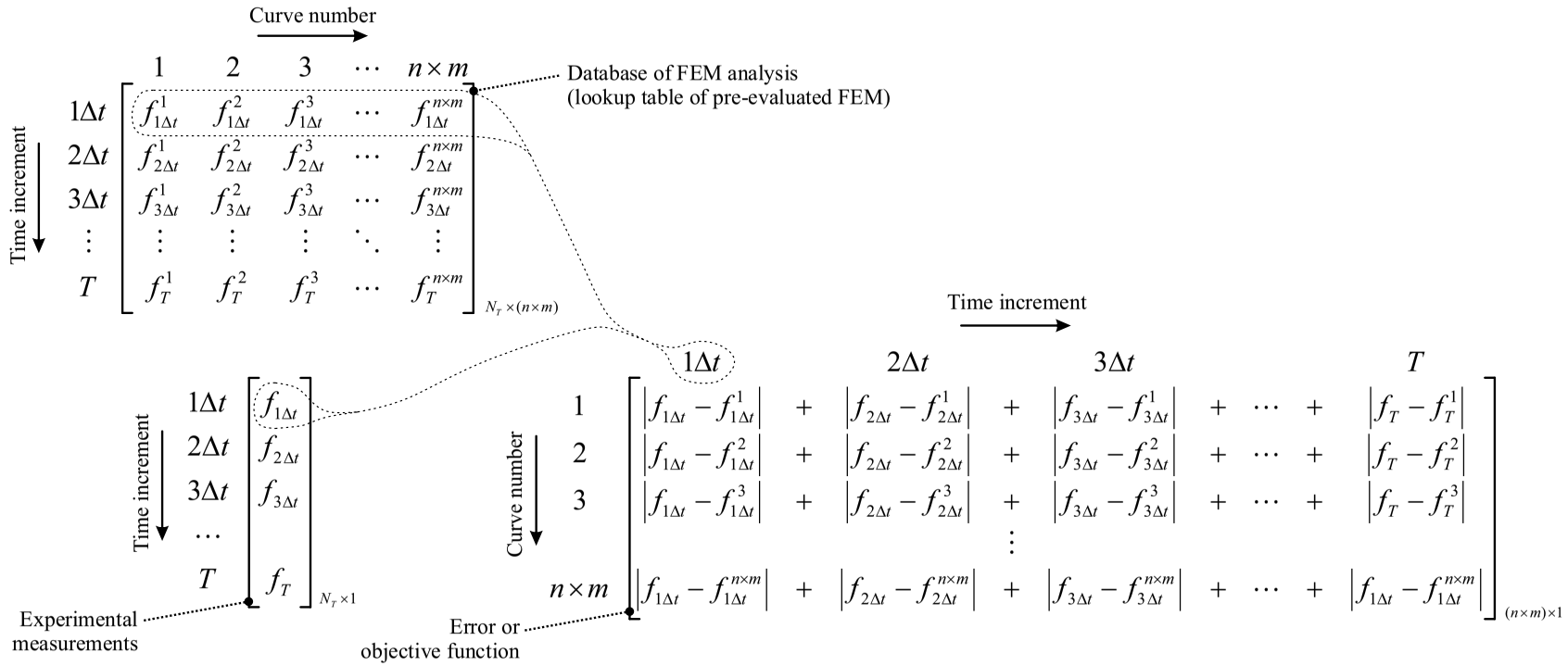

Figure 15: Schematic of real-time objective function evaluation for a material model containing two mechanical parameters, A and B. T is the time of indentation process. Feasible range of parameters are divided to n and m sections. $n \times m$ number of indentation force curves are calculated by FE analysis of the indentation.

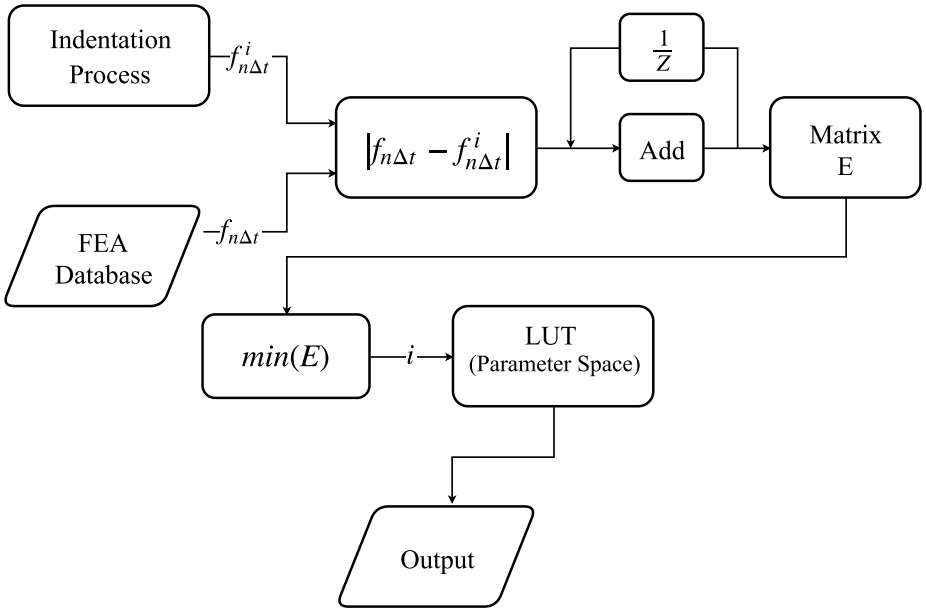

Figure 16: Block diagram of error matrix calculation for real-time material parameter identification. Index of the minimum member of the matrix E is used to extract material parameters from storage matrix or lookup table (LUT).

3.2.2 The Kalman Filter Method

The Kalman filter, named after Rudolf Emil Kalman, is an algorithm that estimates unknown variables using a series of noisy measurements observed over time and contain inaccuracies. More formally, the Kalman filter was developed as an optimal signal processing algorithm which operated recursively on noisy input data in order to statically identify the underlying system state [109]. Technically, this algorithm updates the previous estimates of unknown system variables through indirect measurements of the system state and the covariance information of both the measurement variables and the real system state. This recursive procedure has been widely used in such fields as signal processing, radar systems and navigation [110]. Recently, application of this

method was proposed for identifying material parameters using the inverse finite element method and was investigated for the first time by Nakamura et al. [27,91]. They created a reference data source using a FE model of micro indentation and analyzing this model in a 4×4 material parameter space (two material parameters each in a reasonable range divided by 4) for non linear FGMs. They interpolated the curves of displacement versus indentation force and their gradients with respect to the material parameter space (in their study, parameter space have two members or two material parameters) using bi cubic Lagrangian functions[1]. They successfully employed the Kalman filter method to estimate material parameters by performing micro indentation experiments and extracting the material parameters as the underlying system state. In another similar study, Li et al. employed the same approach with macro indenters. They applied this method on closed cell foams to obtain their hyperelastic material properties [28]. Although researchers have shown that the Kalman filter method is suitable for parameter identification, they have not yet investigated the capability of this method for real time material parameter identification applications. The main advantage of the estimation using this method is its recursive nature which allows it to run in real time using only the most recent measurements, the uncertainty matrix and the latest state estimates.

[1]In mathematics, bi-cubic interpolation is for interpolating data points in two dimensions.

3.2.3 Theory of the Kalman Filter

The Kalman filter formulation is based on the update algorithm shown in Eq. 18:

$$x_n = x_{n-1} + K_n \left[y_n - H_n \left(x_{n-1} \right) \right] \tag{18}$$

In this equation, x_n is a posteriori state estimate at updating increment n, x_{n-1} is a priori state estimate, y_n is the noisy observation, H_n is the function of exact relation between the state parameters (e.g. material constants) and the measured variables, and the correction at each time increment is made by the Kalman gain matrix, K_n. The difference $[y_n - H_n (x_{n-1})]$ in this formula is called the measurement innovation which shows the discrepancy between the predicted and the actual measurement. K_n is calculated from Eq. 19:

$$K_n = P_n h_n^T R_n^{-1} \tag{19}$$

where P_n is the measurement covariance matrix as calculated from Eq. 20:

$$P_n = P_{n-1} - P_{n-1} h_n^T \left[h_n P_{n-1} h_n^T + R_n \right]^{-1} h_n P_{n-1} \tag{20}$$

In this equation R_n is the error covariance matrix and is related to the measurement error. Gradients of H_n with respect to the x_n are contained in matrix h_n.

The flowchart of parameter identification process using the Kalman filter is shown

in Fig. 17 which shows that the process starts by assigning an initial estimate after which each estimate is performed incrementally by calculating the matrices of gradient, covariance and the Kalman gain.

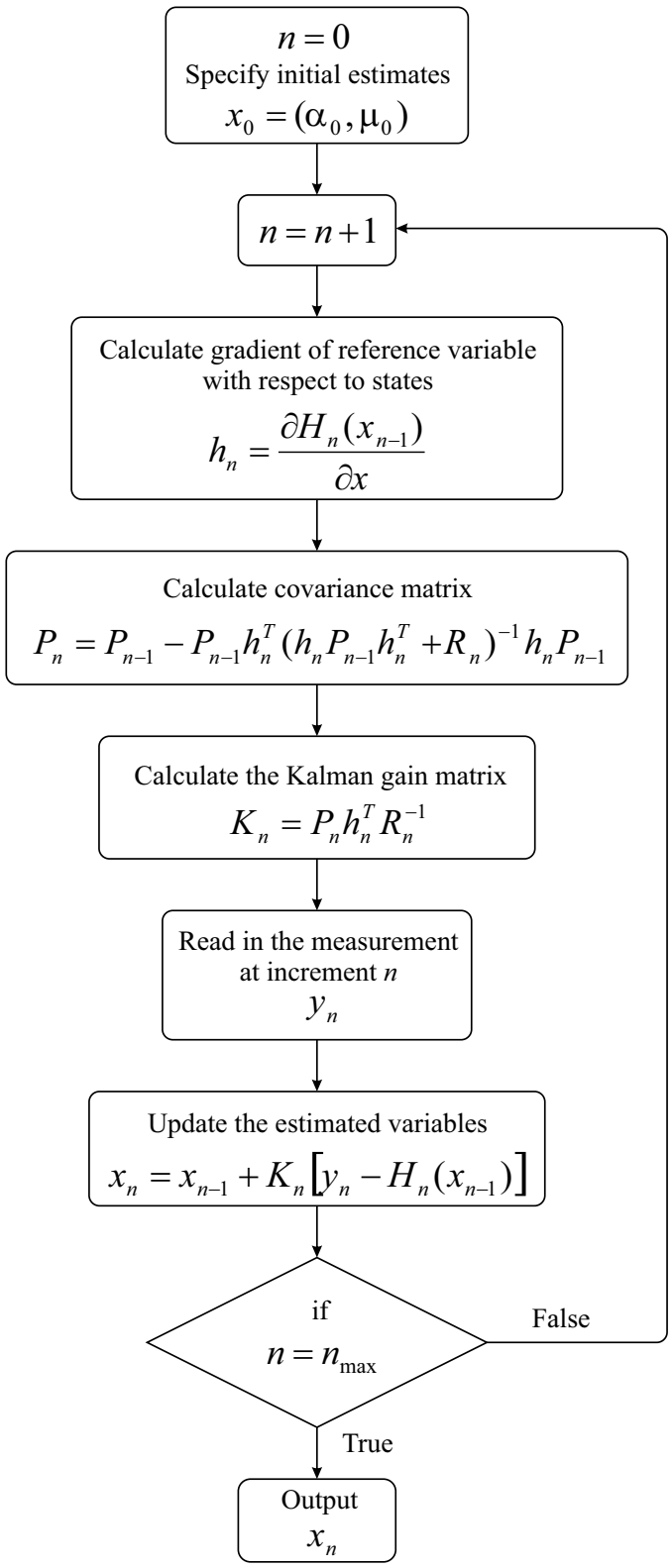

Figure 17: Flowchart of parameter identification based on Kalman filtering.

The convergence characteristics of the Kalman filter depends on factors such as initial estimates, measurement error and accuracy of the H_n and h_n functions. A successful Kalman filtering process for material parameter identification requires an appropriate range for unknown variables, selection of a reasonable time increment, preparation of a reference data source for the measurement variables and their gradients with respect to estimation variables, and determination of suitable values for the matrices of covariance, P_0 and R_n.

3.2.4 Kalman Filter Implementation for FEM Based Inverse Parameter Identification

As previously mentioned, the Kalman filter can be adopted for inverse identification problems. In this research, the Kalman filter is implemented for the identification of hyperelastic and hyper-viscoelastic (HV) material properties based on indentation tests. By measuring the indentation load and depth of the indentation, and providing this information along with results of the FE model of same procedure to the Kalman filter algorithm, the underlying model of the material is identified in terms of hyperelastic and HV material model parameters. A schematic of the algorithm for the Kalman filter that is applied when identifying material parameters is shown in Fig. 18. As shown, a mechanical test of indentation is employed for identifying hyperelastic material parameters, α and μ. The FE model is evaluated prior to the identification processes. The indentation force is calculated in parameter space at each indentation depth increment.

An example of an indentation force surface, in a 2D parameter space of α and μ, is shown in Fig. 19.

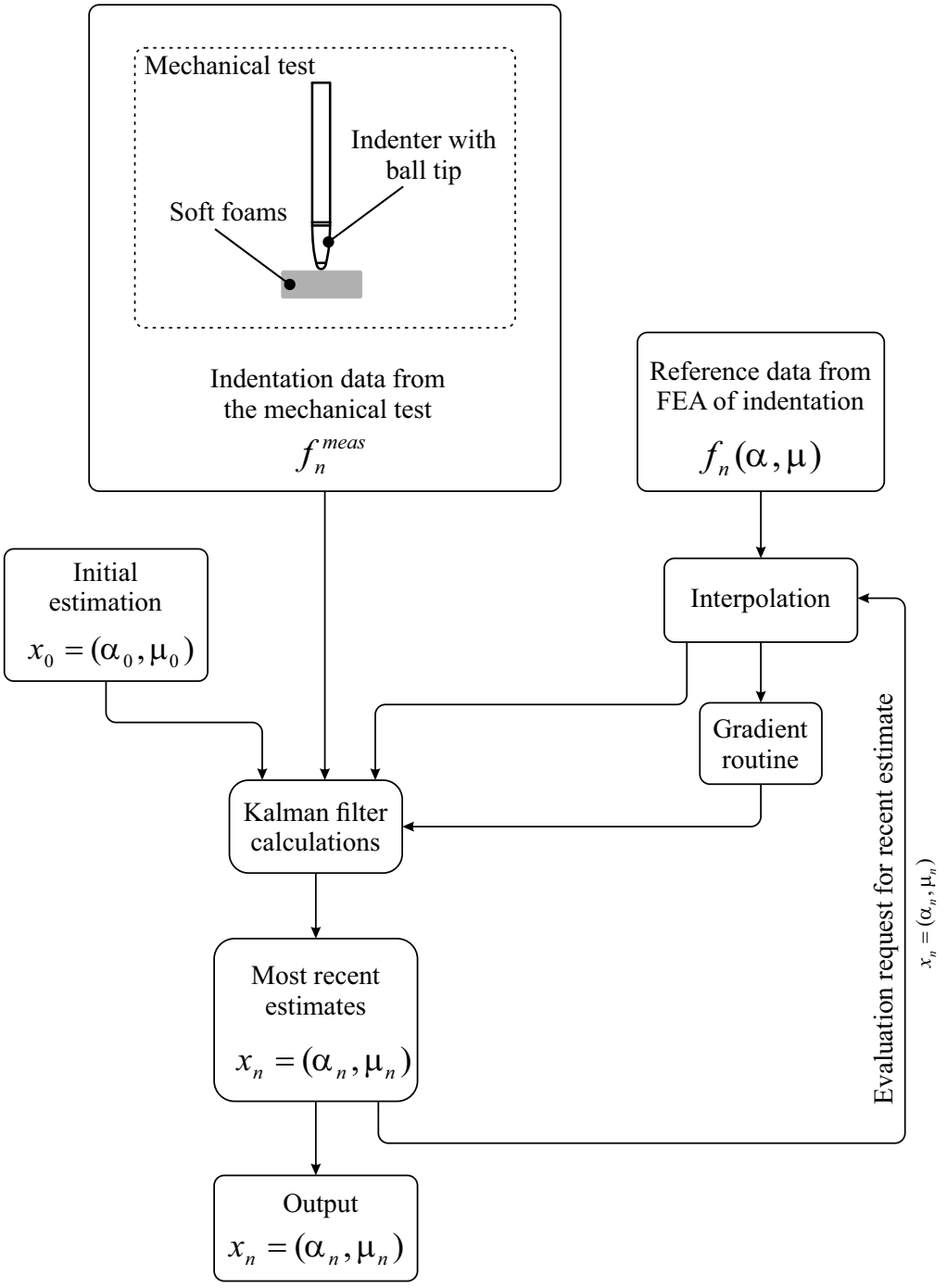

Figure 18: Schematic of the procedure for identifying first order hyperelastic material parameters using the Kalman filter and FE analysis.

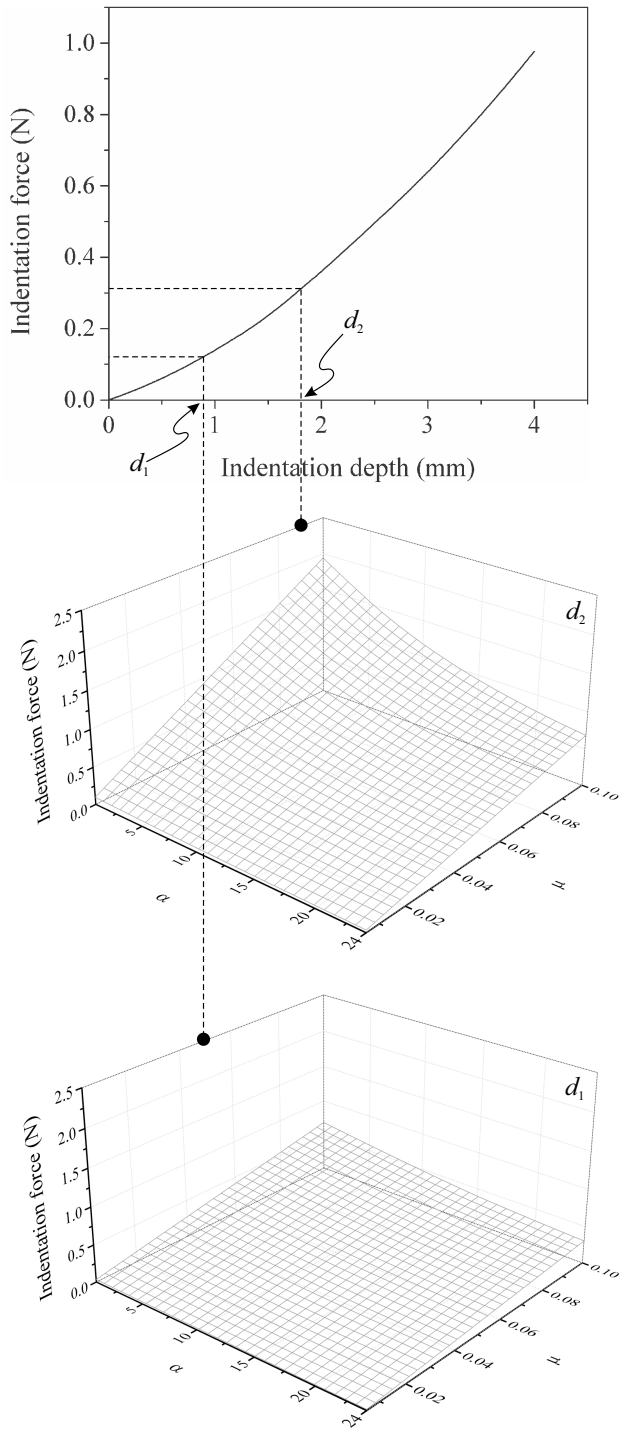

Figure 19: Surface of indentation force in the parameter space (α and μ) at two different depths of the indentation process, d_1 and d_2.

The measured indentation load (f_n^{meas}) is selected as the measurement variable

or noisy observation (y_n) and displacement of the indenter is selected as the filtering increment or process time increment (n). Unknown hyperelastic parameters are defined as $x_n = (\alpha_n, \mu_n)^T$. In Eq. 18, the function $H_n(x_{n-1})$ is the exact value of the indentation load at the latest state variable estimation x_{n-1}. This function is a representation of the exact model of the indentation process and is created by FE analysis of the indentation, similar to that described in variance measurement method. As previously mentioned, the parameter h_n is a gradient of the function H_n with respect to the material parameters, α and μ. The measurement covariance is a 2×2 matrix and its initial value is calculated as Eq. 21:

$$\begin{bmatrix} (\Delta\alpha)^2 & 0 \\ 0 & (\Delta\mu)^2 \end{bmatrix} \tag{21}$$

where $\Delta\alpha = \alpha_{max} - \alpha_{min}$ and $\Delta\mu = \mu_{max} - \mu_{min}$. In the error covariance matrix, R generally corresponds to the estimated maximum measurement error as $R_n = R^2$ where $R = |f_n^{err}|_{max}$. The value of R can be considered as constant throughout the analysis. Matlab code of the parameter identification based on the Kalman filter is presented in Appendix D.

3.2.5 Bounded State Space Estimation

Since each member of the material parameter space (e.g. α and μ in this research) in the pre-evaluated numerical model is a scalar with a range that is bounded by feasible upper and lower levels, it follows that the parameter space itself is bounded

in all dimensions. Depending on the state (material parameter) space geometry, the estimated value might fall beyond the feasible region of parameters. As explained in theory of the Kalman filter method, reference data are generated in a reasonable range of material parameters by evaluating the FE model at reasonably distributed equidistant grid points of the parameter space. However, an improper selection of the initial estimate might lead the Kalman estimation path to the boundaries of the parameter space, and further estimation might require a nonexistence function value from the reference data and related gradients, namely $H_n(x_{n-1})$ in Eq. 18 and h_n in Eq. 20. This condition would stop the parameter estimation of this process and provide a spurious output reading. Although there is no general method to handle the bounded state estimation in Kalman filter theory, some efforts have, nonetheless, been made in this respect. For instance, the estimates which are out of state space bounds can be projected onto the boundary of the feasible region [111–113], or in state estimation of non linear systems with unscented Kalman filter[2], the shrinking of sigma points is proposed in [93]. Since the linear Kalman filter method is employed in this research, the projection method fits the estimation problem very well. A schematic example of the projection in a two-dimensional parameter space (e.g. α and μ) is shown in Fig. 20.

[2]The unscented Kalman filter is used in highly non linear systems. In this method, several sampling points (Sigma points) are produced around the current estimate. Then these points are propagated through the non linear map to get more accurate estimation of the mean and the covariance.

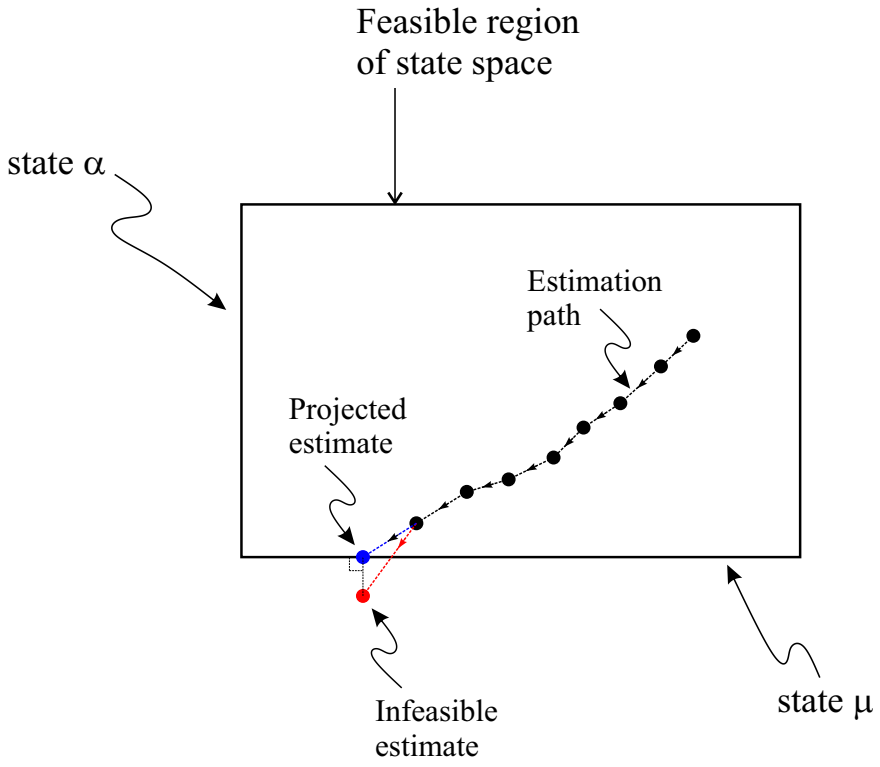

Figure 20: Schematic of the projection method for bounded state estimation using the Kalman filter method.

Another bounded estimation method is also implemented in this work, which involves penalizing of the Kalman gain (K), which prevents the estimator from indenting to the infeasible state space. The idea of penalizing is employed to add a repelling property to the state space boundary. The marginal Kalman gain (K in Eq. 18) for upper and lower bounds of the state space is calculated as shown in the

following precursors to Eqs. 22 and 23:

$$x_n = x_{n+1} + K_n \left[y_n - H_n \left(x_{n-1} \right) \right]$$

$$x_n \leq x_b^{max} \Rightarrow x_{n-1} + K_n \left[y_n - H_n \left(x_{n-1} \right) \right] \leq x_b^{max}$$

$$x_n \geq x_b^{min} \Rightarrow x_{n-1} + K_n \left[y_n - H_n \left(x_{n-1} \right) \right] \geq x_b^{min}$$

$$K_n \left[y_n - H_n \left(x_{n-1} \right) \right] \leq x_b^{max} - x_{n-1}$$

$$K_n \left[y_n - H_n \left(x_{n-1} \right) \right] \geq x_b^{min} - x_{n-1}$$

$$K_n \leq \frac{x_b^{max} - x_{n-1}}{y_n - H_n \left(x_{n-1} \right)} \tag{22}$$

$$K_n \geq \frac{x_b^{min} - x_{n-1}}{y_n - H_n \left(x_{n-1} \right)} \tag{23}$$

where, x_b^{max} and x_b^{min} are upper and lower bounds of the state space.

By converting the inequalities of Eqs. 22 and 23 to equalities, a penalty coefficient (C_p) was introduced to Eqs. 24, 25, 26 and 27:

$$if x_n \geq x_b^{max},\ K_n \geq 0 \Rightarrow K_n = (1 - C_p) \frac{x_b^{max} - x_{n-1}}{y_n - H_n \left(x_{n-1} \right)},\ 0 \leq C_p \leq 1 \tag{24}$$

$$if x_n \leq x_b^{min},\ K_n \geq 0 \Rightarrow K_n = (1 + C_p) \frac{x_b^{min} - x_{n-1}}{y_n - H_n \left(x_{n-1} \right)},\ 0 \leq C_p \leq 1 \tag{25}$$

$$if x_n \geq x_b^{max},\ K_n < 0 \Rightarrow K_n = (1 + C_p) \frac{x_b^{max} - x_{n-1}}{y_n - H_n \left(x_{n-1} \right)},\ 0 \leq C_p \leq 1 \tag{26}$$

$$if x_n \leq x_b^{max},\ K_n < 0 \Rightarrow K_n = (1 - C_p) \frac{x_b^{min} - x_{n-1}}{y_n - H_n \left(x_{n-1} \right)},\ 0 \leq C_p \leq 1 \tag{27}$$

The value of the penalty coefficient in the above equations determines the repelling

power of the state space boundary.

In addition to the projection and penalty methods, extrapolation of the state space is also employed in order to prevent failure of the identification process. Although the extrapolation prevents failure of the estimation process, the estimation itself might not actually converge to a desired solution. Nearest neighbor extrapolation method was employed in this research which assigns values of the nearest neighbor on the boundary for the requested extrapolation point, as shown schematically in Fig. 21. This shows how force is extrapolated for a problem of material parameter identification with two parameters, α and μ. Surface of indentation force is represented in material parameter space at an indentation depth increment.

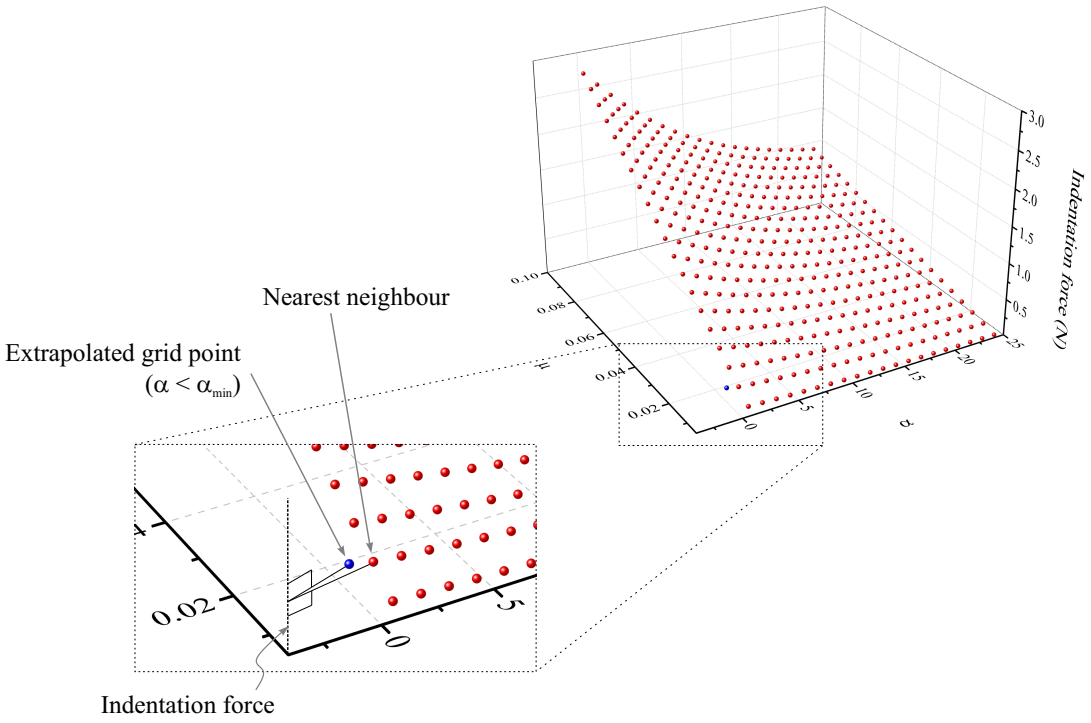

Figure 21: Example of nearest neighbor extrapolation method for calculating indentation force. α_{min} is boundary of the α state.

3.2.6 Parametric Finite Element Model of the Indentation

As mentioned in previously, storage matrices are constructed for storing the FE model analysis results. In order to construct these matrices, a parametric FE model of indentation test was constructed consisting of the material constants that are the primary objective of the identification process. For the purpose of constructing the parametric FE model of indentation, Abaqus software and an axi-symmetric model of indentation were used in this research. The constructed model is shown in Fig. 6(a). The iso-surfaces of the Von Mises stress are shown with color contours from which different modes of deformation can be observed in the material. In this model, hyperelastic and HV material models were used to replicate the mechanical behavior of the hyperelastic foams as well as biological tissues. These models are explained in Sections 2.2 and 2.3.

According to the results of Chapter 2, the foams studied in this research possess first order hyperfoam mechanical behavior. Therefore, the first order hyperfoam model employed in our indentation model has two material parameters, the initial shear modulus, μ, and the parameter α which is related to the shape of the stress strain curve and has no physical interpretation. The FEM storage matrices were constructed by analyzing the indentation model in the uniformly divided parameter space of (μ, α) for the hyperelastic model and $(\mu, \alpha, D, g, k, \tau)$ for the HV models.

Following ranges were used for these parameters:

$$1 < \alpha < 24 \qquad 0.0005 < \mu < 0.3$$

$$1 < D < 4 \qquad 0.0005 < g < 1$$

$$0.0005 < k < 1 \qquad 0 < \tau < 2$$

The storage matrices were then constructed by (30×30) and $(3 \times 3 \times 3 \times 3 \times 3 \times 3)$ members of indentation force curves, respectively for hyperelastic and HV models (the ranges of hyperelastic and HV model parameters were respectively divided uniformly by 30 and 3 grid points). As an example, the indentation curves of five various members of hyperelastic parameter space are shown in Fig. 22.

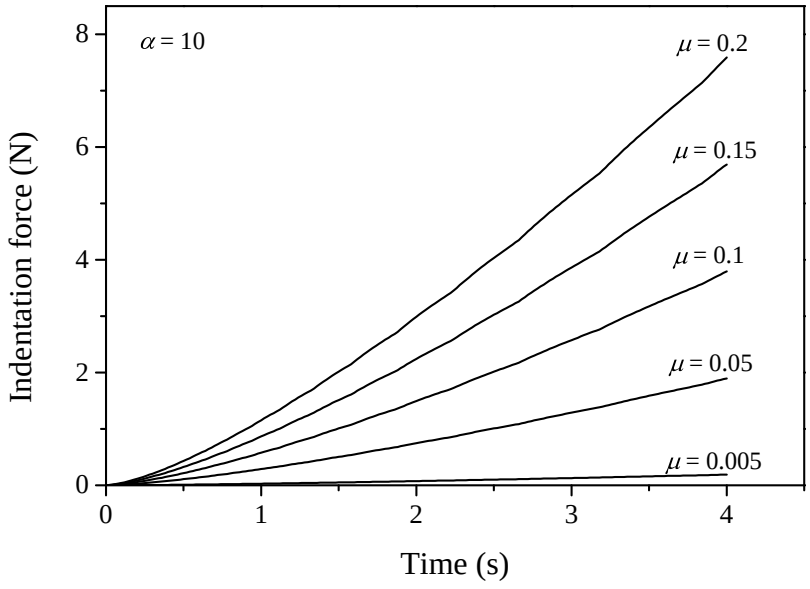

Figure 22: Sample curves of indentation force. These curves are part of the parameter space of storage matrix for FEM analysis results and are calculated using a FEM model with five different sets of parameters: (1) $\alpha = 10$ and $\mu = 0.2$ (2) $\alpha = 10$ and $\mu = 0.15$ (3) $\alpha = 10$ and $\mu = 0.1$, (4) $\alpha = 10$ and $\mu = 0.05$, (5) $\alpha = 10$ and $\mu = 0.005$.

A constant velocity boundary condition is defined for the indenter to indent into the material. Since experiments were performed at three different indentation velocities ($V = 1, 2$ and 4 mm.s^{-1}), the FEM analysis results storage matrix was constructed separately for each indentation velocity. A Python code was written for the Abaqus Python interface in order to automatically analyze the model in each desired parameter space in order to extract the required information for the storage matrices in a data format suitable for the Matlab Simulink.

3.2.7 Indentation Force Probe

A straight rod with a force sensor mounted on its end and a ball transfer unit attached to tip of the sensor was employed in this research. This probe, shown in Fig. 23, consists of an aluminum rod with a gripping handle machined at one end and a force sensor mounting hole on the other end. A strain gage based load cell is employed as the force sensor and a ball caster (ball transfer unit) is attached to one end of the sensor to allow free rolling on the soft material.

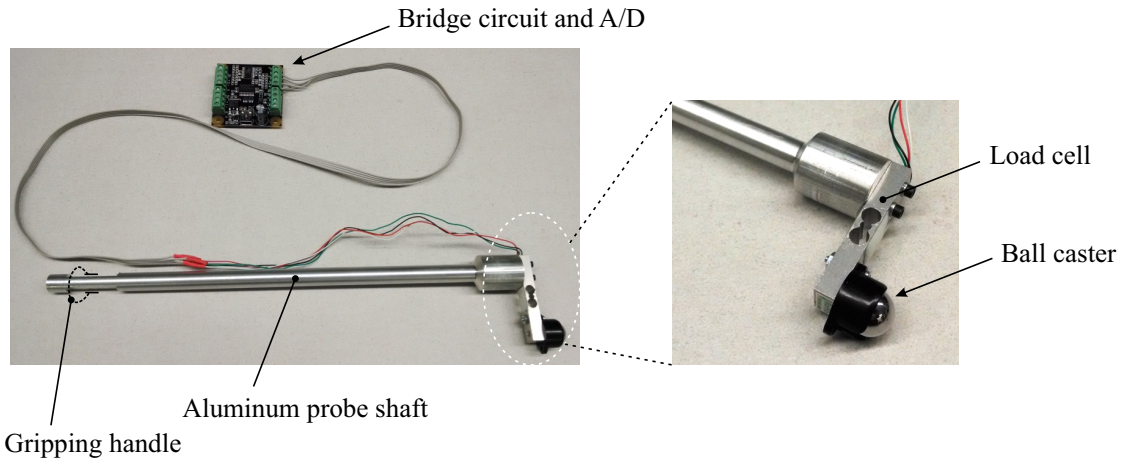

Figure 23: Force or tactile probe used for the indentation process.

3.3 Experimental Method

In order to evaluate the proposed algorithm, a testing scenario was setup analogous to that used during MIRS procedures. This setup consisted of the proposed identification algorithm implemented in Matlab and Simulink software environment, a CRS CataLyst 5 robotic arm and the explained force probe. The schematic of this setup is shown in Fig. 24.

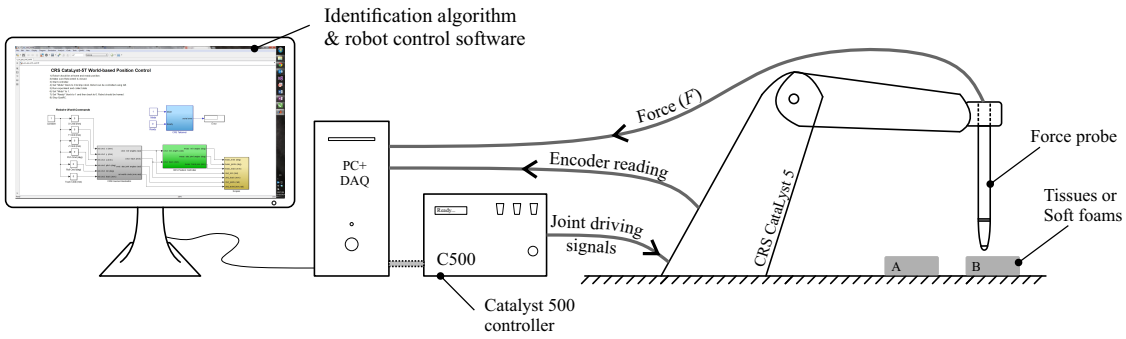

Figure 24: Schematic of test setup for real-time parameter identification.

The robotic arm was controlled by using the inverse kinematic controller software provided by Quanser Inc. and the force probe was held by the gripper located at the end effector of the arm. The identification experiment was performed on four soft materials containing hyperfoam material properties and three biological tissues with hyper-viscoelastic material properties. As an example, the mechanical compression test results of the foams are presented in Fig. 25 from which it can be seen that these materials exhibited severe non-linear deformation behavior.

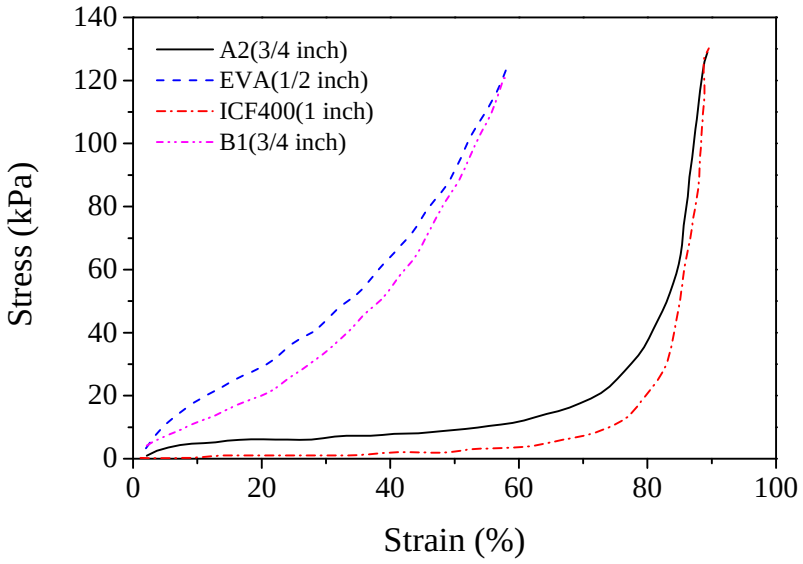

Figure 25: Compression test results of non-linear compressible foams used in this research. Four elastomeric foams are used as: closed cell sponge neoprene (B1), one-inch thick PVC/NBR polymer (ICF), open cell polyether (A2) and closed cell ethylene vinyl acetate (EVA).

A block diagram of the test setup is shown in Fig. 26 in which the dotted rectangle represents the material cart. The global position of the face center for each material is stored as $(x, y, z)_n$.

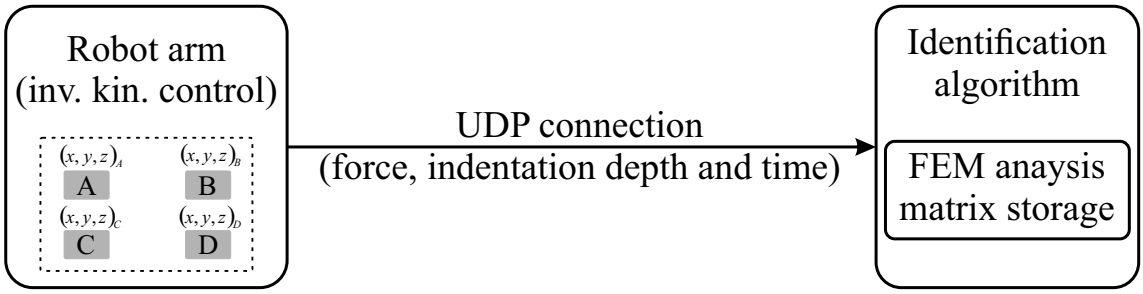

Figure 26: Simplified block diagram of test setup for identifying real-time material properties.

The test setup itself is shown in Fig. 27. Four soft foams and three different biological tissues were used in this experiment, Mat. A represents B1, Mat. B represents ICF, Mat. C represents A2 and Mat. D is EVA.

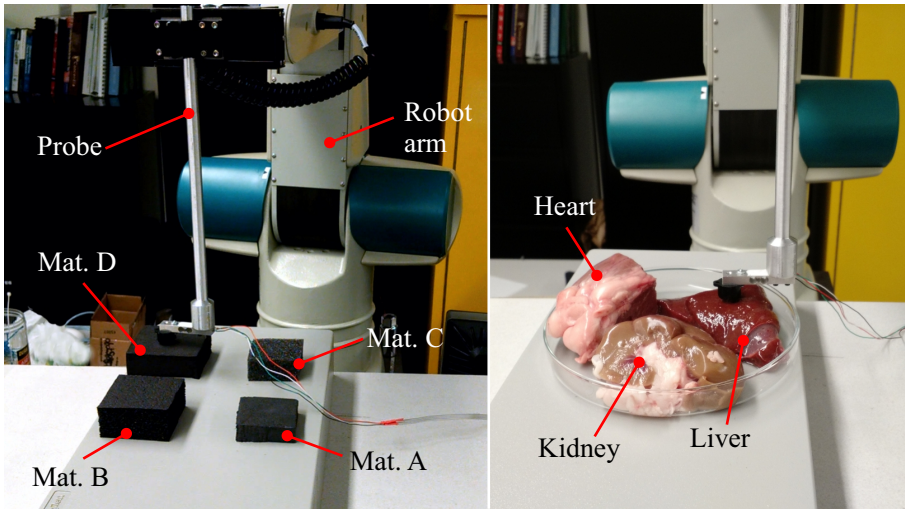

Figure 27: Test setup for identifying real-time material properties.

Two separate Simulink models were constructed for this test setup of which one included the robotic arm control blocks based on robot's inverse kinematics. Positions of the foams are stored in this block, and the arm was programmed to perform indentations of 4 mm depth on each material at their location. Curves of indentation

force were also obtained with the same setup for each material.

The indentation curves are shown in Figs. 28 and 29. Curves were achieved by the described robotic arm test setup. A slight deformation rate dependency can be seen in these curves.

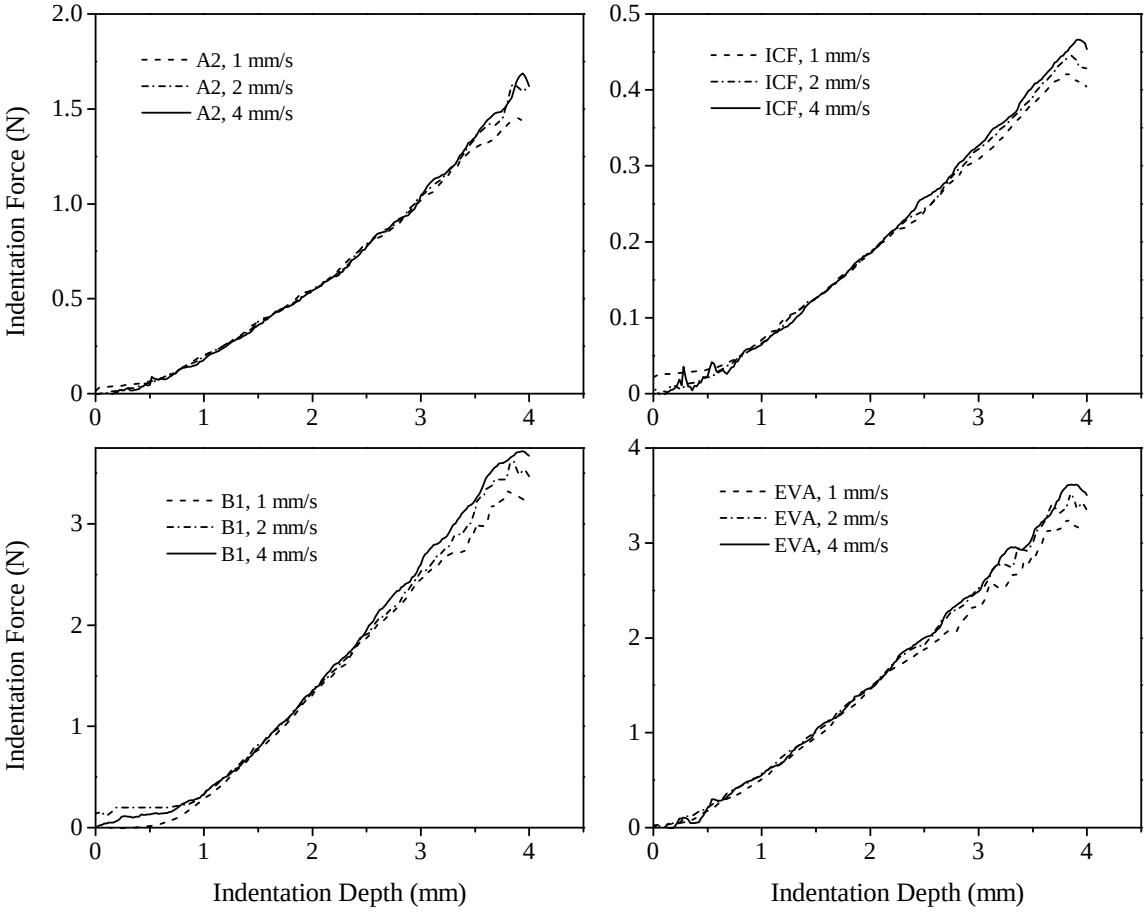

Figure 28: Curves of indentation force versus indentation depth of foam materials.

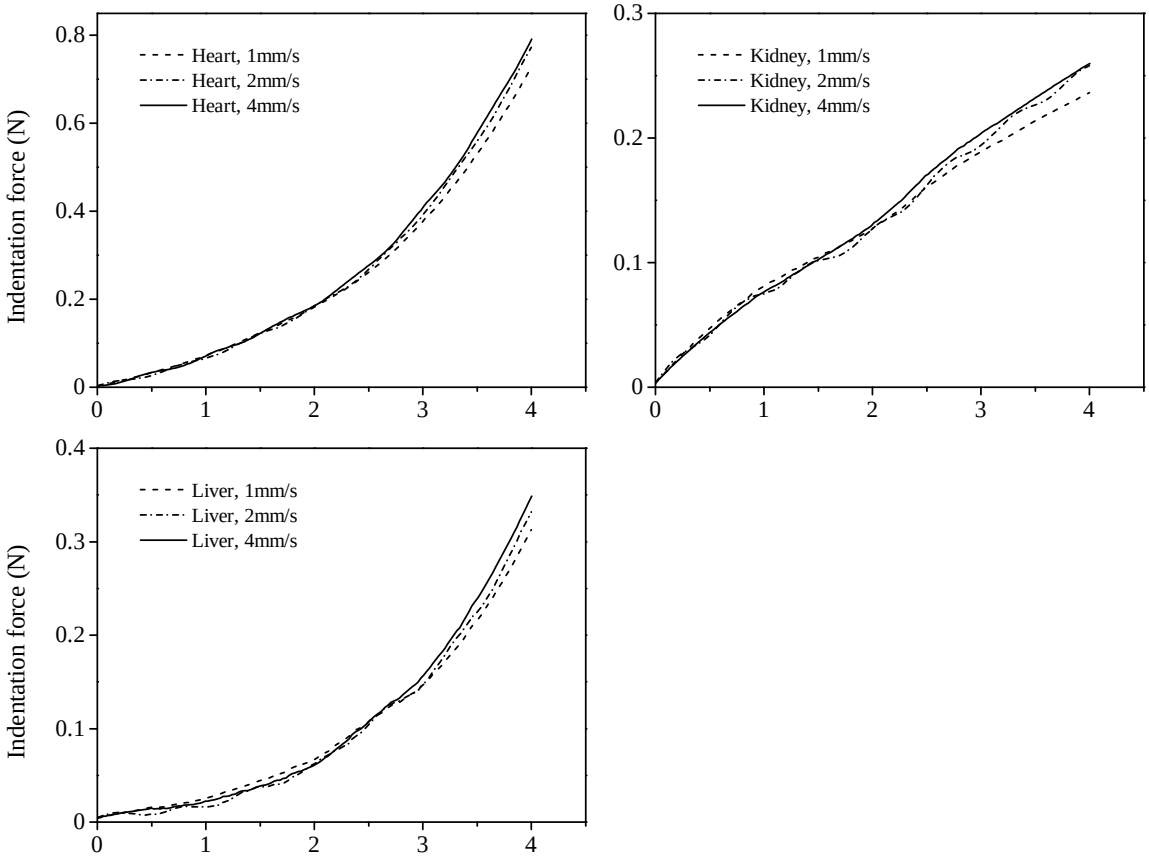

Figure 29: Curves of indentation force versus indentation depth of biological tissues.

Another database of material list was also added to the algorithm in addition to the material property database. In this database, indentation curves of known materials were added, along with some dummy curves, in order to statistically evaluate the algorithm accuracy in distinguishing material type in the identification process. Curves of this database for foams are shown in Fig. 30.

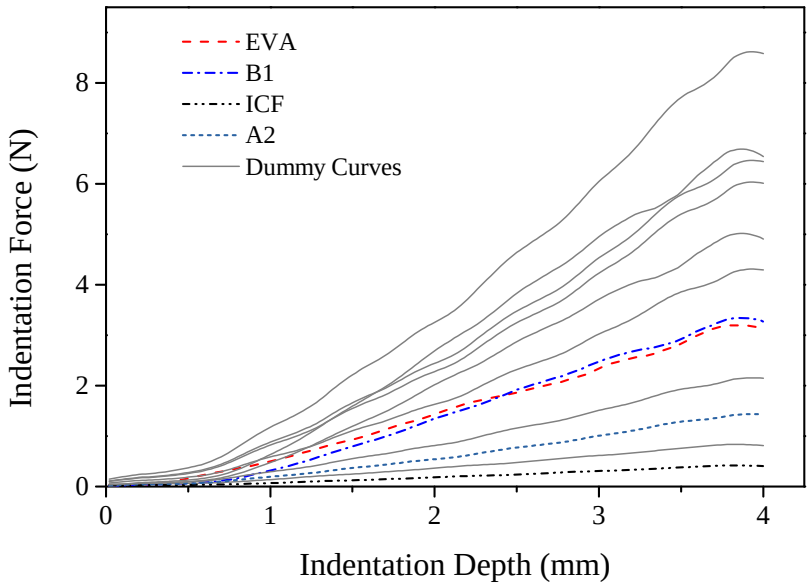

Figure 30: Average of indentation force curves at different indentation rates for recognizing the material type. Dummy curves are added for evaluating the accuracy of the algorithms and increasing the computation load.

3.4 Results and Discussion

Using the test setup shown in Fig. 27, identification experiments were performed with three indentation velocities, $V = 1$, 2 and 4 mm.sec^{-1}. In order to statistically assess the overall performance of the system, the robotic arm software was programmed to perform the indentation in a random manner. One-hundred and fifty random indentations were performed at each indentation rate. A constant seed was used for the random number generator, therefore the same sequence was repeated in each experiment. Results of this experiment on foams, using both the variance and Kalman filter methods at the indentation rate of $V = 2$ mm.s^{-1}, are shown in Figs. 31 and 32. As can be seen in these figures, material B1 exhibits a time-dependent behavior in which

the initial shear modulus decreases as the number of indentations increases. Although this time dependency causes a deviation in parameter estimates, this deviation is alleviated by using the average values of several sequential indentation experiments and by increasing the indentation velocity. For example, the deviation of identified parameter α for material B1 at indentation rates of $V = 1$, 2 and 4 mm.sec^{-1} was 28%, 21.3% and 7.3% . This effect can be explained by the fact that, by increasing the strain rate, the viscous property of the material is relatively eliminated. This effect can also be seen in Fig. 28, as the difference between indentation curves at indentation velocities of 2 and 4 mm.s^{-1} are smaller than those at velocities of 1 and 2 mm.s^{-1}. Statistical material recognition results of these experiments are presented in Table 3.

Table 3: Statistical results of real time identification at various indentation rates using the variance method.

Indentation rate	Successful recognition percentage (%)				
	B1	A2	EVA	ICF	Total
1 mm.s^{-1}	92.1	100	96.8	100	96.7
2 mm.s^{-1}	76.0	97.6	100	100	91.3
4 mm.s^{-1}	100	97.6	94.1	100	98

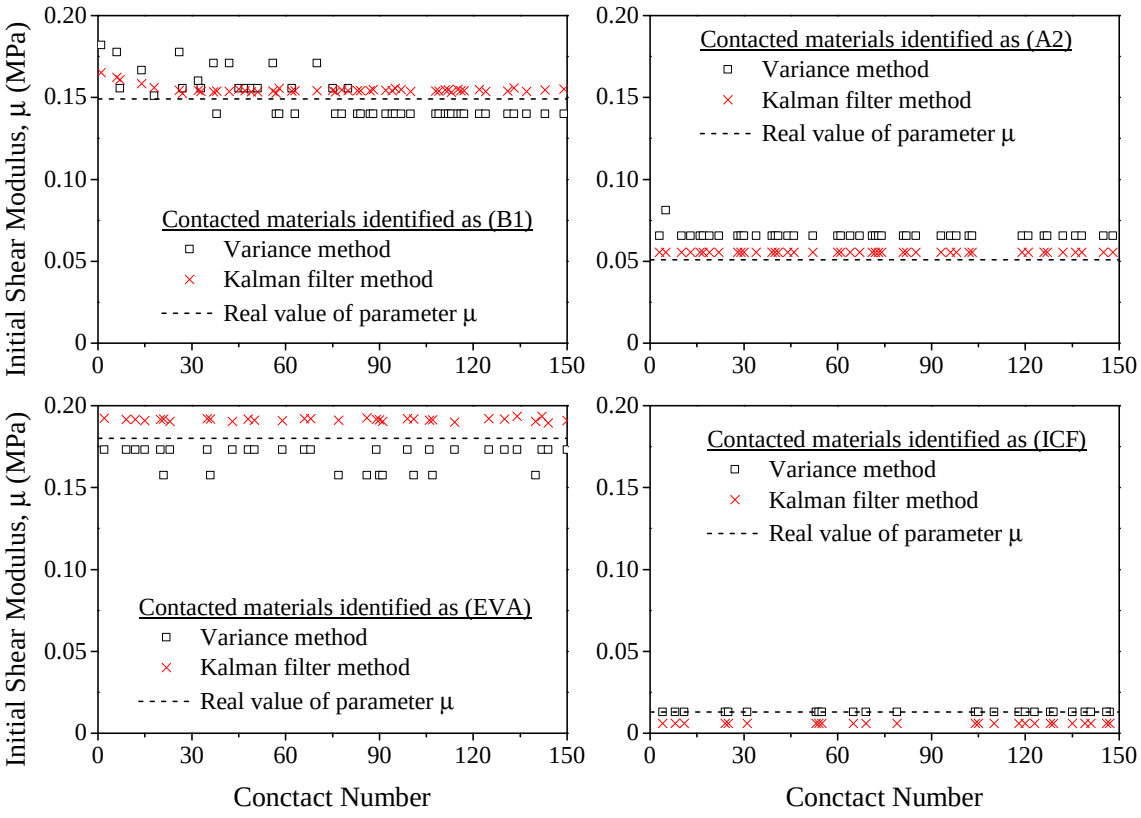

Figure 31: Identified initial shear modulus of specimens in real-time material identification using the variance and Kalman filter methods.

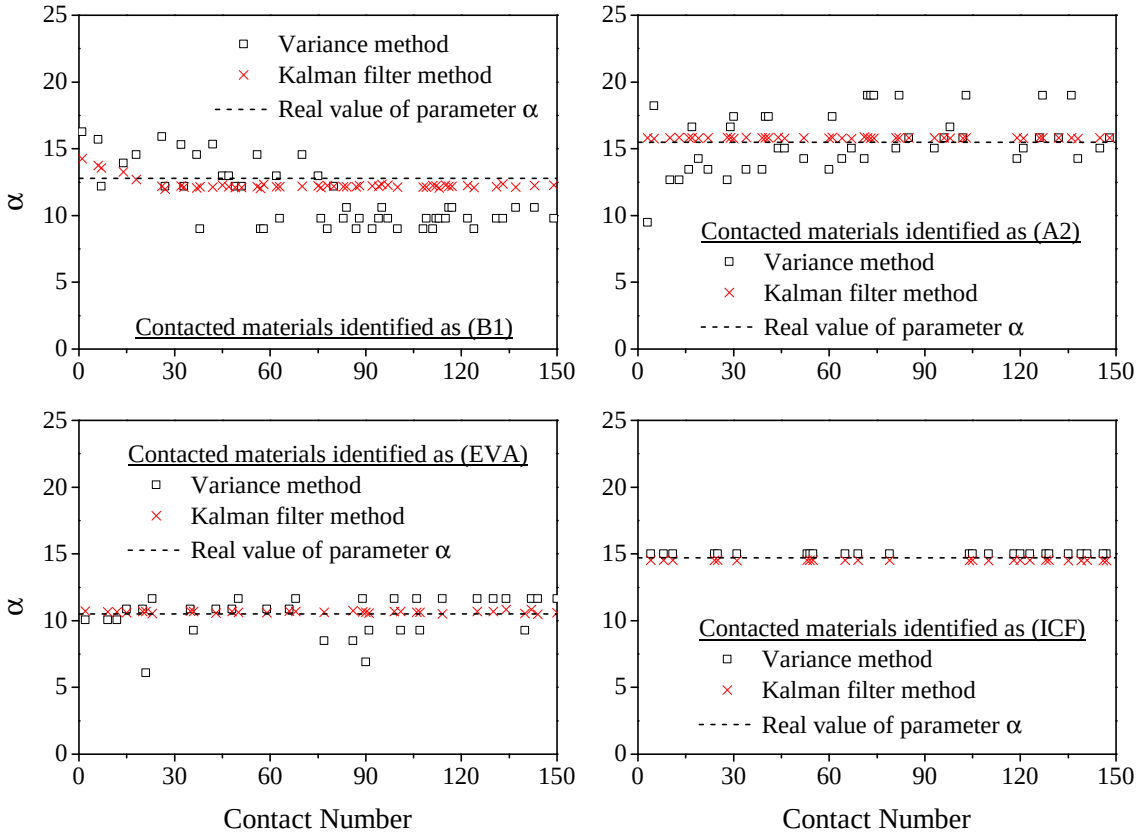

Figure 32: Identified parameter (α) of specimens in real-time material identification using the variance and Kalman filter methods.

In Table 3, the statistical results are tabulated for real time identification experiments performed at various indentation rates using the variance measurement method. The same seed was used for the random number generator. In each experiment, B1, A2, EVA and ICF are contacted 50, 42, 34 and 24 times, respectively.

Also, as can be seen in Figs. 31 and 32, the Kalman filter yields higher accuracy compared to the variance method at the same indentation rate. Experiments were performed at an indentation rate of $V = 2$ mm.s^{-1}. Scatter points are the outputs of identification algorithm for each material. Dashed lines represent the value of μ

parameter obtained from inverse modeling with global method of MultiStart optimization based on Nelder-Mead algorithm. The Penalty method was employed for bounded estimation with the Kalman filter. The statistical result of material recognition using the Kalman filter method is shown in Table 4.

Table 4: Statistical results of real time identification at various indentation rates using the Kalman filter method.

Successful recognition percentage (%)				
B1	A2	EVA	ICF	Total
98.3	100	99.6	100	99.3

In order to compare the performance of the bounding methods, a reference database was prepared and an indentation force curve used for identification purpose of material properties in which the initial shear modulus was very close to the boundary of the feasible region. In this benchmark, reference data was selected between the ranges of $0.5 < \alpha < 24$ and $0.005 < \mu < 0.1$. An iterative task of identification was defined in order to estimate the material parameters using the Kalman filter method based on penalty, projection and nearest neighbor bounding algorithms. The initial estimate for the Kalman filter algorithm was selected as a variable, uniformly distributed on the state space (20×20 combinations of α and μ over feasible region). Results of this benchmark are shown in Fig. 33.

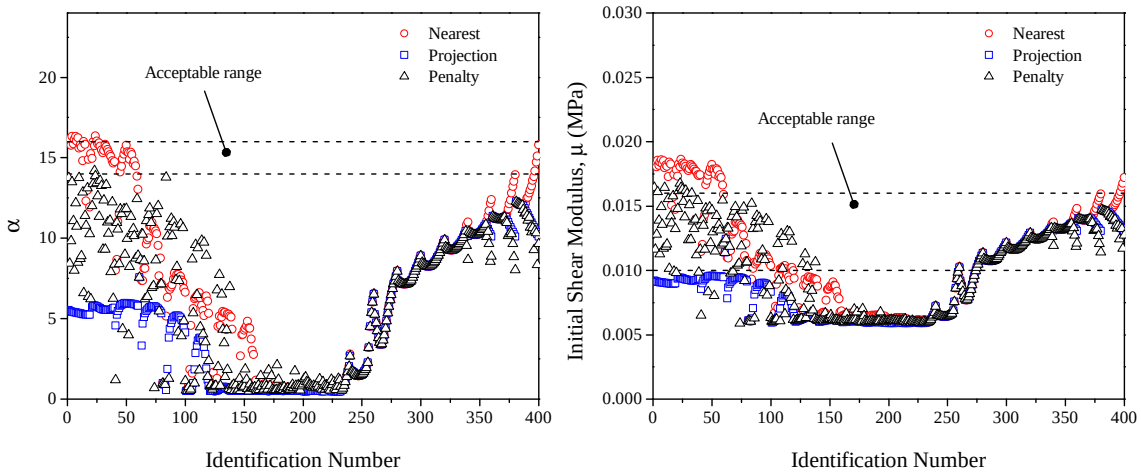

Figure 33: Comparison of identification results obtained using the penalty, nearest neighbor extrapolation and projection methods. Bounds of the acceptable range for each parameters are shown with dashed lines. The parameter to be identified (μ) is close to boundary of the feasible state space.

This specific identification task shows higher number of successful identifications obtained by the nearest neighbor bounding method in comparison with the projection and penalty methods. Also the penalty method exhibited a more successful estimation compared to the projection method. However, in a normal reference data (estimate variables at around central region of the parameter space), successful rate of the parameter estimation by the Kalman filter, bounded by the projection and penalty methods, was greater than the nearest neighbor bounding algorithm. For instance, a similar iterative benchmark of Fig. 33 was performed for identification with the Kalman filter but with estimation variables located around central region of the feasible state space. Results of this benchmark are shown in Fig. 34.

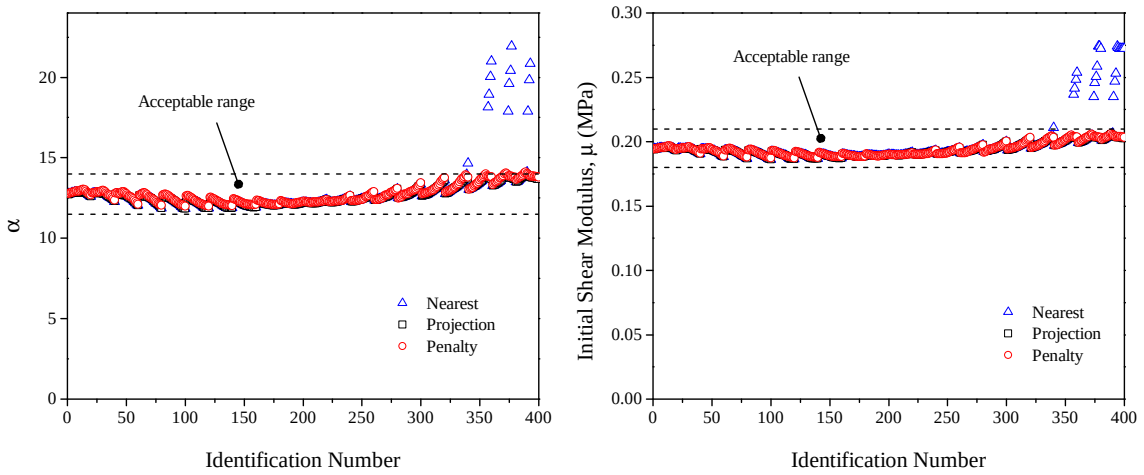

Figure 34: Comparison of identification results obtained using the penalty, nearest neighbour extrapolation and projection methods.

In Fig. 34, the bounds of the acceptable range for each parameters are shown with dashed lines. Parameters that are to be identified (α and μ) are at the central region of the feasible state space. As can also be seen, some of the identifications with the nearest neighbor method did fail but, however, all the identifications using the penalty and projection methods were successful.

Real time implementation of any algorithm demands a minimal amount of processing power to guarantee successful execution. In this research, the ratio of processing time (CPU time) in relation to the elapsed wall clock time was used as a criterion to measure the required processing power for either the variance or Kalman filter identification methods. For this purpose, one-thousand identifications tasks were defined and performed using both methods in which the duration of each task was governed by the indentation rate. For example, for an indentation rate of 2 mm.s^{-1}, each

identification task took two seconds to perform, assuming that the identification being performed was with an indentation up to of 4 mm in depth. Measurement was performed for each method on a workstation using the Matlab software running in single processing core mode at high priority to ensure least CPU time sharing in the operating system. All calculations were run on an Intel® Core™ i7-3770 at 3.9 GHz with 16 GB RAM with Windows 7 64-bit and MATLAB® R2014a. The CPU time for the defined repetitive task was measured at 1.513 seconds and 1,304.61 seconds for variance and Kalman filter methods, respectively. As can be seen, the variance method is very cost effective in terms of computation time compared to the Kalman filter method. In fact, in the same CPU configuration, real time identification at an indentation rate of 4 $mm.s^{-1}$ would not be possible due to the required CPU time of 1,304.61 seconds which is greater than the duration of the indentation process. It should be noted that the majority of elapsed CPU time in the Kalman filter method is related to the interpolation step which is, in fact, assumed as being an advantage over the variance method. However, as the results show, this advantage costs about 900 times more in term of the processing power.

3.5 Conclusions

In this chapter, two methods of real time parameter identification were proposed for nonlinear soft materials. The proposed methods were based on variance calculation and parameter estimation using the Kalman filter algorithm. Both the methods were

based on inverse FE modeling of mechanical indentation test. The FE model of indentation was pre evaluated in feasible range of material parameters and used as a reference data source for both the methods. Results were illustrated and compared in terms of precision and computing time. It was found that the variance calculation method required much less computation time compared to the Kalman filter method, which makes it suitable for real time identification procedures at high indentation rates. Although the Kalman filter method showed less scattering in identified parameters, it was prone to failure and, in some cases, was unable to achieve good convergence characteristics in contrast to the variance method. The proposed bounding methods for the Kalman filter estimation were implemented and their results compared. It was found that the Nearest Neighbor extrapolation method yields better results in certain estimation processes such as if the estimate is selected on the state space boundary. However, during the normal identification processes, the Projection and Penalty methods yielded better results compared to the Nearest Neighbor method. The performance of both algorithms were assessed in material parameter identification and was found to yield a performance success rate of greater than 90% based on experiments in which random indentations (150 indentations per experiment) and three different indentation rates were employed. It was also found that increasing the indentation rate leads to more accurate and repeatable results, which perhaps is due to the reduced viscous behavior of the studied materials. Identification results, from both the variance and Kalman filter methods, were found to be comparable. However the way these methods work leads to discrete estimate space for the variance method

and continuous space for the Kalman filter method with less scattering. Two methods of bounding were proposed for the Kalman filter parameter estimation based on Nearest Neighbor extrapolation and the Penalty method. The bounded estimation of the Kalman filter, using the two proposed methods, was found to be more accurate compared to the conventional projection method. The required processing time was found to be considerably less for the variance method compared to the Kalman filter method. However, the variance method was found to be more suitable for real time application of identification with higher indentation rates in robot assisted MIS. The advances in the techniques of determining the nature of material properties by artificial means, as detailed in this paper, has undoubtedly pushed the frontiers of knowledge of a hitherto little understood and somewhat neglected field. Our purpose and ambition is to undertake more research in order that the use of tactile sensor devices, and its use in MIRS for every conceivable kind of surgical procedure, will soon become *de rigueur* among the medical fraternity at large. In view of the strides that we have made over the past decade, that day can surely not be far away.

Chapter 4

Design and Model-Based Control of Magnetorheological Fluid-Based Softness Display

Softness displays are generally used to replicate the behavior of a range of virtual materials or objects. How realistically a softness display can recreate real and virtual materials, depends on the interaction between the pad of the finger and the softness display. One of the main parameters in human softness perception is the area between the pad of the finger, and any material with which it comes into contact. In order to display the degree of softness of the material, it is necessary to either have complete control of the surface geometry of the material with which the finger pad makes contact or to replicate the mechanical behavior of the soft material itself. In this research, Magneto Rheological Fluid (MRF) is employed in order to recreate the

nonlinear mechanical behavior of a range of soft materials. A softness display is developed based on MRF and an algorithm is proposed for controlling the display by changing the yield strength of the MRF by varying the magnetic flux density. A Finite Element Model (FEM) of interaction between the finger pad and soft materials is developed and used for design of a model based controller for the display. The curves of the contacted area versus contact force, resulting from interaction of the finger pad and the proposed display, are validated in experiments and found to be in good agreement with the FEM. The design and control algorithm of the softness display, finite element model and experimental results are presented and discussed in this chapter.

4.1 FE Model of Finger Pad Interaction with Soft Materials

In this research, human finger pad interaction with soft materials and rigid bodies is modeled using the FE method. Four main components of the human finger pad that are considered in the FE model are skin, subcutaneous tissue, bone and nail. Dimension and geometry of the finger pad components were chosen based on the anatomy of an average male index finger [114]. The schematic of the two-dimensional model is illustrated in Fig. 35. In this figure, (a) shows the schematic of the basic components of the human finger pad in distal phalanx; (b) shows the 2D FE model geometry, extracted from cross section of finger pad as well as boundary conditions

related to a hard contact condition; and (c) shows boundary conditions for a soft contact case. The constant velocity boundary condition, V, applied on three nodes at the center of the bone. The mechanical properties of the finger pad components are modeled based on published data [115]. Nail and bone are assumed as being linear elastic whereas skin and subcutaneous tissue are modeled based on hyperelastic and viscoelastic mechanical behavior, respectively. The material properties used in the finger pad model are presented in Table 5. The Ogden strain energy potential function is used for defining hyperelastic behavior and the Prony series is used as being a constitutive model of viscoelasticity.

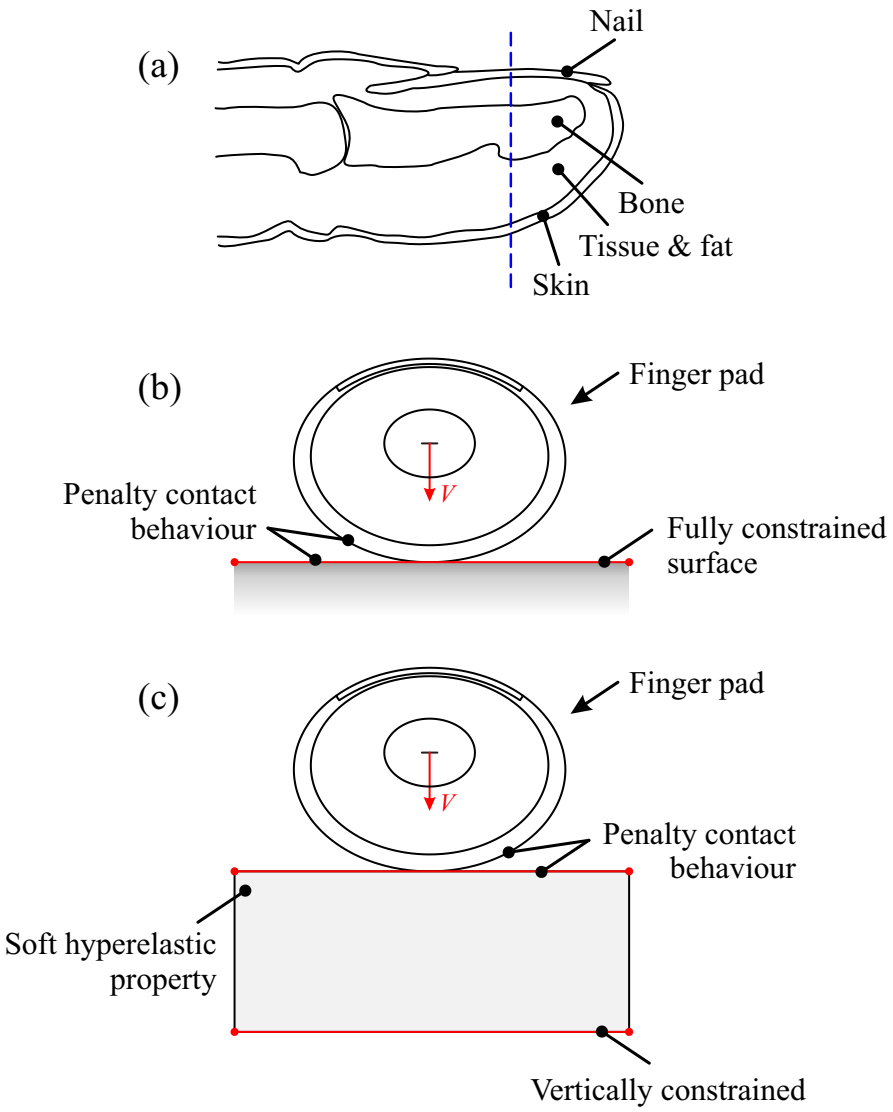

Figure 35: (a) Schematic of basic components of human finger pad in distal phalanx. (b) 2D FE model geometry, extracted from cross section of finger pad. (c) Boundary conditions for a soft contact case. Constant velocity boundary condition, V, is applied on three nodes at the center of the bone.

Table 5: Mechanical properties of the human finger pad components and Hyperelastic foams used in the FE model [115]

		Skin	Tissue	Bone	Nail	EVA	ICF
Density	ρ (Kg/mm^3)	1.0×10^3	1.0×10^3	2.7×10^3	2.0×10^3	92.0	50.0
Elastic	E (MPa)			17.0×10^3	17.0		
	N			0.3	0.3		
Viscoelastic	g_1	8.64×10^{-2}	0.2566				
	g_2	0.2136	0.383				
	τ_1 (s)	0.2136	0.223				
	τ_2 (s)	8.854	4.68				
Hyperelastic	α_1 (MPa)	1.3416	-2.06				
	α_2 (MPa)	25.0	25.0				
	α_3 (MPa)	-7.85	-3.47				
	α_4 (MPa)	-10.89	-4.48				
	μ_1 (MPa^{-1})	6.37×10^{-3}	2.35×10^{-2}				
	μ_2 (MPa^{-1})	1.88×10^{-4}	4.54×10^{-5}				
	μ_3 (MPa^{-1})	-3.77×10^{-3}	-4.08×10^{-2}				
	μ_4 (MPa^{-1})	1.84×10^{-3}	1.93×10^{-2}				
Hyperfoam	μ (MPa)					0.22	1.37×10^{-2}
	α					10.17	14.8

The driving force for pressing the finger pad against the rigid and soft materials is generated by muscles in the finger, wrist and arm. The resulting force is transferred to the contacted material through the skin, tissue and bone in the finger pad. Therefore, the driving boundary condition in the FE model is applied to nodal points at the center of the finger pad bone component as shown in Fig. 35(b), and the reaction force is calculated as being the sum of the reaction forces on these nodal points. In order to simplify the model and avoid undesirable effects of dynamic finger movement, a constant velocity boundary condition is applied in the vertical direction toward the contacted material with relatively low displacement rate of 2 mm.s^{-1} in order to avoid inertial force and impact loading effects [60, 61].

4.1.1 FE Model Validation in Hard and Soft Contact Experiments

Experiments of finger pad contact with rigid and soft surfaces are performed and the resulting contact area and contact force are measured for validation of the developed FE model of the finger pad. In these experiments using the test setup as shown in Fig. 36, three subjects were requested to push their ink-stained index finger against surfaces of a soft polymer as well as a rigid plate which were covered by a thin cloth and paper sheet in order to capture and measure the contact area. A force sensor was placed under the rigid plate and block of the soft polymer to measure and record the contact forces. First, while viewing a force indicator on the computer monitor, subjects were asked to push their index finger against a rigid plate with various

forces, starting with a very slight pushing force of about 0.5 N, and then gradually increasing to 10 N. After each contact, the paper sheet was readjusted to record a new fingerprint while the force sensor recorded the force data continuously. The same experiment was repeated using soft polymeric foams. The test setup is shown in Fig. 36.

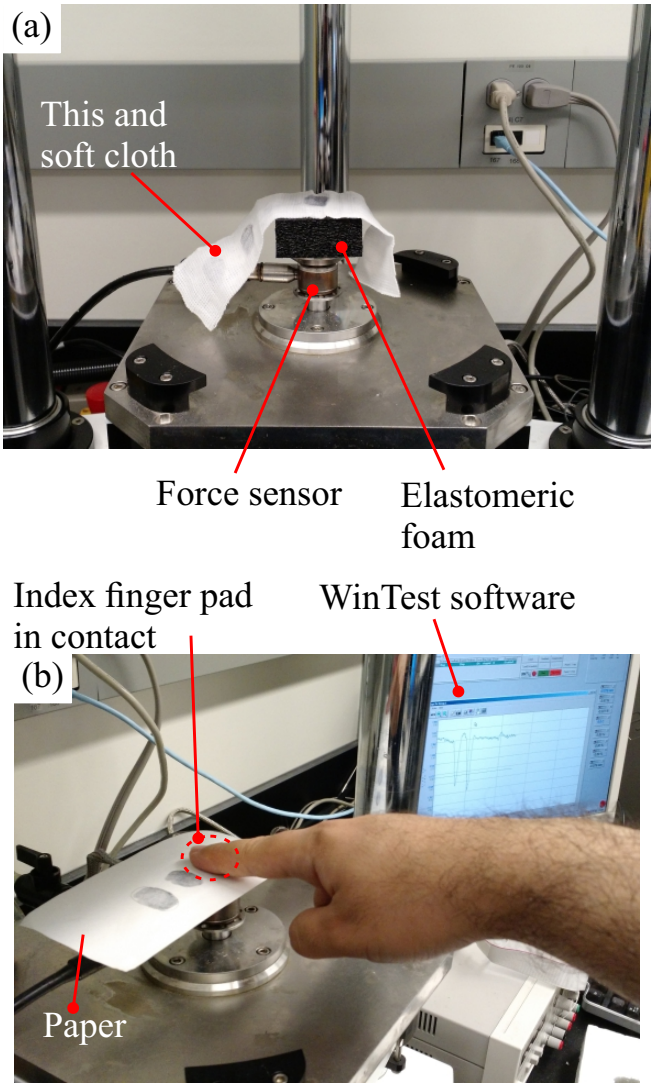

Figure 36: Test setup of the finger pad contact with rigid and soft materials.

Curves of the contact area versus the contact force were generated from recordings

of the force sensor by measuring the pertaining contact area from fingerprints formed on the thin cloth and paper sheets. As can be seen in Fig. 37, the contact area of the sample captured finger prints for both the rigid and soft contacts possess an elliptical shape. Assuming a perfect ellipse for the shape of the contact region, areas of the contact were calculated by measuring two radiuses of the elliptical finger prints.

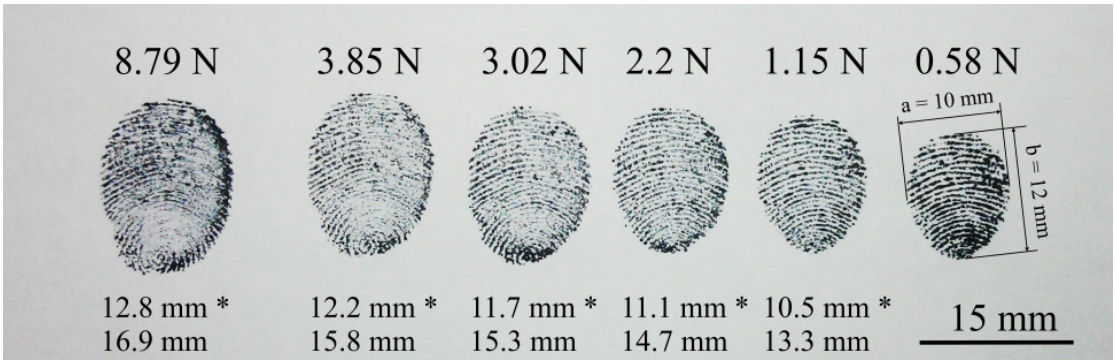

Figure 37: Finger prints recorded for the purpose of contact area measurement.

Similar data was acquired from the FE model of the finger pad contacted with the rigid surface and deformable foams with nonlinear elastic (hyperelastic) material behavior. Material properties of hyperelastic foams used in this investigation are shown in Table 5. Hyperfoam constitutive model of Abaqus software was employed for definition of the deformation behavior of foams. Since neither the amount of indentation in the soft material nor vertical displacement of the finger pad was recorded in the soft and rigid contact experiments, the contact area was calculated against the contact force. The resulting curves and data points of the contact area versus the contact force are presented in Fig. 38. As it can be seen in this figure, there is a good agreement between the experimental data points and FE model curves of the contact

area versus the contact force.

In Table 5, materials used were ½ inch. thick (closed cell ethylenevinyl acetate (EVA) and 1 inch thick PVC/NBR (ICF) polymeric foams. Since EVA and ICF are assumed as being fully compressible materials, Poisson's ratio is therefore set to zero. As can be seen in Fig. 38, the measured experimental data conforms to the equivalent calculated curve from the FEM.

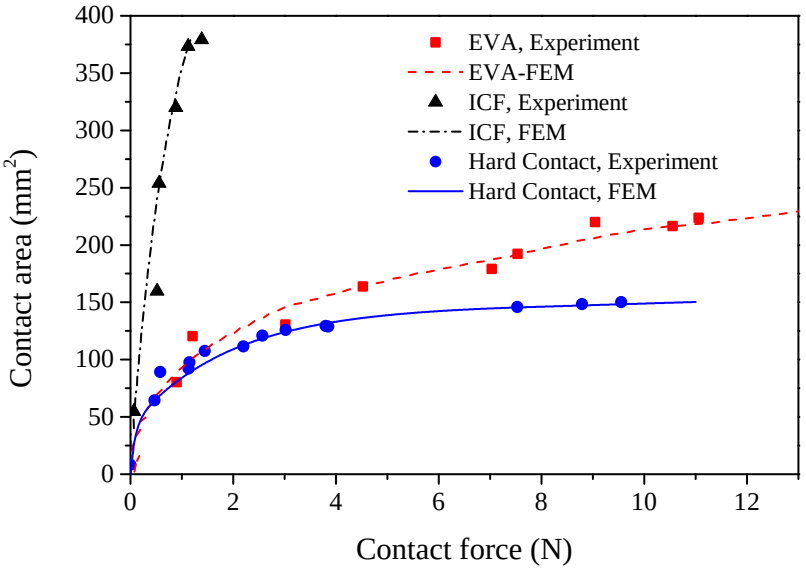

Figure 38: Data points of contact area and contact force measured in the experiment compared to the contact area and contact force curves calculated from the 2D FE model.

4.1.2 Axisymmetric FE Model of the Finger Pad

In addition to the 2D model explained in this section, the finger pad contact with soft materials is modeled in an axisymmetric mode as well. As it can be seen in captured finger prints in Fig. 37, the contact area for both the hard and soft contacts possess an elliptic shape, which is not in agreement with the circular and spheroidal cap shaped contact areas calculated by axisymmetric FE model. In reality, contact surface in hard

and soft contacts of human finger pad, possess elliptic flat and ellipsoidal cap shapes. Therefore, correction factors are required to compensate the deviation in results due to axisymmetric assumption in the FE model. Elliptic and ellipsoidal cap shaped contact surfaces are schematically shown in Fig. 39. Assuming that shape of the obtained finger prints from hard contact experiments are perfect ellipse, a correction parameter is derived from finger prints as ratio between two diameters of the ellipse. As shown in Fig. 39a, having this correction parameter, the obtained hard contact area from axisymmetric model can be converted to the equivalent elliptic contact area of finger pad with rigid surface. Similarly, assuming a perfect oblate ellipsoid cap shape (Fig. 39b) contact area in soft contact between finger pad and soft materials, a correction factor is achieved for converting the calculated spherical contact area from two dimensional axisymmetric model to equivalent ellipsoidal contact area in three dimensions.

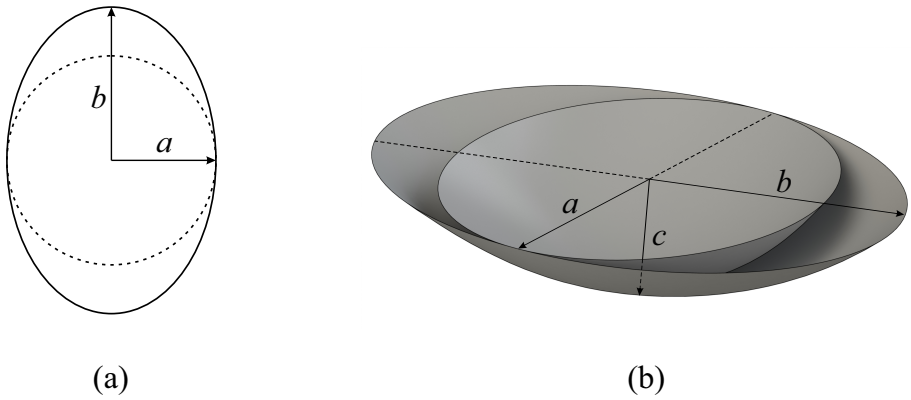

Figure 39: Schematic of ideal contact areas measured from captured finger prints and calculated from FE models. (a) Hard contact surface area obtained from hard contact of symmetric finger pad (ellipse of radii a and b), and axisymmetric FE model (circle of radius a). (b) Soft contact surface area obtained from soft contact of symmetric finger pad (ellipsoidal cap of base radii a, b and c), and axisymmetric FE model (spherical cap of base radius a).

The contact area in axisymmetric model of finger pad in contact with rigid (hard) surface ($A_{H,A}$), is calculated from the length of the contact line a, as radius of circular contact surface, as illustrated in Fig. 40. The correction factor k, is defined as ratio between radii of the elliptic finger prints, a and b of Fig. 39a. Therefore, equivalent symmetrical elliptic contact area ($A_{H,S}$) was calculated as following:

$$A_{H,A} = \pi a^2 \tag{28}$$

$$k = \frac{b}{a} \tag{29}$$

$$A_{H,S} = \pi ab = k\pi a^2 = kA_{H,A} \tag{30}$$

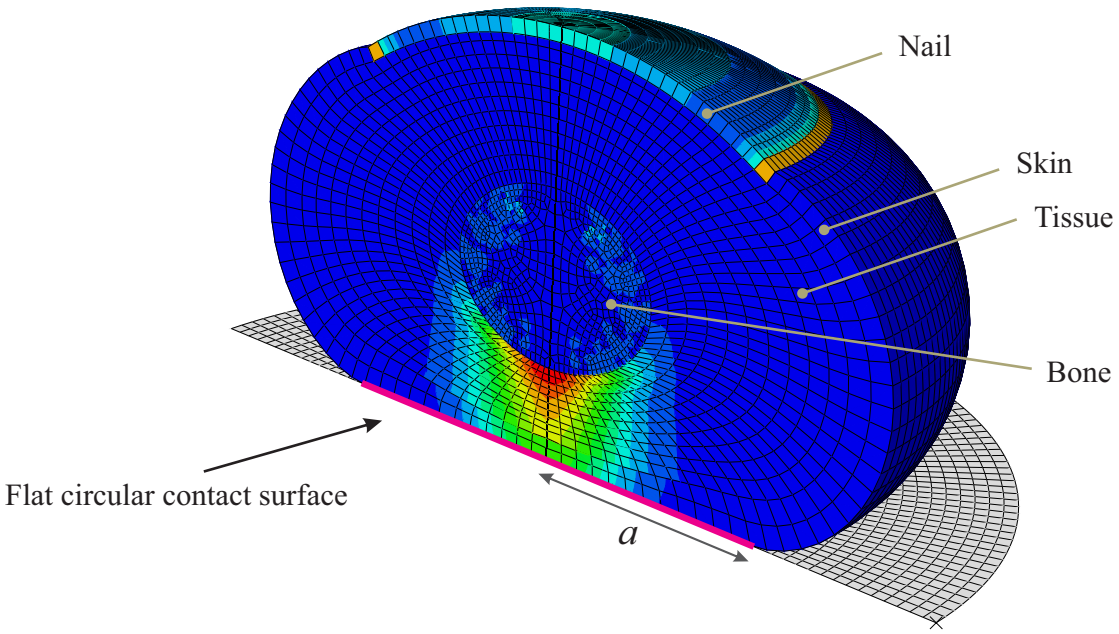

Figure 40: 180 degrees sweep of axisymmetric model of finger pad contact with rigid surface shown in Fig. 35. Circular contact area with radius a equal to the length of the axisymmetric contact line is illustrated.

On the other hand, in axisymmetric FE model of the finger pad in contact with soft materials, the contact area $A_{S,A}$ is achieved by calculating surface area of 360° revolution shape of base radius a and height c (Fig. 39b). The curved contact line is schematically shown in Fig. 41. The correction factor k is defined as ratio between two radii, a and b, of the elliptic fingerprints.

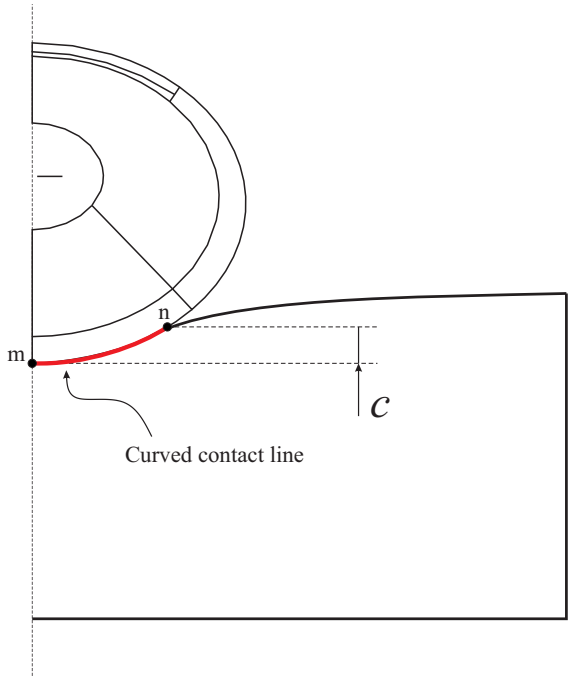

Figure 41: Illustration of the indentation depth c, and curved contact line in axisymmetric FE model of contact between finger pad and soft material. Points, m and n are beginning and end points of the contact line.

Assuming that the revolution shape is a spherical cap of radius r and height c, the contact area $A_{S,A}$ can be calculated as following:

$$A_{S,A} = 2\pi rc \tag{31}$$

The correction factor, k, is defined as ratio between two base radii a and b:

$$k = \frac{b}{a} \tag{32}$$

Indentation depth c, is illustrated in Fig. 41. It should be noted that, depth of the indentation is different from the amount of bone displacement or the displacement due to the velocity boundary condition. This difference is shown in Fig. 42. Indentation depth c, is calculated from the difference between vertical coordinates of lowest node of the finger pad model (beginning of contact line, point m in Fig. 41) and the varying node in contact at the end of the contact line (point n in Fig. 41). Also, it can be seen that the same moving boundary condition V_{ind}, in finger pad contact model on different soft materials, shows different indentation depths, which is a result of different deformation behavior. The difference in deformation behavior is also shown in Fig. 43 and as change in contact surface.

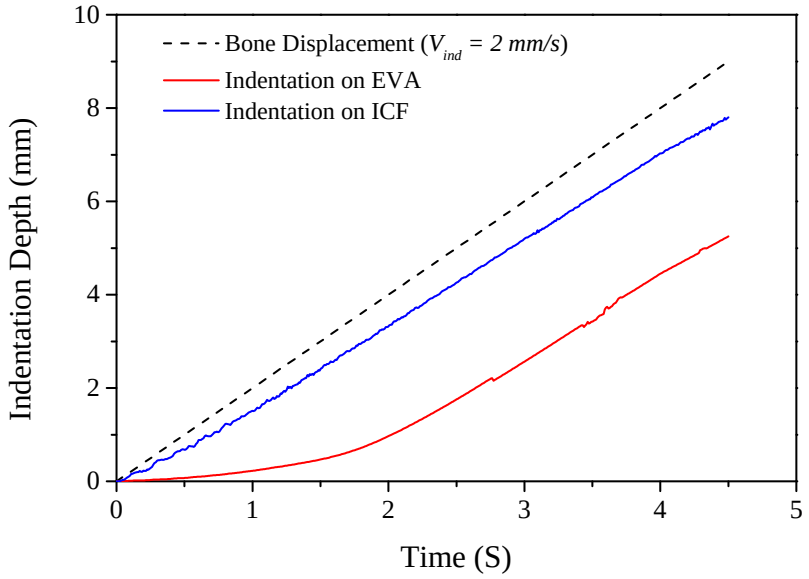

Figure 42: Comparison between depth of indentation and amount of finger bone displacement calculated by FE model of finger pad contact with two soft materials. EVA polymeric foam is harder than ICF foam, therefore under skin tissue is subjected to more deformation than the ICF foam, during the finger contact.

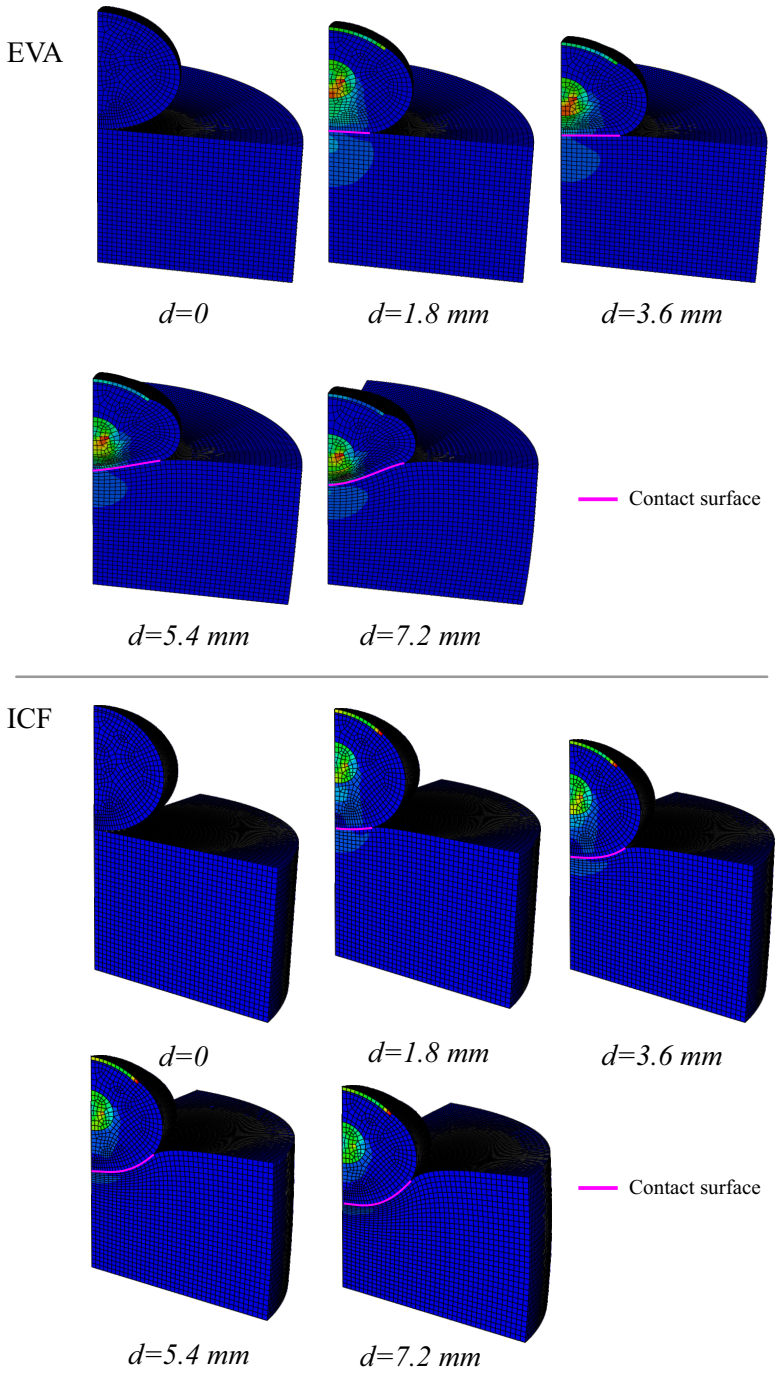

Figure 43: Change in contact surface between finger pad and polymeric foams (EVA and ICF). 90 degrees sweep of the axisymmetric FE model is constructed with Abaqus software.

Having the contact area $A_{S,A}$ and indentation depth equal to height of the spherical cap (c in Fig. 41), the main radius r, of the hypothetical sphere in contact with

the soft material is calculated as following:

$$r = \frac{A_{S,A}}{2\pi c}$$

This calculated contact radius for EVA and ICF foams is shown in Fig. 44

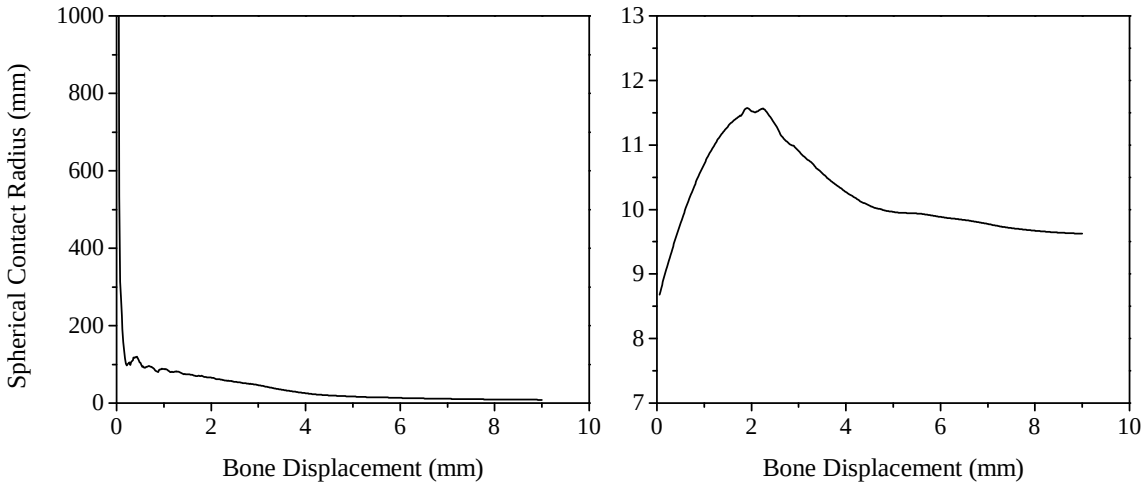

Figure 44: Instantaneous spherical contact radius extracted from FE model of finger pad contact with two different soft materials, EVA and ICF polymeric foams.

Equivalent symmetric contact surface is an ellipsoidal cap of base radii a, b and height of c with surface area of $A_{S,S}$. The ellipsoidal cap is constructed by 360° revolution of an elliptic curve. Parametric equations of ellipsoidal cap in spherical coordinates are as following:

$$x(u,v) = r_1 \cdot cos(u)sin(v) \tag{33}$$

$$y(u,v) = r_2 \cdot cos(u)sin(v) \tag{34}$$

$$z(u,v) = r_3 \cdot cos(v) \tag{35}$$

where u and v are spherical coordinates, and r_1, r_2 and r_3 are main radii of ellipsoid. Surface area of ellipsoidal cap can be calculated as:

$$A_{S,S} = \iint \left(sin(v) \sqrt{r_2^2 sin^2(v)(r_1^2 sin^2(u) + r_2^2 cos^2(u)) + r_1^2 r_2^2 cos^2(v)} \right) du \cdot dv \tag{36}$$

$$0 < v < acos\left(1 - \frac{c}{r_3}\right) \tag{37}$$

$$0 < u < 2\pi \tag{38}$$

Assuming that, two of the main radii of the ellipsoidal cap, r_1 and r_2, are identical, surface area of the resulted oblate ellipsoidal cap can be calculated by the instantaneous spherical contact radius r, shown in Fig. 44, correction factor k, in Eq. 32, and depth of the indentation c, shown in Fig. 42 which is used in upper bound of surface area integration (Eq. 37). Therefore, the contact surface is an oblate ellipsoidal cap of radii r and $k.r$, and height of c. Resulted contact area calculated by Eq. 36 is presented in Fig. 45.

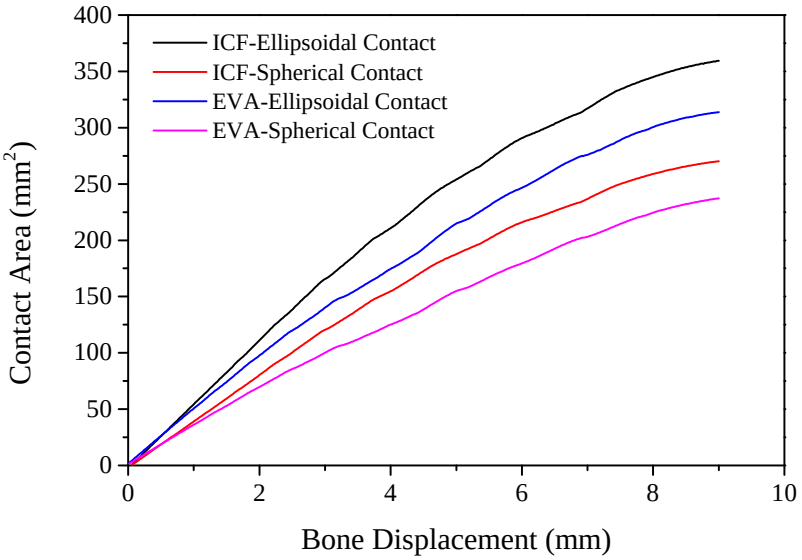

Figure 45: Ellipsoidal contact area between finger pad and soft polymeric foams, EVA and ICF, calculated from spherical contact radius, extracted from FE model, and correction factor extracted from finger prints.

In order to achieve the contact force versus the contact area curves using the updated contact area values shown in Fig. 45, the contact forces should also be interpreted from axisymmetric to symmetric mode. For this purpose, distribution of contact pressure and vertical contact force, on contact surface, in different analysis steps, are calculated and shown in Fig. 46. As it can be seen, major contribution of the reaction force and the contact pressure are transferred to the bone of finger pad from central section of the model. It can be concluded that in a horizontally stretched model, increase in contact force would be negligible in comparison to increase in contact area. In order to prove this supposition, geometry of the finger model is expanded horizontally with ratio equal to correction factor. The same indentation analysis is performed on EVA foam. Result of this analysis is shown in Fig. 47 in a sample time step. As it can be seen in this figure, magnitude of the vertical contact

force is decreased in the stretched model and the extra force related to stretched portion of the contact surface (Distance from center beyond 8 mm in Fig. 47) is very negligible in comparison to the contact reaction force in whole contact surface. The overall increase in reaction force due to horizontally stretching of the finger pad model is calculated as 5.3%.

After calculation of both the changes in contact area and contact force, the interpreted curves of contact area versus contact force in symmetric model are presented in Fig. 48. As it can be seen in this figure, the measured experimental data conforms to the equivalent calculated and mathematically corrected curves from the FEM.

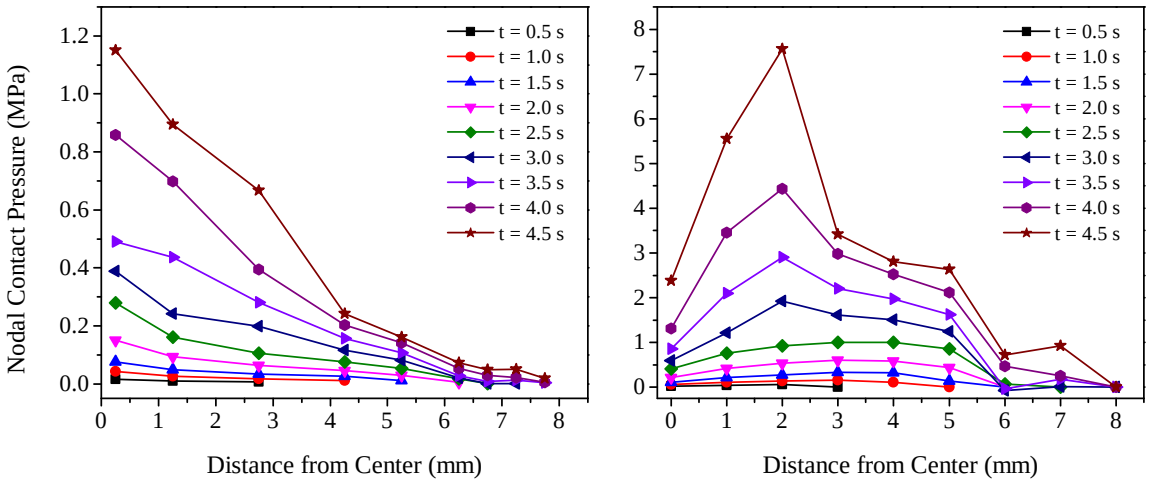

Figure 46: Distribution of contact pressure and vertical contact force on EVA polymeric foam in contact with finger pad. Contact pressures and vertical contact forces are calculated at element nodal points of contact surface.

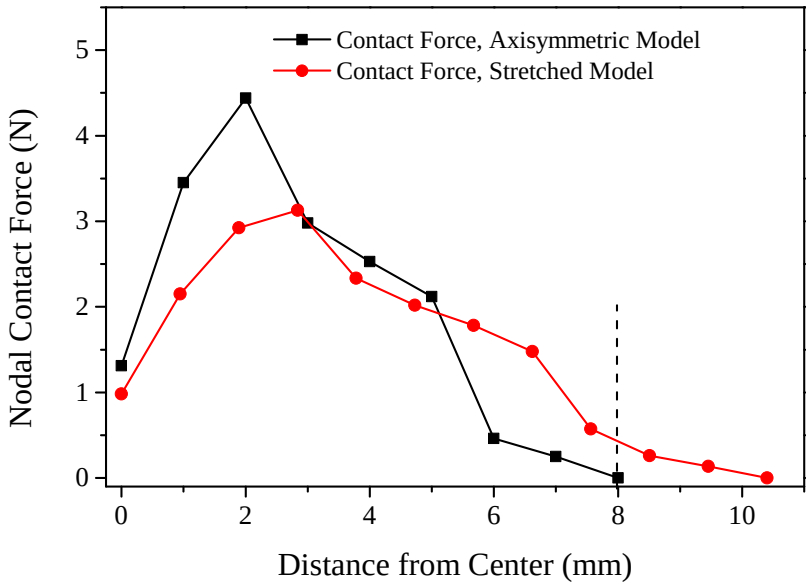

Figure 47: Contact force distribution in time step $t = 4.0$ s from original and horizontally stretched finger pad models.

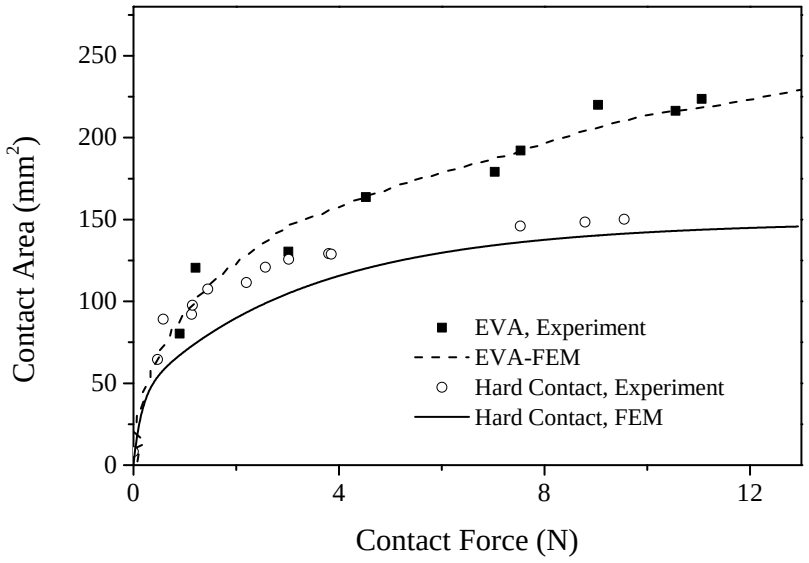

Figure 48: Contact area versus contact force achieved from finger pad contact experiment, and calculated from FE model of finger pad contact with rigid surface and soft polymeric foam. The calculated contact area and contact force data are corrected based on results from the experiment.

4.2 Design and Modeling of the MRF based Tactile Display

In order to have a compact design for the softness display, in which a relatively strong magnetic field is concentrated in MR fluid, various designs were studied using the finite element method (FEM). For this purpose, open source software FEMM 4.2 was employed to perform a 2D FE analysis on different designs. The employed 2D planar approach uses first-order triangle elements and is explained in [116]. A number of examined designs and related FE analysis results are presented in Figs. 49 and 50. Nonlinear $|B|$-H curve of Alnico[1] magnet is used in these analysis. As it can be seen in Fig. 50, the design (c) which represents a closed magnetic circuit shows higher and more uniform magnetic flux density within the modeled MR fluid.

As a result of these analysis, a ring-shape electromagnet design with a gap to locate the MRF container, was found to be the best for this application as it provides a closed magnetic circuit (by considering the MRF as a part of the magnetic circuit) and minimum waste of magnetic flux in the circuit. A hydrocarbon-based MRF from the LORD Corporation (namely MRF-122-2ED) is used in this work which is formulated for general use in controllable energy dissipating applications. Curves of yield strength and magnetic flux density, which are used in magnetic and mechanical modeling of the MR fluid, are provided by the producer. For the ring shape core of the electromagnet, 1018 steel is employed and 770 uniform turns of 28 AWG copper wire is used for

[1] Alnico is family of iron alloys which in addition to iron are composed primarily of aluminium (Al), nickel (Ni) and cobalt (Co).

the winding. Fig. 51 shows the display design that consists of three components, electromagnet with steel core, soft plastic container and magneto rheological fluid. As can be seen in Fig. 51, the MR fluid container has two holes and is placed at the gap of electromagnet ring in such a way that both ends of the ring are slightly inserted into the container internal area. Both ends are fully fixed and sealed to prevent MR fluid leakage. The result of the FE modeling is shown in Fig. 52 as colored distribution of magnetic flux density ($|B|$). The Nonlinear curve of magnetic flux density ($|B|$) versus magnetic field strength (H) in datasheet of MRF-122-2ED from Lord Corporation is used in the electromagnetic FE model. In order to validate the FE model results the flux density is measured at the center of the container, within the MR fluid, using a Gauss meter. However, since the presence of the Gauss meter probe has a disturbing effect on the magnetic field at this location, it is arranged for there to be an air gap in the FE model at the center of the container. Measured and calculated values of magnetic flux density at the air gap location are presented in Table 6.

The FE model is validated by noting the agreement in the readings between the actual and calculated values of the magnetic flux density.

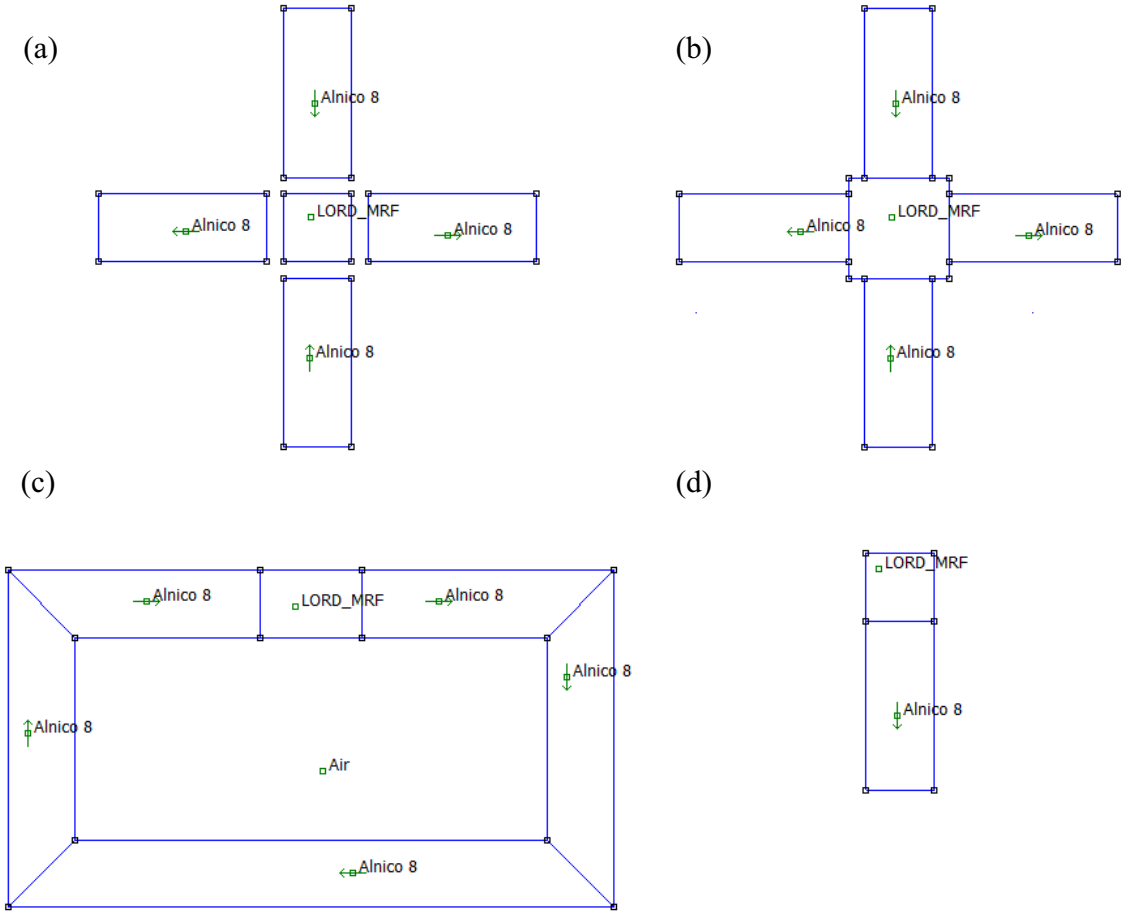

Figure 49: Sample designs examined for the electromagnet of the tactile display. (a) Quadrupole magnet array with separated MRF at the center. (b) Quadrupole magnet array and contiguous MRF at the center. (c) Closed circuit magnet design with MRF included contiguously in the circuit. (d) Single magnet design with contiguous MRF. Green arrows are representing the magnetization direction in each magnet segment.

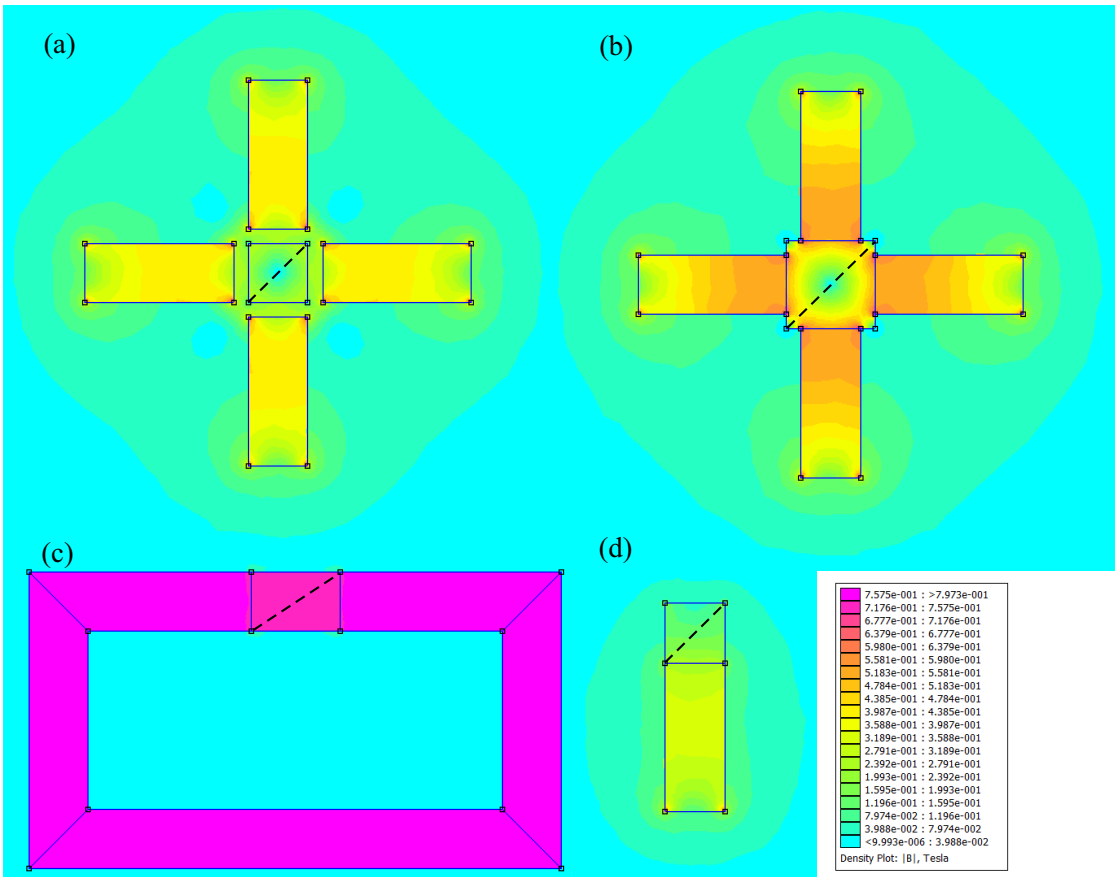

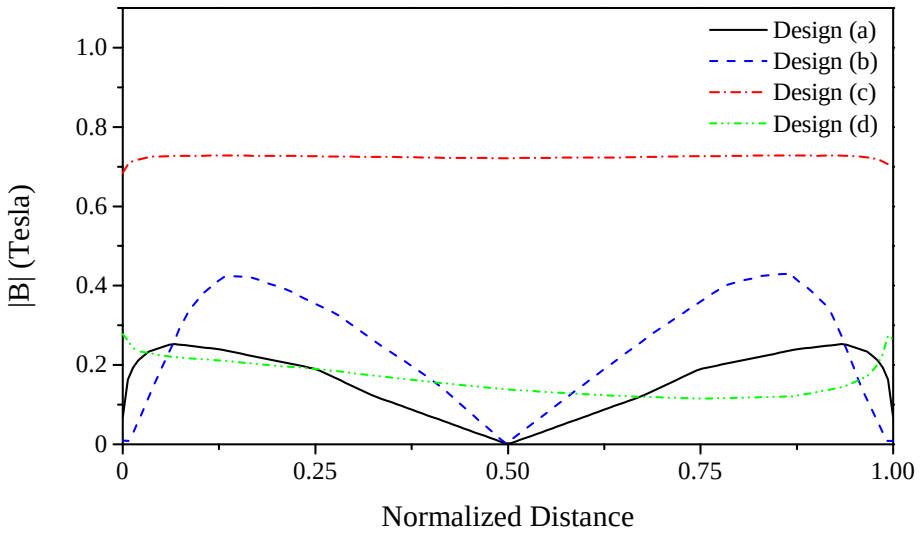

Figure 50: FE analysis of the designs shown in the Fig. 49. Flux density curves are calculated along the dotted line shown in each design.

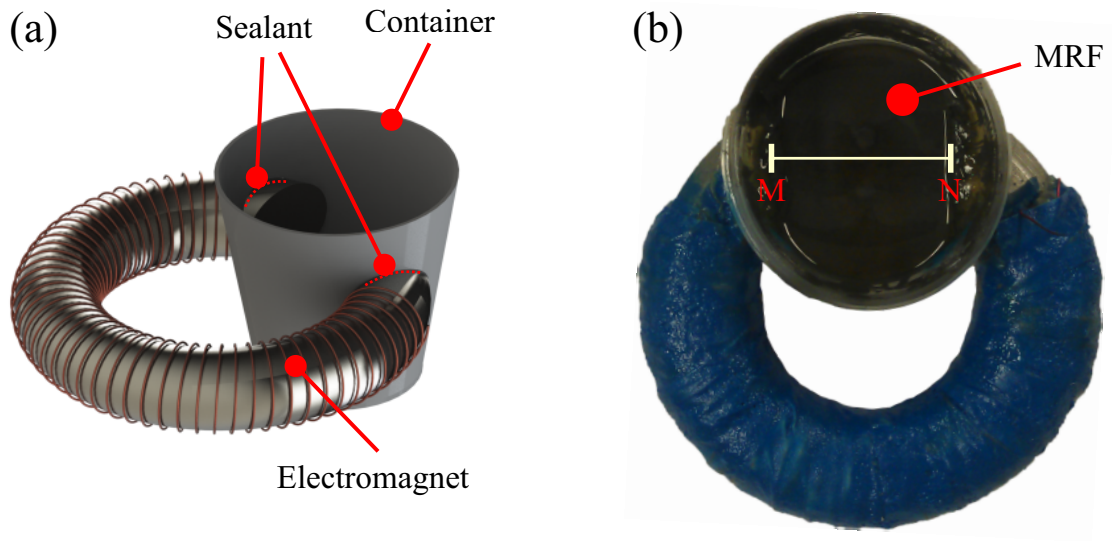

Figure 51: (a) Schematic of softness display based on MRF. (b) Prototype of the softness display. As a reference, length of the line MN is 30 mm.

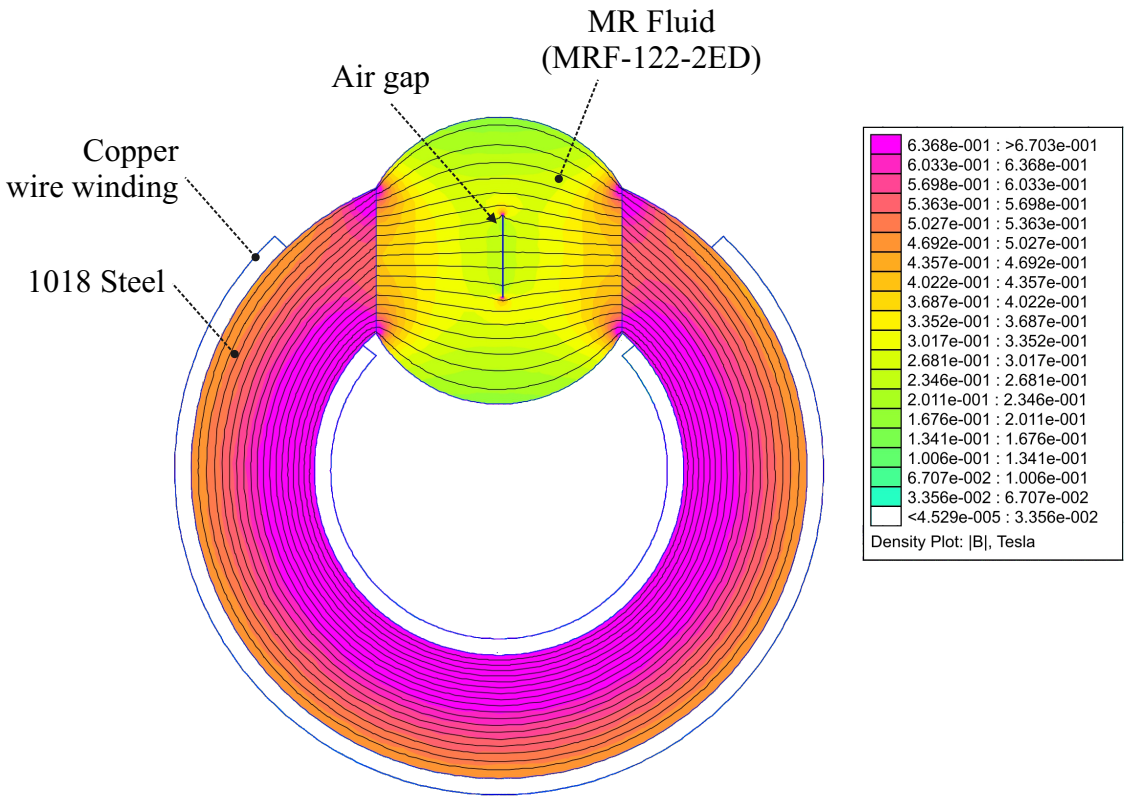

Figure 52: Magnetic flux density $|B|$ map in the electromagnet and MR fluid.

Table 6: Measured and calculated magnetic flux density.

$Current$ $(Amps)$	$Measured\|B\|$ $(Gauss)$	$FEM\|B\|$ $(Gauss)$
1.5	593	608
1.75	629	654
2.0	744	721
2.25	794	766
2.5	831	810

4.3 Model Based Control of the Plastic Deformation Behavior in MR Fluid for Softness Display

The yield strength of the MR fluid can be accurately adjusted by controlling the magnetic flux density within the MR fluid [117]. Therefore, the MRF can transmit a variable force by means of a controllable electromagnet. Fig. 53 shows the variation of yield strength with magnetic field strength for the MRF used in this research using the magnetic and mechanical properties of the said magneto rheological fluid. This nonlinear curve of magnetic flux density (B) versus magnetic field strength ($|H|$) is used in our electromagnetic FE modeling.

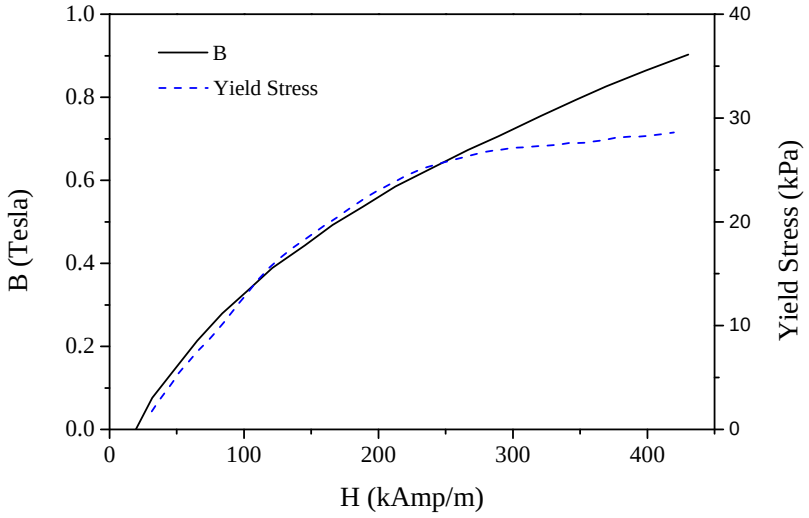

Figure 53: Nonlinear curves of magnetic flux density $|B|$ and yield stress versus magnetic field strength H.

By employing an electromagnet and current control circuitry, the viscoelastic and plastic (yield strength) properties of MRF can be controlled. For applications such as softness displays, which involve relatively large amounts of deformation, the yield strength of the MRF would be of more interest. Since the human softness perception mainly occurs in the loading stage, unloading or material's elastic recovery step would not affect the whole perception process [54]. Therefore, having control on the yield stress would be sufficient for recreating any arbitrary stress-strain loading path.

In this research, we have investigated the feasibility of replicating hyperelastic material behavior by means of an MR fluid-based softness display. Since hyperelastic materials ideally possess elastic mechanical behavior in which the stress is determined by the current state of deformation, a nonlinear relationship exists between the stress and the strain in these materials.

The ability to replicate any stress-strain curve, in the loading cycle only, is demonstrated with an FE model of compression test with variable yield strength material property. Fig. 54 shows examples of compression tests in the FE model with material properties of varying yield strengths. These models are developed using the Abaqus software in which the yield strength is defined by field variables as a function of displacement of moving platen boundary condition. These examples theoretically show the possibility of producing arbitrary nonlinear stress-strain curves in homogeneous deformation modes (e.g. standard compression) by controlling the yield strength of whole bulk of the material. However, non-homogeneous deformation modes (e.g. deformation of soft material due to human finger pad contact) would require localized control over the yield strength within the bulk of the MRF. For example, non-homogeneity of stress distribution in a non-homogeneous deformation mode is shown in Fig. 55 using the FE model of the human finger pad in contact with a soft material. This result shows a spectrum of stress within the material at each moment of the deformation unlike the stress field in uniform deformation modes. Therefore, an average of the distributed stress is used to regulate the yield strength of the MRF or the electrical current in the electromagnet of the proposed display.

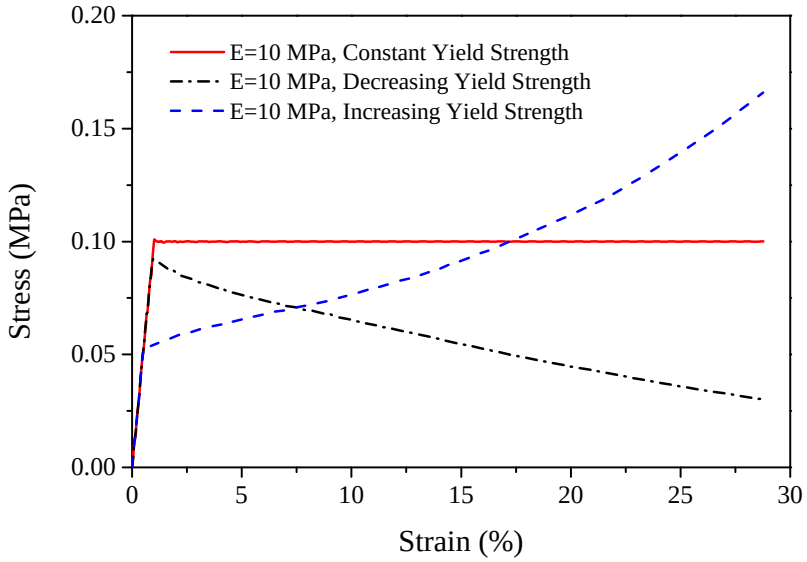

Figure 54: Stress-strain curves achieved by a FE model of a standard compression test with elastic and variable plastic material properties.

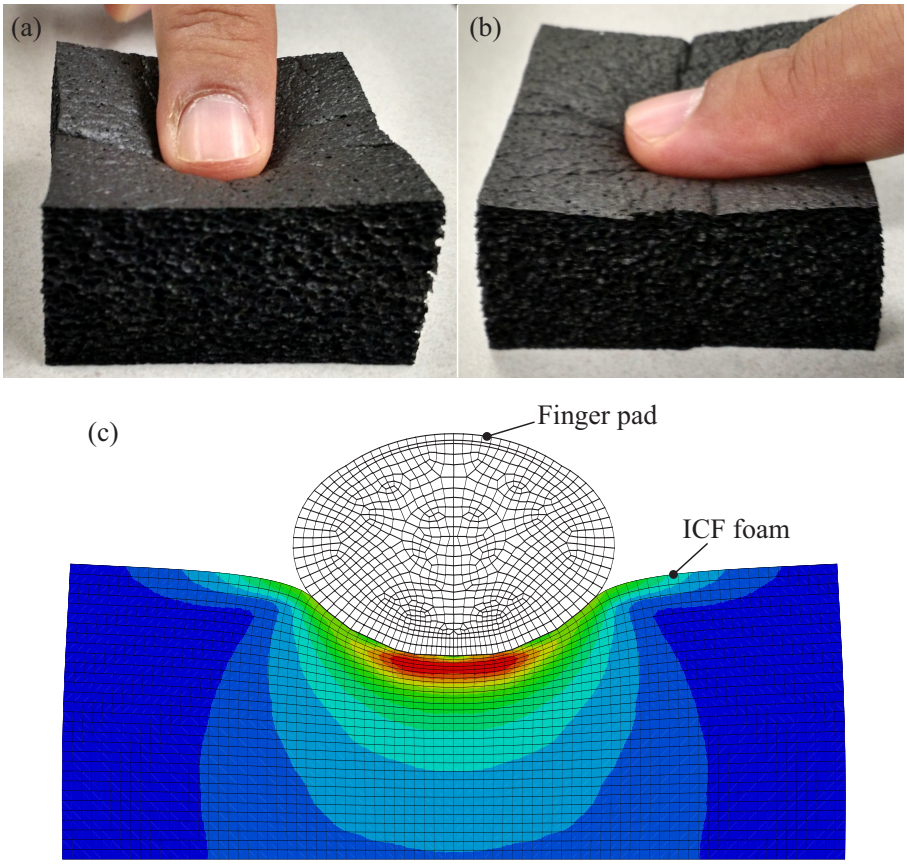

Figure 55: (a) and (b) deformation of ICF foam due to contact of the finger pad. (c) Mises stress distribution in ICF foam deformed due to contact of the finger pad.

The developed finger pad FE model is employed to extract the Mises stress at all nodal points of the soft contacted material at each time increment of the simulation. Fig. 56 shows normalized distribution of the Mises stress values in this model for the ICF elastomeric foam in contact with the finger pad. This histogram is calculated with a bin size of 1 KPa. PVC/NBR polymer (ICF400) soft foam material property is used for this model which possesses hyperelastic material behavior. Different yield strength control scenarios are examined in this work using the FE model. Three different yield stress control curves are achieved by calculating mean, median and geometrical mean

of the Mises stress values of all the nodal points of the soft deformed material versus the finger bone displacement. The same FE simulation is performed using these curves as the material property in form of the variable yield strength. Then, in order to decrease the error in reaction force and contact area between curves achieved by actual material property and equivalent property of variable yield strength, an optimization task is defined and performed. A cubic polynomial is considered for the control curve and three coefficients of the polynomial are optimized to minimize the difference in curves of the contact area and the reaction force.

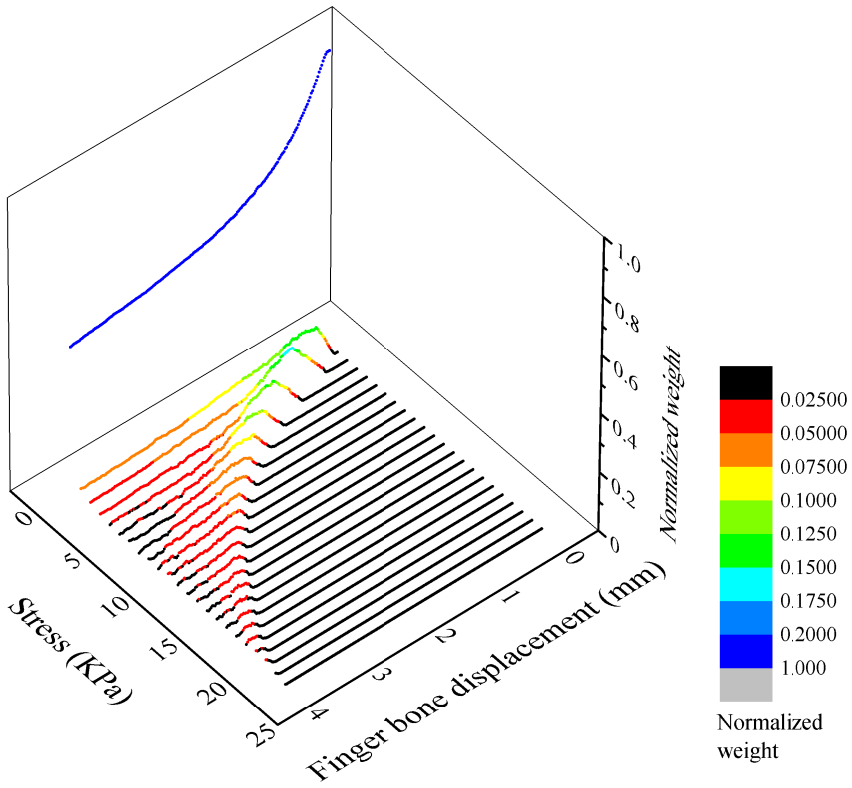

Figure 56: Mises stress distribution at nodal points of the ICF soft foam in contact with the finger pad in the FE model. The graph is achieved by extracting the Mises stress values at nodal points of the ICF foam model (shown in Fig. 55) at each step of finger movement toward the ICF foam.

The achieved yield strength curves, and results of FE simulation using these curves, are shown in Fig. 57 and Fig. 58. As can be seen, the geometrical mean and median yield relatively less error compared to the regular averaging. On the other hand, the optimized yield strength curve resulted in optimum contact area and reaction force among all these curves.

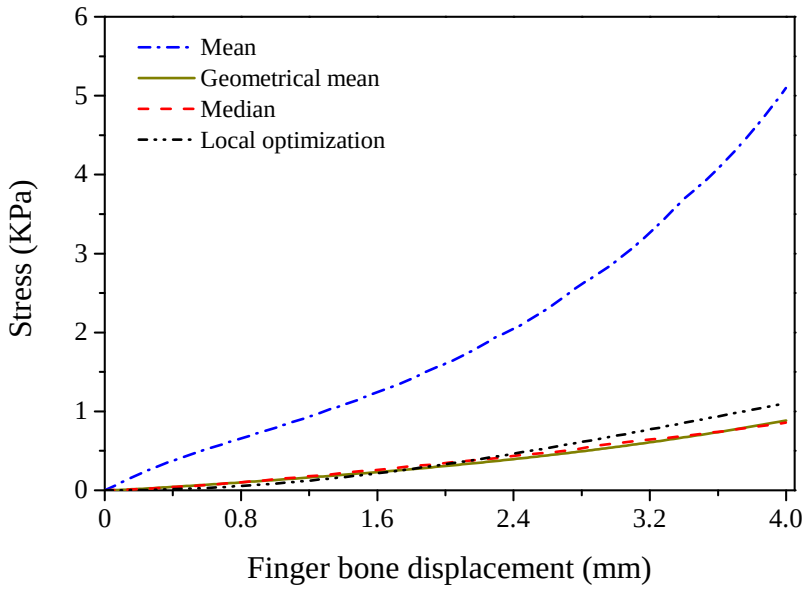

Figure 57: Different control curves achieved by various average methods over Mises stress values and optimization.

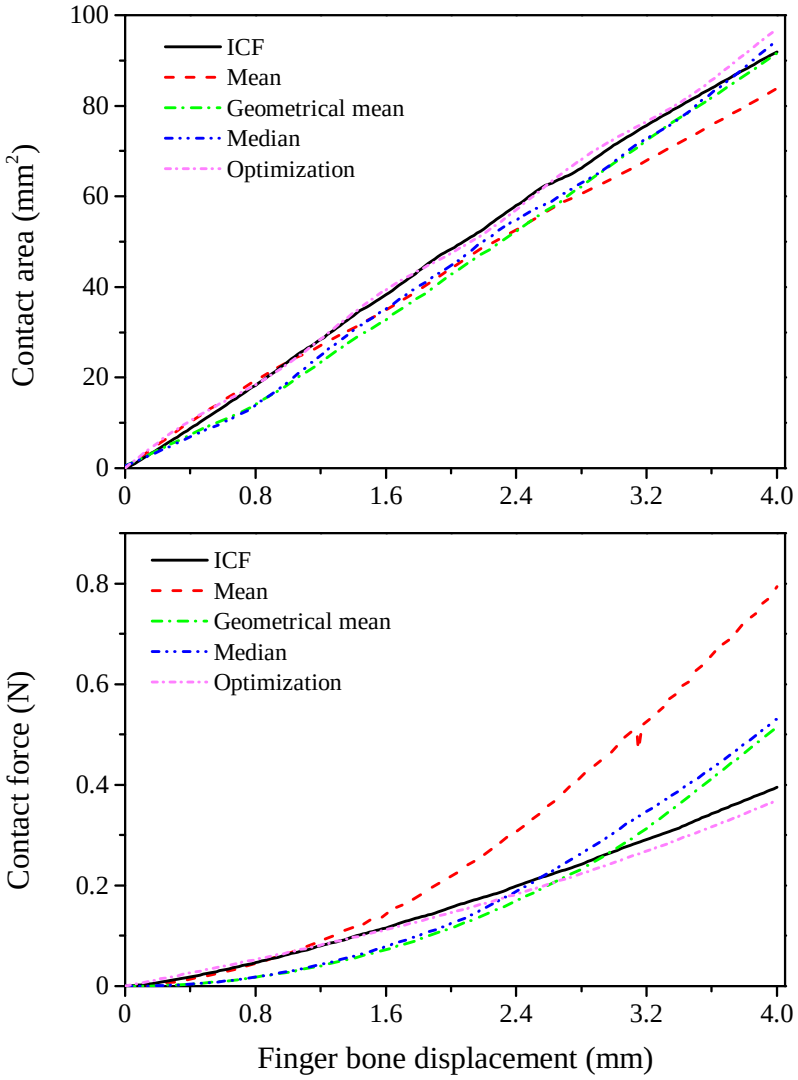

Figure 58: Contact area and reaction force of interaction between the finger pad with ICF and material with variable yield strength calculated by the FE model.

A test setup is built as shown in Fig. 59. A computer vision-based motion tracking system is employed to track the movement of the subject finger pad. Major components of the test setup are shown in Fig. 60. Two soft foams, ICF and A2, are employed for testing the proposed control algorithm. Control curves of reaction force versus ampere are achieved from FE simulation of the finger pad contact with the ICF and A2 material models, and magnetic FE model of the designed softness

display. In order to achieve these control curves, the yield strength (σ_y) is calculated as a function of reaction force (F_r) by optimization and the finger pad FE model:

$$\sigma_y = f_1(F_r) \tag{39}$$

Then the magnetic flux density ($|B|$) is calculated as a function of yield strength using the datasheet provided by the manufacturer of the MR fluid (see Fig. 53):

$$|B| = f_2(\sigma_y) \tag{40}$$

Then the magnetic FE model of the softness display is used to calculate the required Ampere (A) for achieving the desired value of the flux density. This relation expresses this current as a function of flux the density:

$$A = f_3(|B|) \tag{41}$$

Linear interpolation is applied to the discrete data of these functions in order to achieve similar data intervals. Then the relation between the reaction force (F_r) and the required Ampere (A) is calculated by replacing the independent variable of each function with same dependent variable of another function:

$$A = f_3(f_2(f_1(F_r))) \tag{42}$$

The resulting curves for ICF and A2 elastomeric foams are shown in Fig. 61 which shows the relation between the reaction force and the required Ampere for the electromagnet of the softness display. Curves are achieved for A2 and ICF elastomeric foams. These curves are used as a lookup table inside the controller software of the designed display. The controller software is designed in Matlab Simulink. The block diagram of the controller software is shown in Fig. 62.

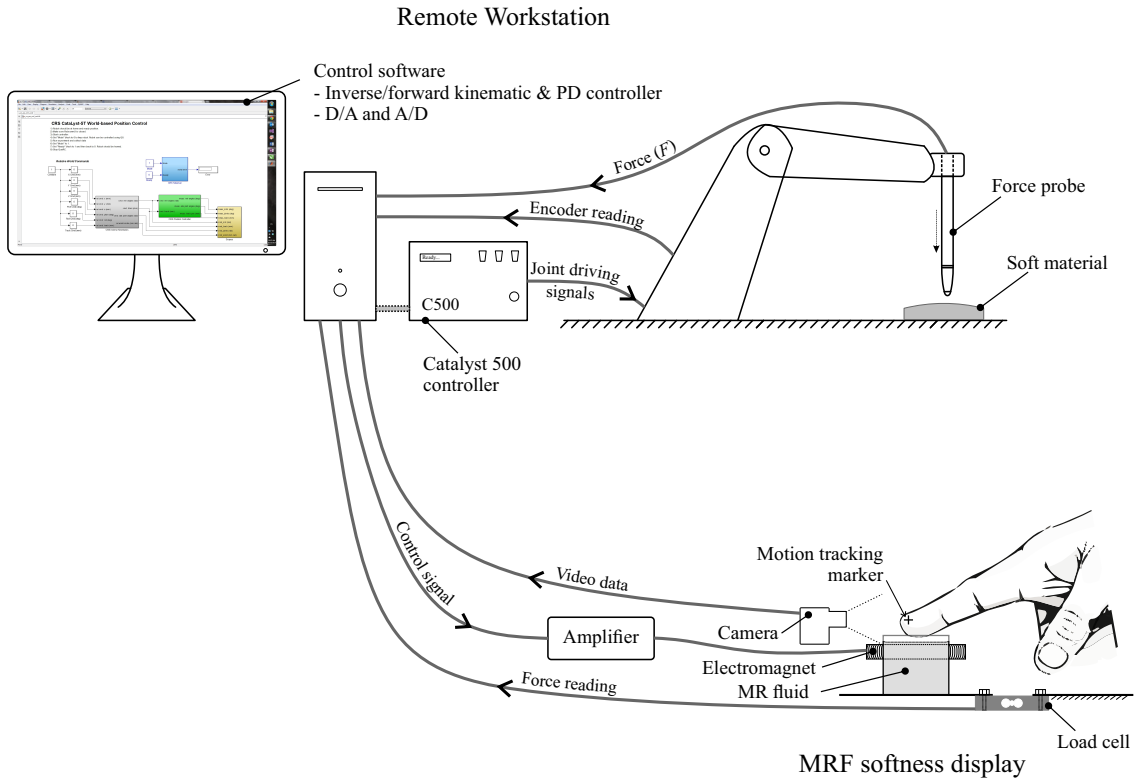

Figure 59: Schematic of the closed-loop system of the MRF based softness display.

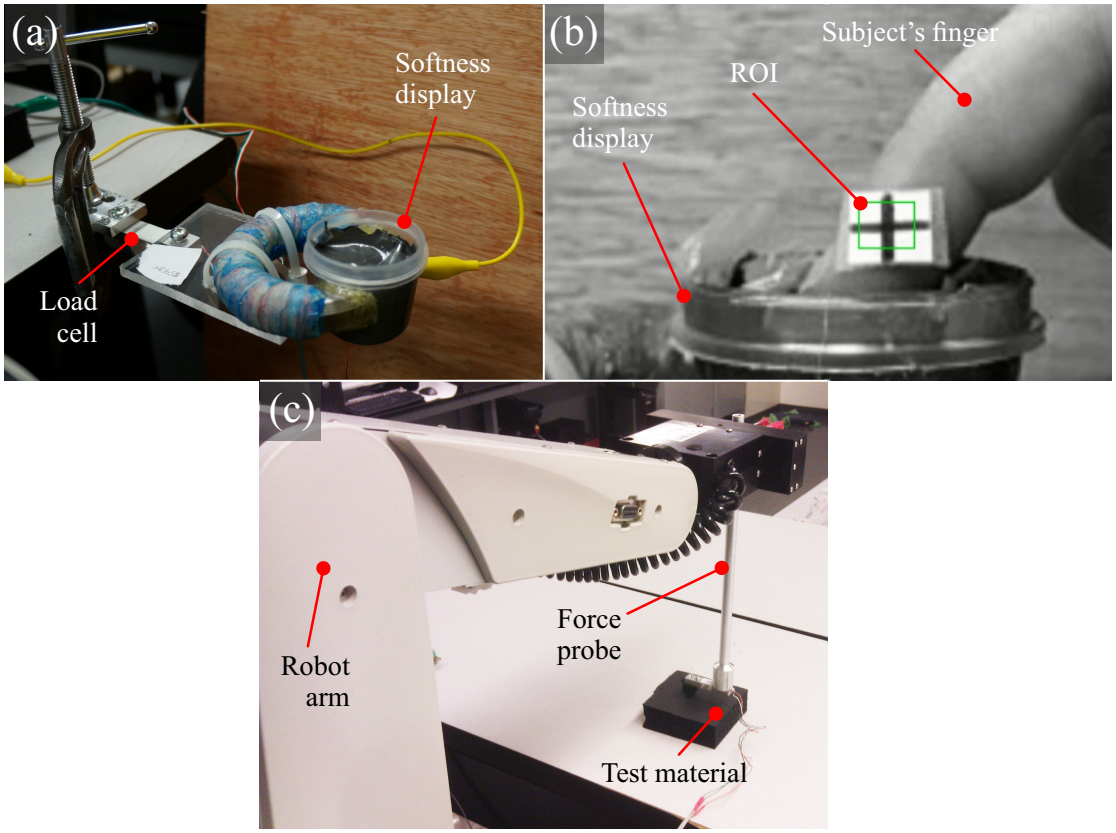

Figure 60: Components of the test setup. (a) Prototype of the display mounted for the palpation experiment. (b) A still frame extracted during real-time image processing for object detection and tracking in which the region of interest (ROI) is marked by a green rectangle. (c) Robot arm equipped with a force probe.

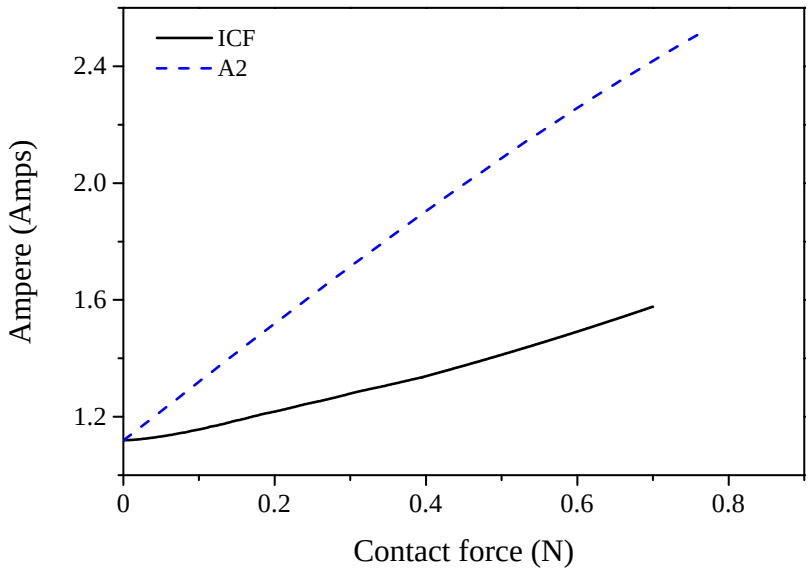

Figure 61: Reaction force and required Ampere for the electromagnet of the softness display.

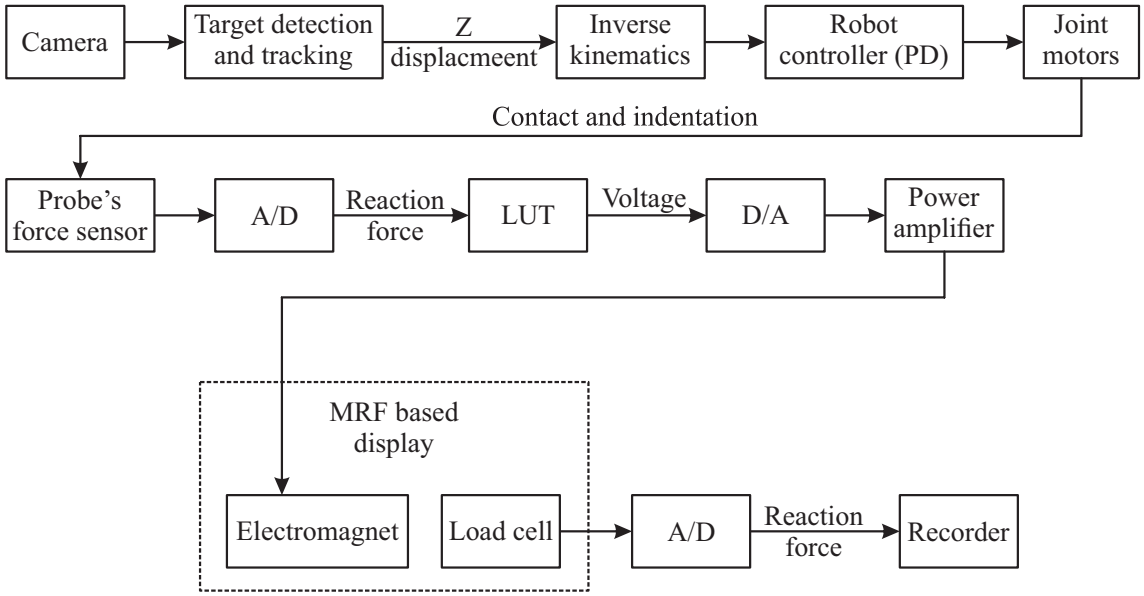

Figure 62: Block diagram of the softness display test experiment.

4.4 Results and Discussion

Two softness recreation tests are performed using the explained test setup and the proposed control algorithm. In these experiments deformation behavior of A2 and ICF elastomer foams are mimicked by the proposed display. First, graphs of the vertical displacement of force probe tip are obtained in order to evaluate the performance of the vision system. An example of these graphs is shown in Fig. 63. Control graphs of the two soft elastomer foams are used for evaluating the softness recreation of the proposed display in the test setup. The reaction forces recorded by the force probe, together with the load cell attached to the robot arm's end effector and the softness display, are shown in the graph displayed in Fig. 64. As can be seen from this graph, the reaction force peaks (recreated by the softness display) show that the loading phase is similar to the loading phase of the force probe in contact with the soft material thereby demonstrating conformity to the reaction forces of the contacts of the robot arm with the soft material and the human finger pad with the softness display. However, as previously explained, there is no unloading phase for the softness display.

Although the employed electromagnet was not strong enough for applications of recreating stiffer material behavior, the experiments using the soft elastomer foams show capability of the display and the proposed control method for recreating the mechanical behavior in the loading phase. The represented results in this work show

that the proposed control model and the display design are suitable for tactile applications such as displaying softness. Future work, such as recreation of softness for stiffer materials, will necessitate the use of stronger electromagnet and amplifier circuits.

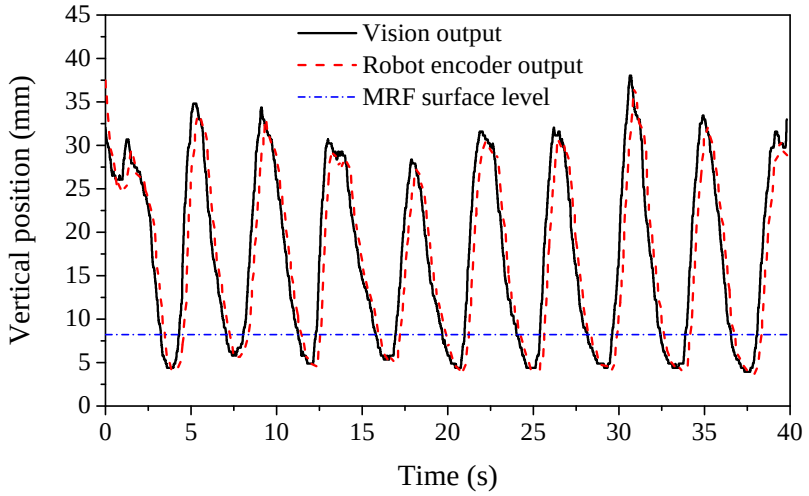

Figure 63: Outputs of the object tracking algorithm compared with output of the robot encoder. Surface level of the MRF display is shown by dotted blue line. Contact between the finger pad and the display happens when vertical position of the finger pad (vision output) falls below the MRF surface level in the loading phase.

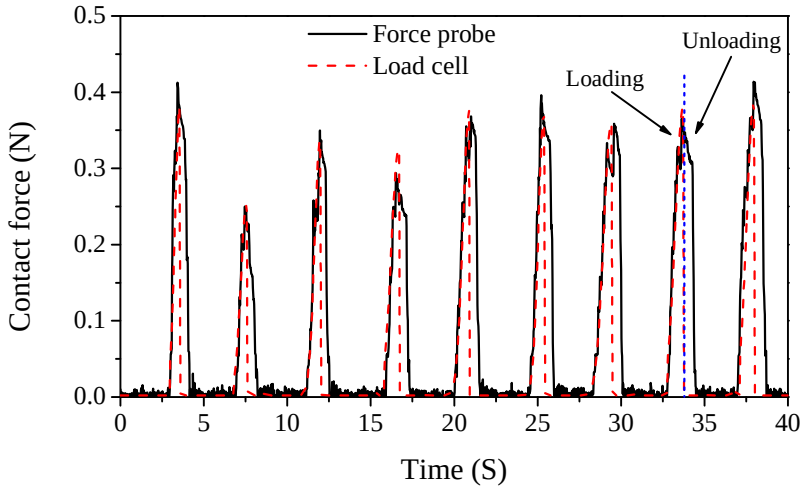

Figure 64: Comparison between the reaction forces recorded from the force probe at the robot arm end effector and the load cell attached to the softness display.

Chapter 5

Contact Modeling and Control of Linear Actuator Based Tactile Display

Most tactile displays that have been introduced which are driven by a servomotor, or other type of linear actuator, use the spring model to simulate the softness. From a simplistic point of view, most materials can be modeled as a spring which, for small strains, is good for characterizing the softness of the material. However, in large deformations, the spring model cannot determine the behavior of the material with any exactness. During the Minimally Invasive Surgery (MIS), a surgical endoscope can apply large forces on tissues which results in a considerable amount of strain on those tissues. Based on the above facts, a tactile display system was designed which takes the nonlinearity in force-displacement into account. This tactile display

comprises a linear actuator, a force sensor, and processing software. The system can reconstruct the softness of different materials based on the mechanical properties of those materials, and fingertip pulp deformation behavior.

In this work, the data of the mechanical properties of the materials were measured and recorded. The effect of fingertip pulp deformation was applied to the material model and used by the processing software for reproducing the same properties by the tactile display. By calculating the dimension of the contact area, over which the force is applied, these stress-strain data can be transformed to force-compression which is used by the processing software to actuate the display. The data are saved in lookup table in the processing software which gathers information from the applied force to the shaft of a linear actuator and the position of the shaft. In conjunction with this information, and using the lookup table, the response of the material to the applied force is extracted from the table and used as the input to a PID controller which prepares necessary commands to the linear actuator to move the shaft. Tuning of the PID controller and robust stability of the controlled system are explained. The experimental results showed that the developed tactile display can replicate the softness of materials very accurately.

5.1 Tactile display system design

Although a complete tactile display needs a number of actuators, this study focused on the methodology of gathering and interpreting material information by means

of a tactile display. The realization of a comprehensive tactile display is merely a matter of adding the number of sensors and actuators and miniaturization. Therefore, as mentioned above, the tactile display system comprises a linear actuator, a force sensor, and processing software. The linear actuator is used as a softness display and the force sensor to measure the applied force by the finger to the tip of the actuator shaft. The working principle of the system is to measure the force applied by the finger to the linear actuator shaft, calculate the displacement of the shaft in response to the applied force according to the mechanical properties of the simulated material, and move the shaft to the calculated position to produce the sensation of softness. Ideally the material properties will be measured in real-time. In this study, however, the mechanical properties of several materials, such as the stress strain relation for different objects, were measured off-line and stored in a material data base to be processed eventually. By measuring the applied force to the actuator, and having the contact area of fingertip and the cap, the applied stress can be calculated and the related strain found using the characteristic curve of the simulated object. The calculated strain was then converted to the displacement and used as the input to the PID controller. Having determined the desired position of the shaft and its actual position, the PID controller prepared the control commands for the actuator and fed them to the driver circuit. Fig. 65 shows the block diagram of the system.

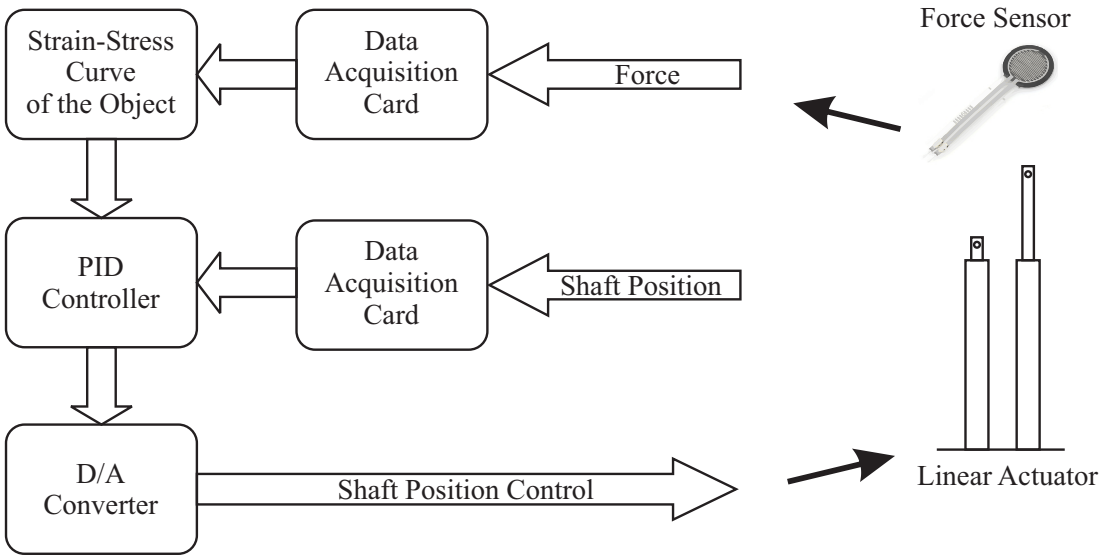

Figure 65: Block diagram of the tactile display design. [54, 118]

5.1.1 Linear Actuator

As explained in [54,118], the tactile display shown in Fig. 66, consists of a combination of a linear actuator, Plexiglas cap, force sensor, shaft position sensor and current-driver electronics. The stroke length of the actuator shaft is about 2 cm and can apply a maximum force of 30 N. The cap is glued to the tip of the shaft and a force sensor, placed on the cap, measures the force applied by the finger to the shaft. The linear actuator can measure the position to an accuracy of within 0.5 mm.

Figure 66: Elements of the tactile display. [54, 118]

5.1.2 Force Sensor

The Force Sensing Resistor (FSR) is supplied by the Interlink Electronics Company and is a polymer thick film (PTF) device whose resistance decreases in direct proportion to the increase in force applied to the active surface. Its force sensitivity is optimized for use in human touch control of electronic devices. To determine the force-conductance relation for the FSR experimentally, several different standard weights are placed on the active area of the FSR and its conductance measured. The results are shown in Table 7.

Table 7: Experimental results for determining force-conductance relation.

Force(gr)	Conductance($^1/\Omega$)
100	0.0733
200	0.1518
300	0.2151
400	0.2603
500	0.3589
600	0.4611
700	0.5314
800	0.6217
900	0.6774

The data plotted in Fig. 67 shows that the conductance in the FSR is almost linear in relation to the applied force.

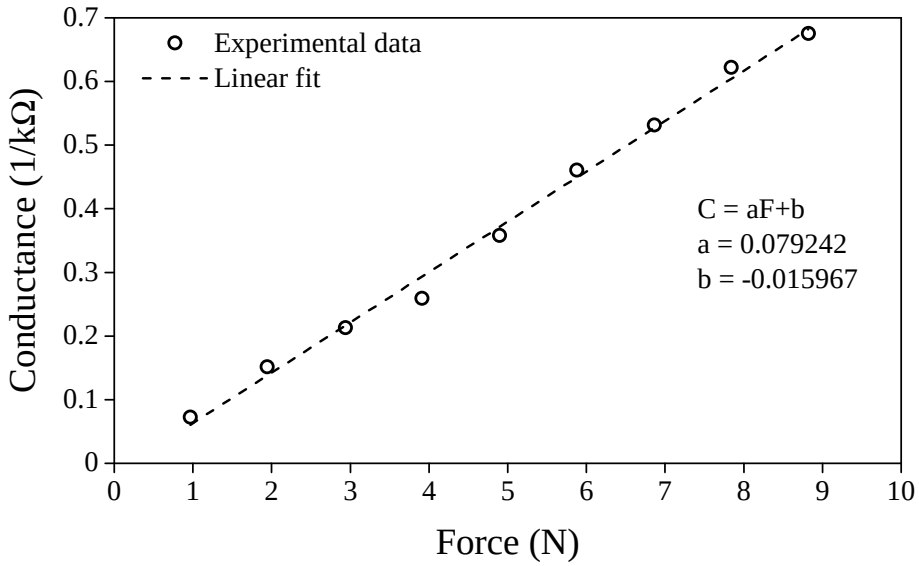

Figure 67: The Conductance of the FSR versus force. [54, 118]

A line drawn through points derived from the experimental data in Eq. 43 is used to relate the conductance c and force f:

$$c = af + b \tag{43}$$

where $a = 0.079$ and $b = -0.016$.

To measure the resistance (conductance) of the FSR, we used the electric circuit shown in Fig. 68 from which the conductance of the FSR can be calculated using Eq. 44.

$$V_r = \frac{R}{R+r}V^+ \Rightarrow C = \frac{1}{r} = \frac{1}{\left(\frac{V^+}{V_r} - 1\right)R} \tag{44}$$

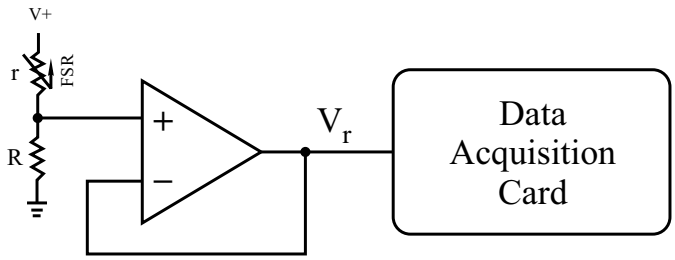

Figure 68: The electric circuit for measuring resistance r. [54, 118]

By combining Eqs. 43 and 44 we can find a relationship between the force F and voltages V_r and V^+ as shown in Eq. 45.

$$F = \frac{1}{\left(\frac{v^+}{Vr} - 1\right)Ra}\frac{b}{a} \tag{45}$$

where $a = 0.079$, $b = -0.016$, $R = 10\ \text{k}\Omega$, and $V^+ = 5\ \text{V}$.

Voltages V_r and V^+ were used by the data acquisition card and the force was calculated by the processing software using Eq. 45.

5.1.3 Shaft Position Sensor

A built-in linear potentiometer was used to find the position of the shaft. The relationship between the resistance of the potentiometer and the length of the shaft is plotted in Fig. 69.

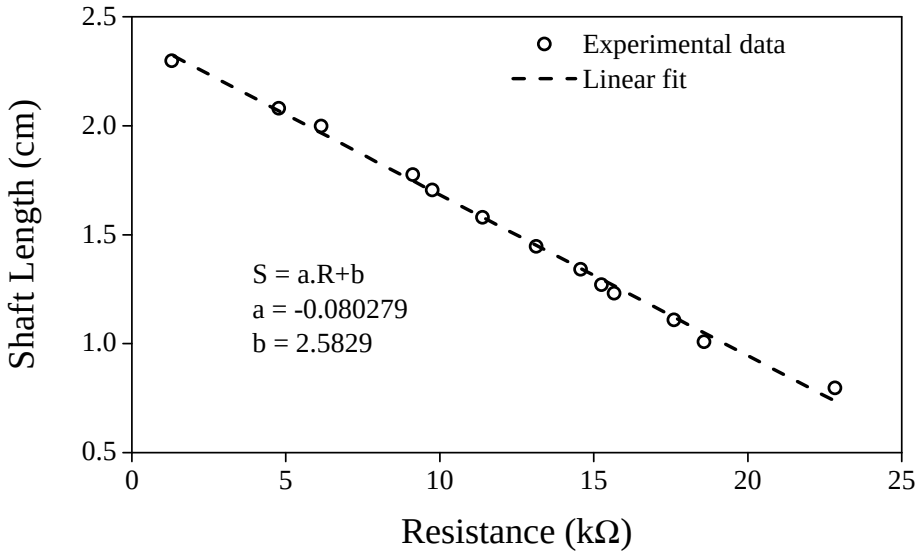

Figure 69: The relationship between shaft length and resistance. [54, 118]

Using the linear relation of the shaft length and resistance, the position of the shaft can easily be determined by measuring the resistance of the potentiometer. To measure the resistance, an electric circuit is used similar to that shown in Fig. 68 except that the FSR was replaced by a potentiometer. The relationship between the

shaft length (l) and the measured voltage (V_s) can be found using Eq. 46:

$$l = \frac{1}{\left(\frac{v^+}{Vs} - 1\right) Ra} \frac{b}{a} \tag{46}$$

where $a = -0.080279$, $b = 2.5829$, $R = 10$ kΩ, and $V^+ = 5$ V.

Therefore the applied force (F) and the displacement of the shaft (l) can be found by using relationship between Eqs. 45 and 46.

5.2 Stress-Strain Curves

For this research work, the mechanical properties of several materials were determined using mechanical ElectroForce® 3200 compression test instrument supplied by the BOSE Corporation. Fig. 70 shows the results of this test using four different materials.

Each of the four rows in Fig. 70 shows a different elastomeric material. The graph on the left shows the stress-strain curve and the graph to the right shows the force-displacement relationship for the same material. Since the dimensions of the test materials are known, the stress and strain can be calculated from the force and displacement curve. The material used in Fig. 70(a) is open cell polyether (A2) having a thickness of ¾ inch. In Fig. 70(b), the material is ½ inch thick closed cell ethylene vinyl acetate (EVA). In Fig. 70(c), the material used is one-inch thick PVC/NBR polymer (ICF400) and for Fig. 70(d), the material is ¾ inch thick closed cell sponge neoprene (B1) foam. An identical test is used in this investigation to simulate the same behavior for each of the four different elastomers using the linear actuator.

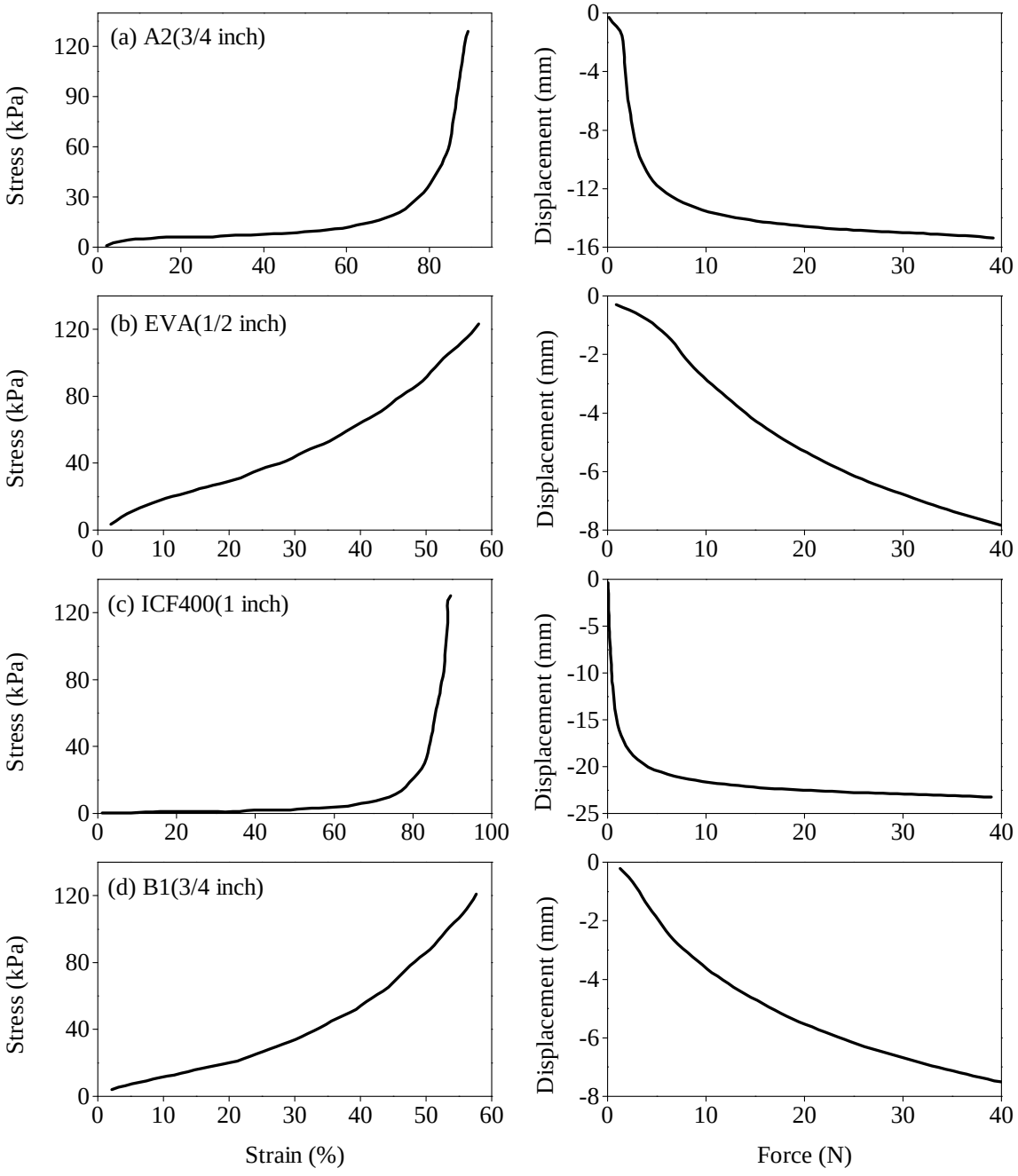

Figure 70: Mechanical compression test results.

5.3 Fingertip Pulp Deformation

Fingertip deformation has been investigated in several studies. Serina et al. [119] developed a structural model of human fingertip to predict force-displacement and force-contact area responses of the fingertip during contact with a flat rigid surface. Pawluk and Howe [120] used quasi-linear viscoelastic model of tissue [121] to explain the loading and relaxing phases of the human fingertip dynamic response. In this research, fingertip pulp deformation has been taken into account using a Hertz elastic contact model [122] according to which a is the radius of the contact area between two spheres as defined in Eq. 47:

$$a = \left(\frac{3FR}{4E^*}\right)^{\frac{1}{3}} \tag{47}$$

where, F is the applied force, R is the effective radius of two spheres (spheres with radiuses R_1 and R_2), defined as:

$$\frac{1}{R} = \frac{1}{R_1} + \frac{1}{R_2} \tag{48}$$

and E^*, the effective elastic modulus, is defined as:

$$\frac{1}{E^*} = \frac{1-\nu_1^2}{E_1} + \frac{1-\nu_2^2}{E_2} \tag{49}$$

where E_i and ν_i denote the Young's modulus and Poisson's ratio associated to each body.

To consider the difference between fingertip/actuator contact and fingertip/material contact, the actuator shaft and material contact surfaces are considered as being flat and the Young's modulus of the shaft, compared to finger pulp, is considered infinite. This is because the mean value for the fingertip Young's modulus, in the medial-lateral and proximal-distal directions, is in the kilo pascal (KPa) range [23] which is negligible when compared to Plexiglas which is in the giga pascal (GPa) range.

Considering one of the bodies as being a flat elastic surface, and assigning R_2 value as infinite, Eq. 47 can be rewritten to produce Eq. 50 as follows:

$$a = \left(\frac{3FR_1}{4E^*}\right)^{\frac{1}{3}} \tag{50}$$

therefore, depth of indentation, $d = \frac{a^2}{R}$, can be calculated as shown in Eq. 51:

$$d = \left(\frac{3F}{4E^*R^{\frac{1}{2}}}\right)^{\frac{2}{3}} \tag{51}$$

From Eq. 51, the difference between the two fingertip deformation modes originating from the difference in E^* can be calculated as shown in Eq. 52:

$$\begin{aligned} \frac{1}{E_1^*} &= \frac{1-\nu_1^2}{E_1} \\ \frac{1}{E_2^*} &= \frac{1-\nu_1^2}{E_1} + \frac{1-\nu_1^2}{E_2} \end{aligned} \tag{52}$$

The elastic moduli of elastomers are obtained from the linear portion of the stress-strain curves. Considering the fingertip as being a sphere with radius $R = 5$ mm, $\nu = 0.5$ [123] and $E = 126.2$ KPa, the modified force displacement graphs are represented in Fig 71. Based on these assumptions, fingertip deformations are valid up to 5 mm using a force 5.63 N. Beyond this value, the controller switches to the original which is measured by elastomer compression. As shown in Fig. 72, fingertip pulp deformation in contact with an actuator is different from one that is in contact with simulated material. Since a hard contact occurs between the actuator shaft and finger pulp, the contact interface and contact area between finger pulp and actuator shaft would deviate from ideal values in contact between finger pulp and soft materials.

Fig. 71 shows the modified force-displacement curves based on fingertip deformation correction for the four different elastomers.

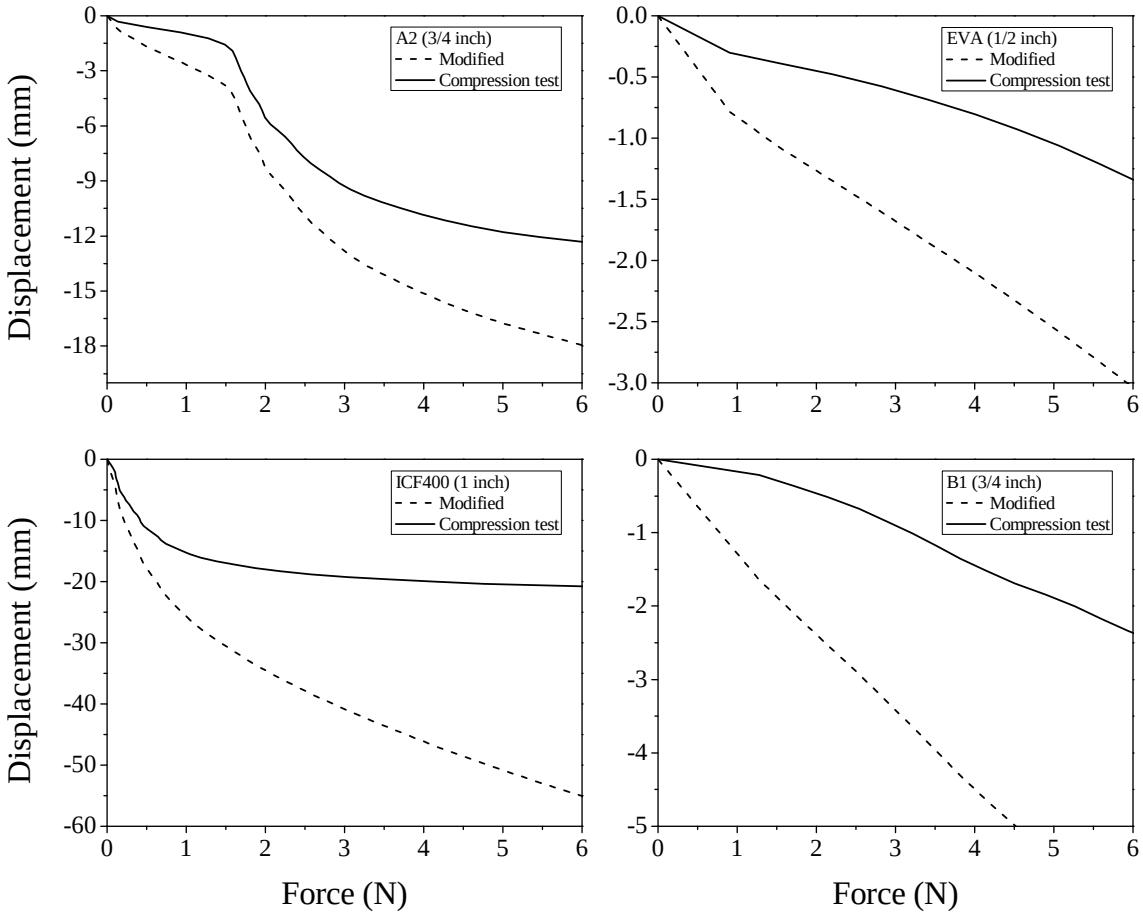

Figure 71: Modified force-displacement curves.

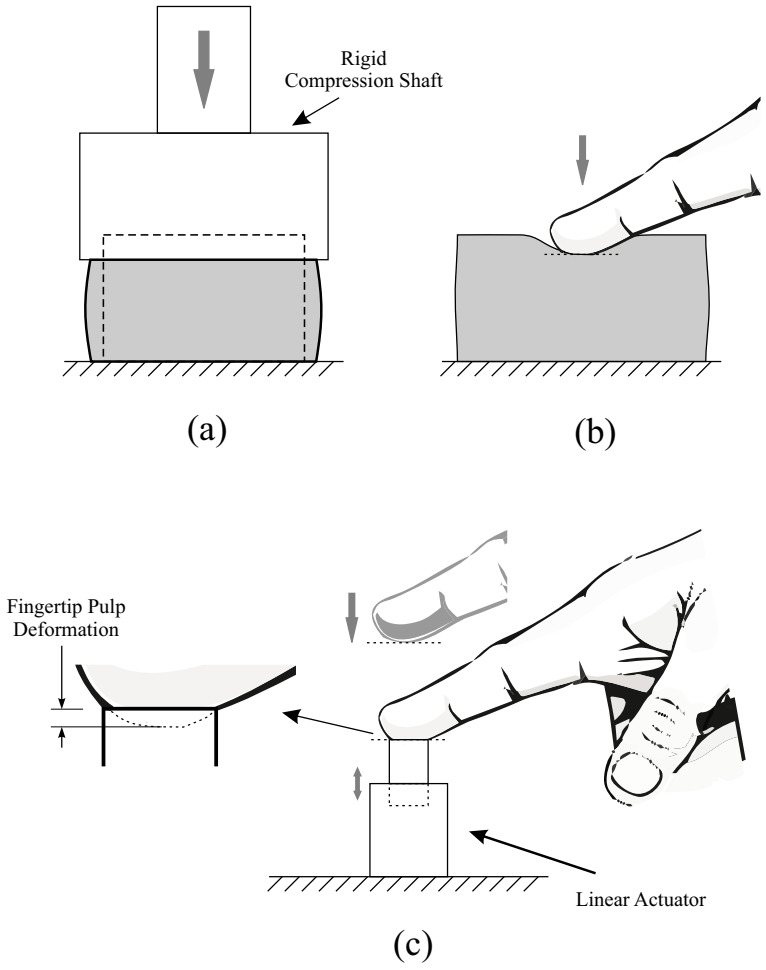

Figure 72: Compression test and fingertip contact. (a) shows a compression test to obtain stress-strain behavior of the material. (b) shows contact of fingertip pulp with an elastomeric material. (c) illustrates fingertip pulp contacting an actuator.

As can be seen, the modified curve shows more displacement compared to the compression test. The difference in displacement can be described as extra finger pulp deformation in hard contact of finger and actuator shaft compared to finger and soft material. Since A2 displays relatively harder behavior than that of ICF400, the difference between compression and the modified curve for A2 is smaller.

5.4 PID Controller

The measured force from the force sensor was registered by the data acquisition card, DAC, and read by the processing software. The position of the shaft of the actuator was also measured and transmitted to the processing software through the DAC. The mechanical properties of the object to be simulated had already been determined and saved in the computer. These data contained the strain-stress relation for different objects. With a known force applied to the linear actuator by the fingertip, and having the dimensions of the cap over which the force was applied, the stress was calculated and the desired strain was found by using the characteristic curve of the simulated object. The desired strain was then converted to the displacement and used as the input to the PID controller.

To simulate the behavior of each elastomer, the linear actuator was required to follow their force-compression relationship and was hence required to re-construct the tangent modulus, or the slope of force-displacement, at each moment. In order to accomplish this, a negative feedback closed-loop control system with PID controller was used. The PID controller monitors the position of the shaft, compares this position with the desired position of the shaft and, based on the difference which is called the following error, prepares proper commands to the actuator to move the shaft to the desired position.

To be able to design a controller for the system, a model of the linear actuator was derived [54]. Fig. 73 shows the block diagram of the system.

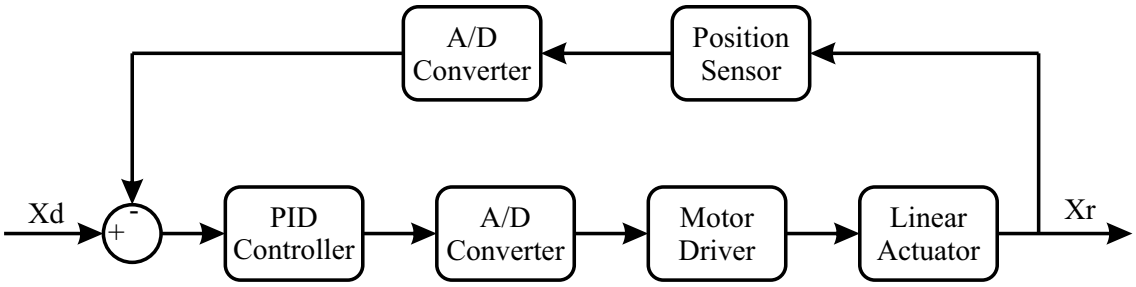

Figure 73: Block diagram of a linear actuator system.

5.5 PID Controller Tuning

For the special system explained in [54] research work, the position of the shaft, and the applied force by the finger to the shaft, follow the desired force-position curve as closely as possible. To minimize the tracking error as a cost function, the optimum controller design method is used to find optimum PID controller parameters. The error is defined as the difference between step input and output. The cost function to be minimized (J) is the sum of errors in each step from 0 to 100 seconds as shown in Eq. 53. The PID controller parameters (K_P,K_I,K_D) as well as filter coefficient (K_N) are chosen as the design variables. In addition, three constraints are introduced for the optimization problem to limit the actuation signal (u), system overshoot and system undershoot (OS and US). The closed-loop system including the actuator and the PID controller is shown in Fig. 74.

$$J = \int_0^{100} |y(t) - u(t)|\, dt \tag{53}$$

Subject to:

$$|u(t)| < u_{max}$$

$$[OS, US] < |y(t) - r(t)|_{max}$$

In discrete cases, Eq. 53 can be written as Eq. 54:

$$J\left(K_P, K_I, K_D, K_N\right) = \sum_{k=1}^{P} |y(k) - r(k)|_{max} \tag{54}$$

where

$$P = \frac{100}{T_S}.$$

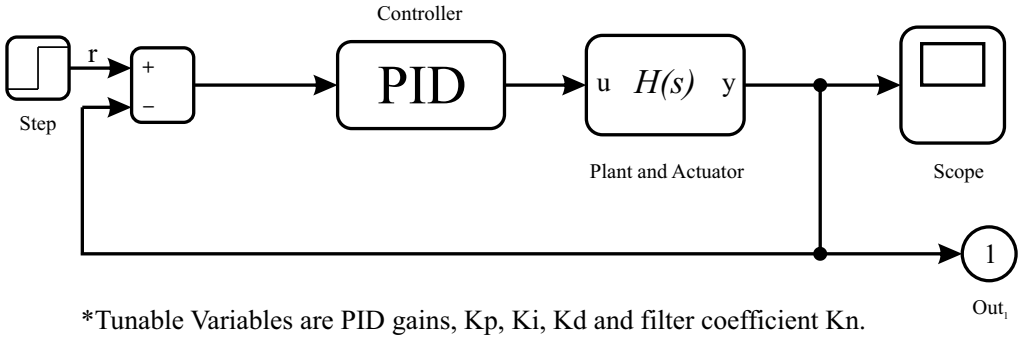

Figure 74: The closed-loop system for PID design.

P is the total number of samples in 100 seconds, T_S is the sampling period and $(y(k) - r(k))$ determines the difference between system input and output. u_{max} is

limit for the actuation signal, and $|y(k) - r(k)|_{max}$ is maximum amount of the difference between system input and output which limits the overshoot and undershoot. Having the number of samples (P) and sampling period (T_S), the objective of the optimization problem is defined as finding PID controller parameters (K_P, K_I, K_D, K_N) for which $J(K)$ becomes locally minimized subject to the constraints on actuation signal as well as overshoot and undershoot. The constrained nonlinear optimization method is performed using interior-point algorithm with the given tolerance in order of 0.001 to minimize (J). After twenty one iterations, the optimization process results in optimum proportional, integral and derivative (K_P, K_I, K_D) gains and filter coefficient (K_N) as $K_P = 3.6610, K_I = 14.1596, K_D = 0.1787, K_N = 7.4936$. Input signal and overshoot/undershoot constraints are set as $u_{max} = 5.0$ V and $|y(k) - r(k)|_{max} = 0.05$. The closed-loop transfer function of the system $\left(G(s) = PID(s) \times \frac{H(s)}{(1+PID(s)*H(s)}\right)$ is calculated as Eq. 55 and presented in Fig. 75, and the response of the tuned system to a step signal is presented in Fig. 76. The bandwidth of the closed-loop system is calculated as 4.0463 Hz.

$$G(s) = \frac{430s^6+1.686\times10^4s^5+1.95\times10^5s^4+9.091\times10^5s^3+1.6\times10^6s^2}{s^8+61.79s^7+1735s^6+2.77\times10^4s^5+2.258\times10^5s^4+9.091\times10^5s^3+1.6\times10^6s^2} \quad (55)$$

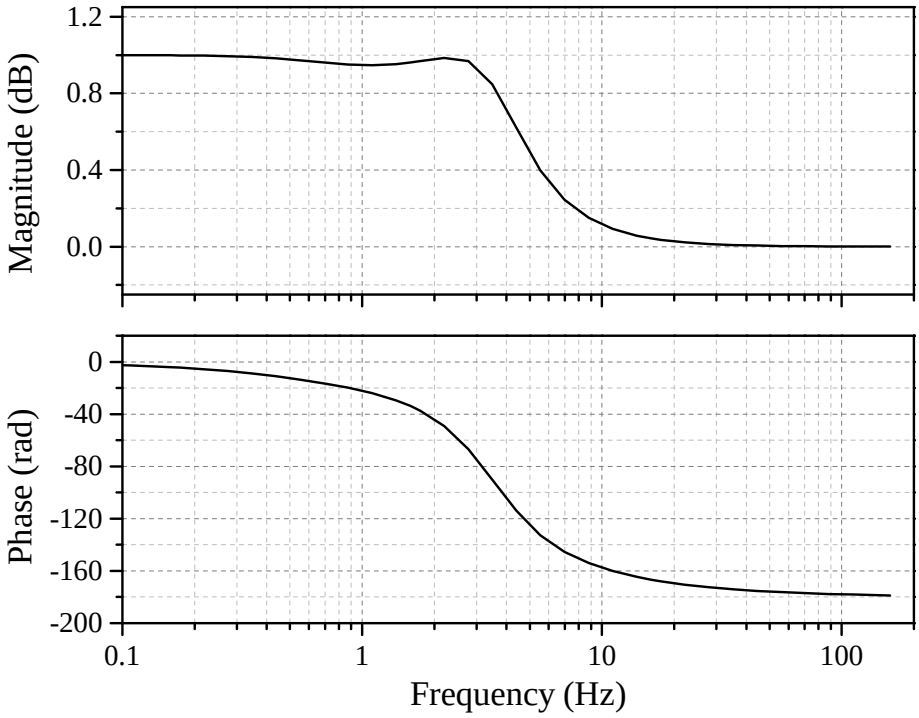

Figure 75: Bode plot of frequency response of the closed-loop system.

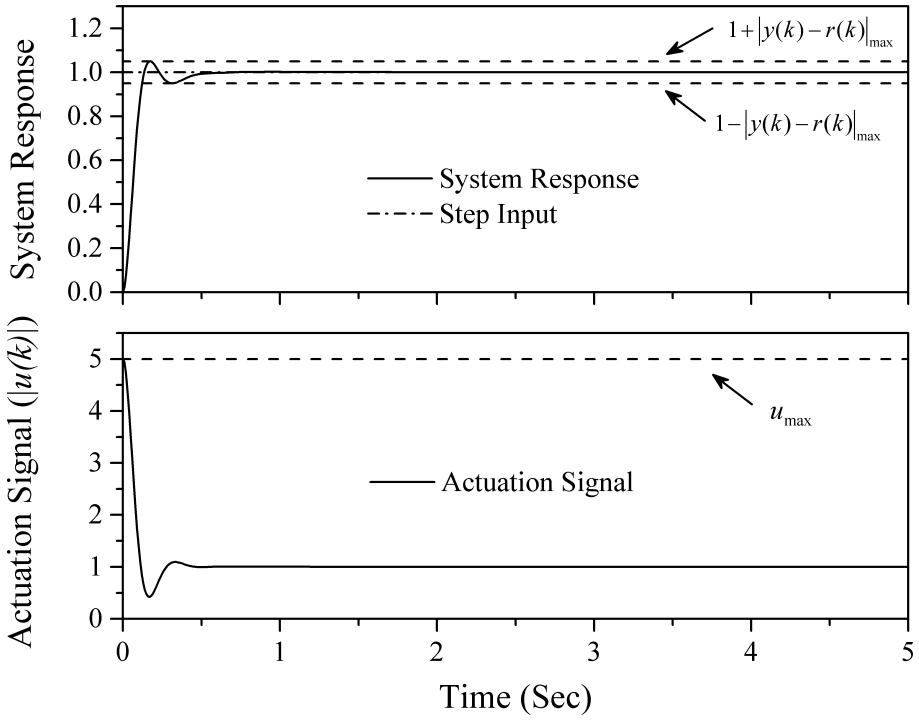

Figure 76: Response of the closed-loop system to a step input.

Fig. 76 shows response of the system to a step signal as well as the behavior of the actuation signal (u). The applied constraints for tuning the PID controller (constraints on input signal and overshoot/undershoot) are illustrated in this figure as dashed lines. In Figs. 76 and 75, it is noticed that the closed-loop system with PID controller tuned by the constrained optimization method has the limited bandwidth and owns satisfactory performance measures which can fulfill the tactile softness display task. Matlab code of the PID controller tuning is presented in Appendix E.

5.6 Robust Stability of the System

Stability analysis is performed on the system. In order to verify stability of the system, Nyquist criterion is employed on the system with 10% uncertainty on each of the system parameters. The Nyquist plot is shown in Fig. 77. As it can be seen, the point $(-1, 0)$ is not encircled by the plot.

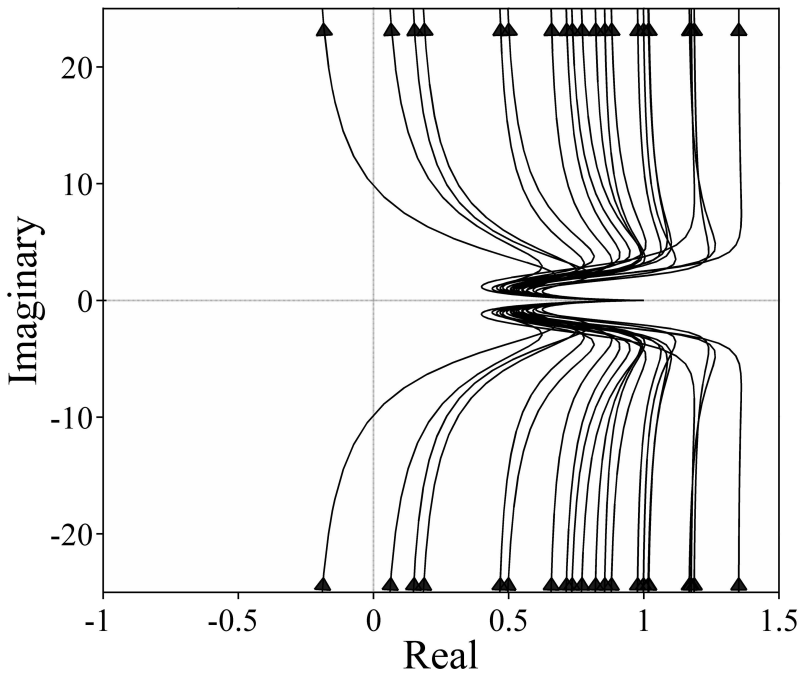

Figure 77: Nyquist plot of the frequency response of softness display system (plant and PID controller) with 10% uncertainty for system parameters.

Characteristic equation of the system and its complex roots are presented in Eq. 56. Roots of this equation are calculated with 10% uncertainty on equation parameters. Histogram of real parts of roots are shown in Fig. 78. It can be seen that real parts of the roots are distributed at -4.8 ± 2.5 and -11.6 ± 2.8 which is an

indication of robust stability for the system.

$$1 + PID(s).H(s) = 1 + \left(\frac{5.0001s^2+41.5936s+106.1063}{s^2+7.4936s}\right)\left(\frac{86}{s^2+23.4s+86}\right)$$

$$s_1 = -11.6143 - 18.9732i$$

$$s_2 = -11.6143 + 18.9732i \tag{56}$$

$$s_3 = -3.83248 - 1.93688i$$

$$s_4 = -3.83248 + 1.93688i$$

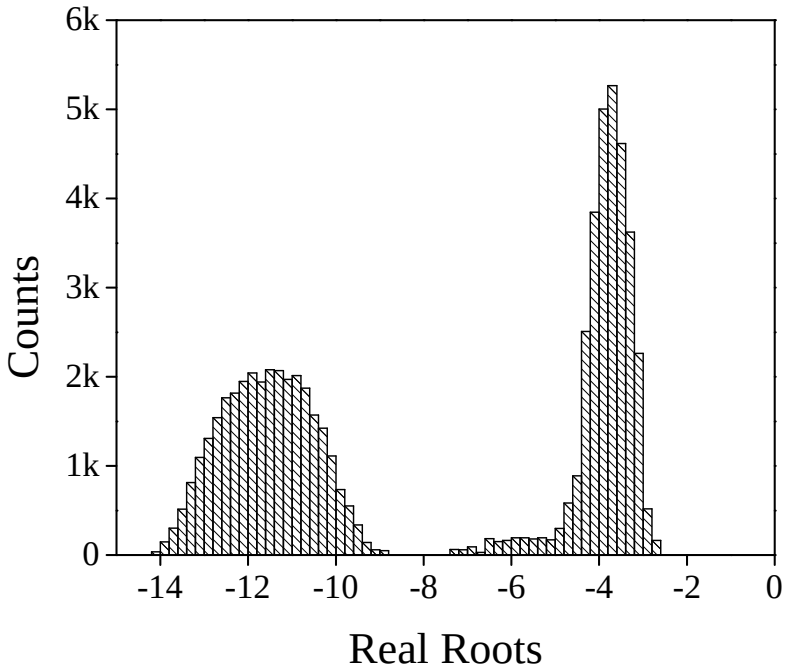

Figure 78: Histogram of real part of roots for the system characteristic equation (Eq. 56) with 10% uncertainty on equation parameters.

5.7 Simulation Results

The processing software, which is written for the Simulink environment, receives the feedback signals from the Force Sensing Resistor (FSR) and linear potentiometer as shown in Fig. 79. The force (F) and shaft position (X_r) are then calculated in separate modules as explained in [54]. The calculated force was then used to find the strain for the simulated material which is saved in a lookup table (LUT).

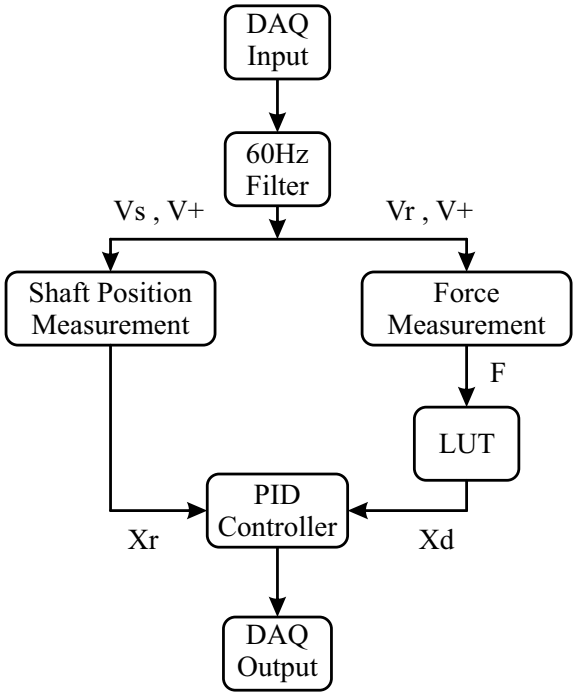

Figure 79: Flowchart of the processing software.

Having the dimensions of the material to be simulated, the stress was converted to compression (X_d). The shaft position and desired compression (X_r and X_d) were then fed to the PID controller. The output of the controller was finally used as the input to the linear actuator.

Fig. 80 shows the parameters which are plotted in the system-design platform

and development environment of the Simulink. The force, output, shaft displacement (measured and desired) and displacement error are plotted in real time. Comparing the measured and desired displacement shows that the error is proportional to the rate of change in displacement. This error exist in system due to limited displacement rate of the actuator.

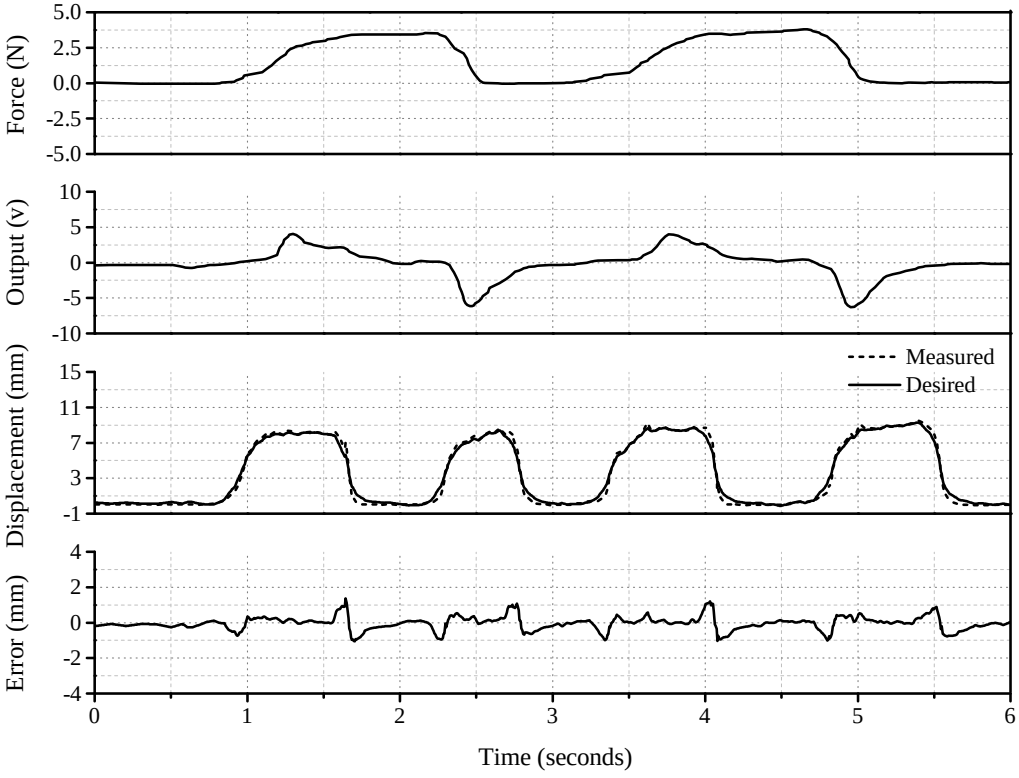

Figure 80: Measured and calculated signals plotted in realtime.

5.8 Experiments and Results

A number of experiments were conducted including stress-strain, position-force and softness display. Results of these experiments are presented as follow.

Stress-strain results:

Five different materials were selected to be simulated by the actuator. These included a hard material (Plexiglas), elastomers A2 (¾ inch thick), A2-FR (¾ inch), ICF400 (1 inch), and B1 (¾ inch). The strain-stress relations for these materials are shown in Fig. 81.

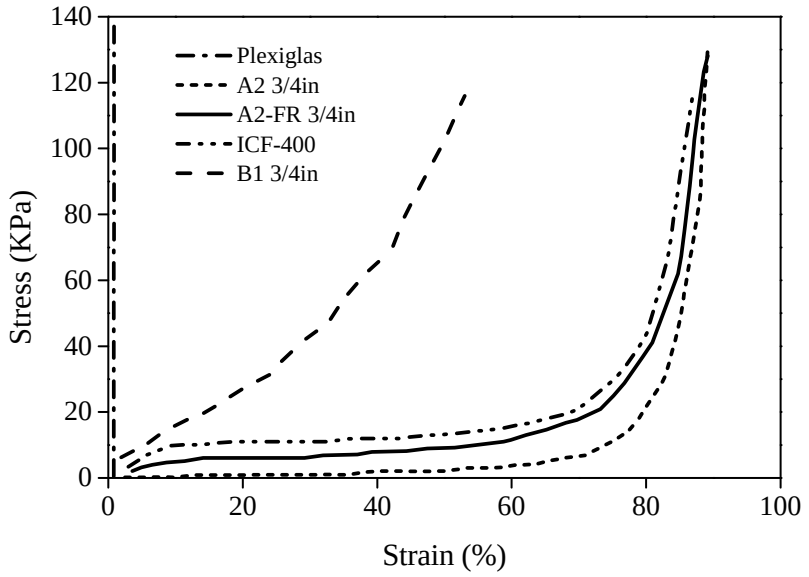

Figure 81: The stress-strain curves for different materials.

To assess the performance of the proposed tactile display, the force-position relation for each simulated material was saved, plotted and compared to the force-position relation of the material. Each curve can be divided into two separate phases: loading and unloading. The loading phase starts when the finger makes contact with the shaft and applies force. As soon as the force is removed, the unloading phase starts. In this phase the material returns to its initial form although the speed with which it does so depends upon its elasticity since the softer the material, the slower the return

speed. Fig. 82 shows both phases for elastomer A2 (¾ inches).

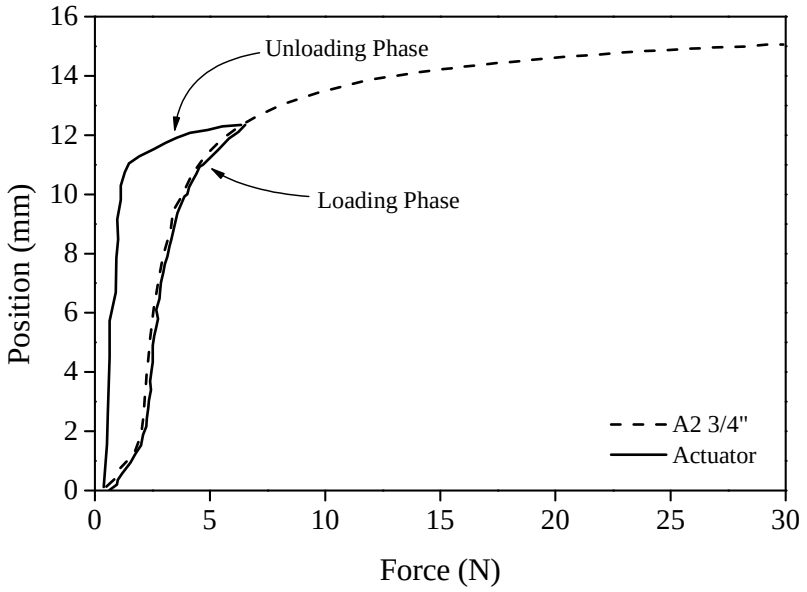

Figure 82: The force-position relation for A2 (¾ inch) elastomer.

Fig. 82 shows that during the loading phase, a small error exists between the simulated curve and the real curve (average position and force error of 16% and 8.7%, respectively). By selecting the optimum controller, this error is minimized but is slightly larger in the unloading phase although it does not, however, noticeably affect the softness perception. This is because the unloading phase, both for the elastomer and linear actuator itself, starts when the finger separates from the surface of the object so, therefore, the speed of unloading does not affect the perception of softness.

Position-force results:

Figs. 83, 84 and 85 represent the loading and unloading phases for three other tested elastomers EVA ½ inch, ICF400 1 inch, and B1 ¾ inch.

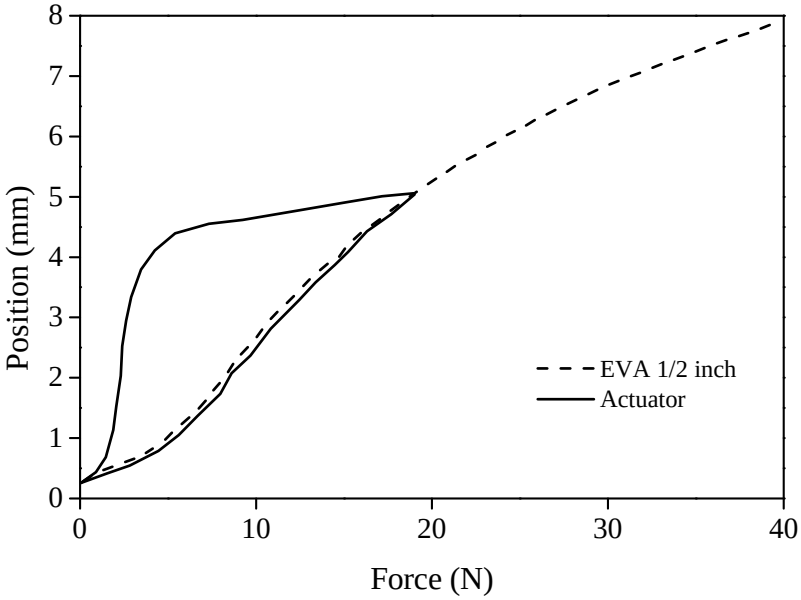

Figure 83: The position-force curve of EVA elastomer and its simulated equivalent.

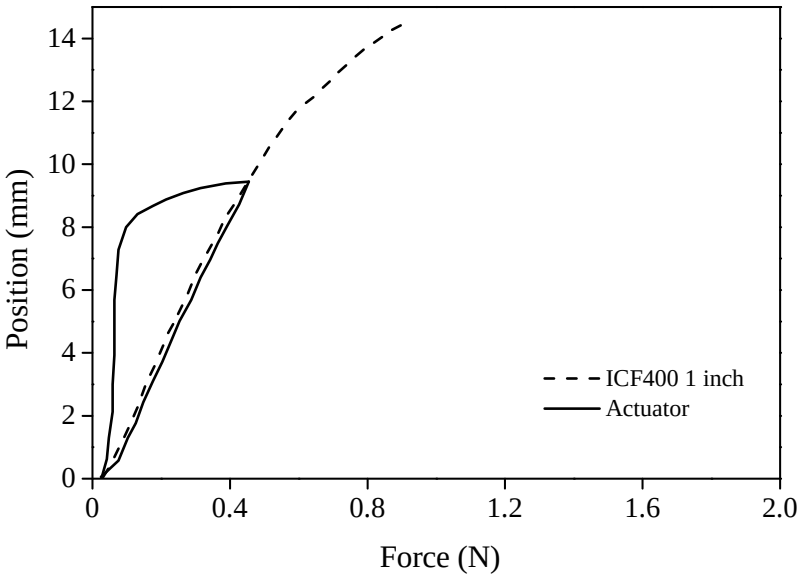

Figure 84: The position-force curve of ICF400 elastomer and its simulated equivalent.

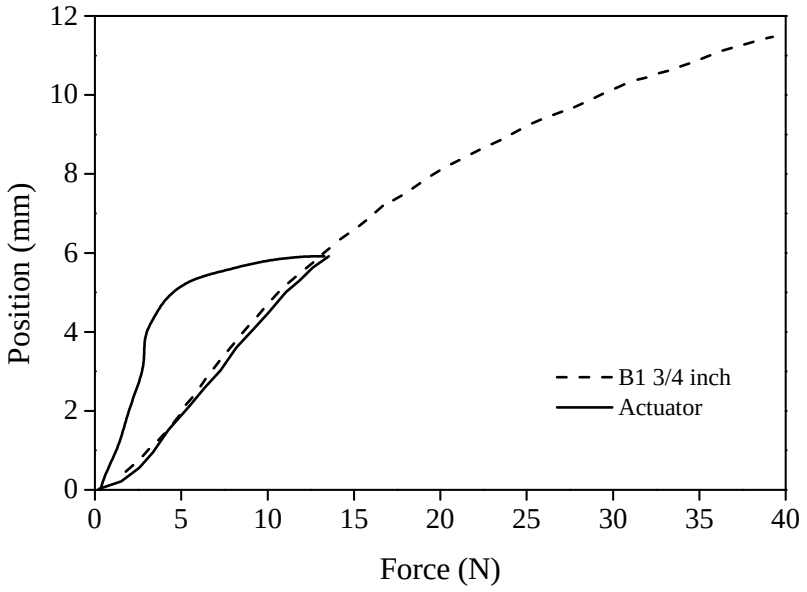

Figure 85: The position-force curve of B1 elastomer and its simulated equivalent.

The rate of applying force is also important for the sense of softness. As depicted in Fig. 86, the error is negligible when the force is applied slowly. However, when the force is applied suddenly, the error becomes larger. Fig. 86 shows the actual and desired force-position curves for two different speeds. In the first instance, force is applied slowly whereas in the second case it is applied quickly. From this, it can be seen that error in the first case is much less than in the second case. When the finger touches an object for softness recognition, it usually applies the force slowly so the error would not distort user perception.

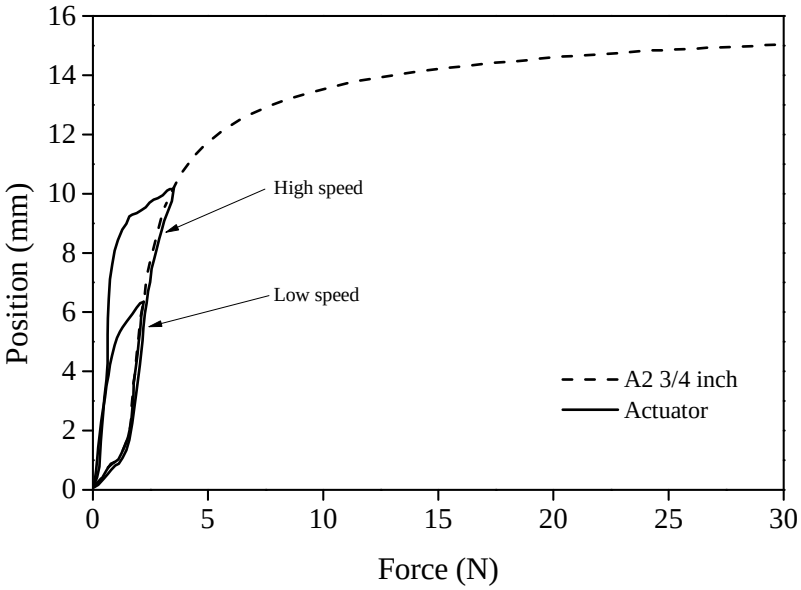

Figure 86: The effect of force rate and error.

Softness display results

To evaluate the efficiency of the tactile display, another experiment was conducted in which subjects touched four elastomer materials and then the linear actuator with their finger. They then attempted to relate the real elastomers with the softness at the tactile display. Each subject repeated this for each of the four simulated materials as illustrated in Fig. 87.

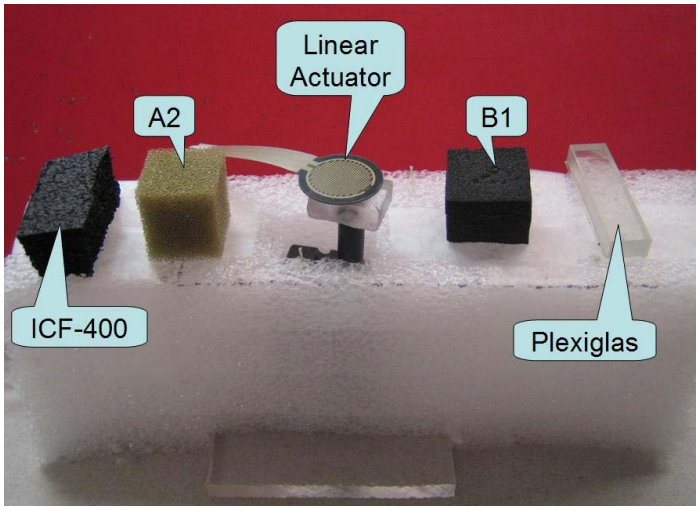

Figure 87: Setup of the finger touching experiment.

To remove the effect of visual feedback, the setup was covered so that the subjects were not able to see the different materials. In the first experiment, four materials were simulated by the tactile display, namely ICF-400, A2, B1, and Plexiglas. The subjects touched each material and finally decided which one of the objects had similar softness with the display. A total of twenty-five subjects participated in the experiment all of whom successfully distinguished between the simulated elastomers as shown in Table 8.

Table 8: Results of the first human subject test.

Material	Recognized	Not recognized
ICF-400	25	0
A2-400	25	0
B1-400	25	0
Plexiglas-400	25	0

In the second experiment, two materials with close mechanical properties (A2-FR and A2) were simulated by the tactile display. This time, the results of the simulation

showed some discrepancies in recognition as shown in Table 9.

Table 9: Results of the second human subject test.

Material	Recognized	Not recognized
A2-FR ¾ inch	17	8
A2 ¾ inch	14	11

The reason for the disparity in this test was because the subjects were required to distinguish between two materials that possessed very similar mechanical properties, as shown in Fig. 88 and without visual feedback.

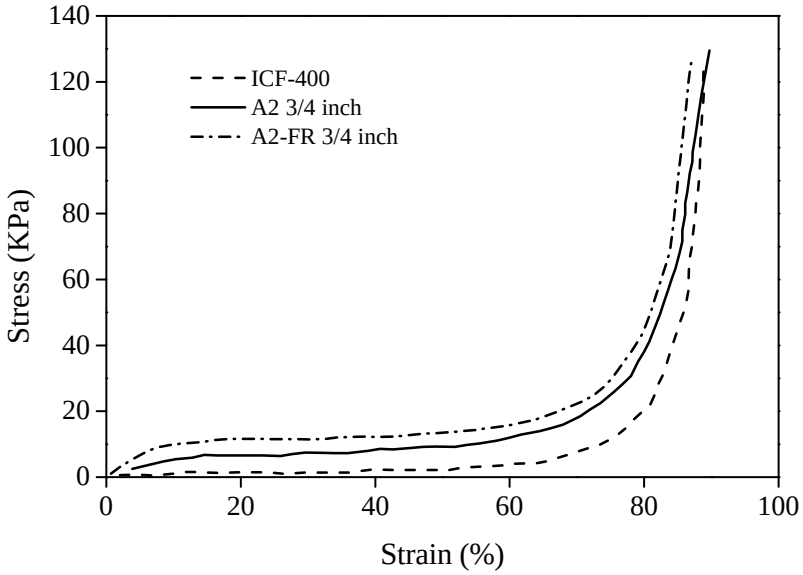

Figure 88: The material properties of the elastomers for the second experiment.

5.9 Conclusion

In this chapter, a system for displaying the softness of different materials was proposed and tested. The main components consisted of a linear actuator, a force sensor, and processing software for each of which a detailed description was provided. The

mechanical properties of various materials were characterized by conducting mechanical compression tests. These data were used by the processing software to actuate the display. A Proportional-Integral-Derivative (PID) controller was designed and optimized to control the shaft of the actuator to produce the same sensation of softness measured by the force sensor. Different materials were simulated by the tactile display and compared to the real objects. Experiments were conducted on the tactile display using human subjects and the results were recorded and presented. The results showed that the developed tactile display can replicate the softness of materials very closely and has great potential for identifying and categorizing objects by touch. In summation, it has proved to be a feasible technique with great potential use in robotic surgery, training facilities, virtual reality and minimally invasive surgery (MIS).

Chapter 6

Conclusion and Future Work

6.1 Conclusions

In this thesis, a novel inverse model program of estimating hyperelastic and hyper-viscoelastic material parameters has been developed based on the FE model and experiment of indentation using spherical indenters. MultiStart global optimization with single and multi-objective function methods, based on the Nelder-Mead simplex algorithm, have been employed for solving these inverse problems. Parameters of a suitable hyperelastic model have been identified for two different closed cell foams, namely EVA and B1. The validity of assuming frictionless contact between the indenter and foams during these indentation tests, as well as zero Poisson's ratio for closed cell foams, have been demonstrated using the same inverse model problem. The effect of indentation depth and indenter size were also investigated in estimated parameters and a numerical relationship was observed and reported in results. The

flexibility of this inverse method makes it suitable for general identification processes where direct measurements are not easily applicable. Applicability of this method is demonstrated on problem of hyper-viscoelastic material parameters identification for bovine liver tissue. It has, however, been shown that the accuracy of parameter identification using inverse indentation modeling is sensitive to both indentation depth and indenter size. It has also been shown that, by increasing the indentation depth, the difference between identified parameters using different indenter sizes decreases correspondingly.

Two methods of real time parameter identification were proposed for nonlinear soft materials. The proposed methods were based on variance calculation and parameter estimation using the Kalman filter algorithm. Both the methods were based on inverse FE modeling of spherical indentation test. The FE model of indentation was pre-evaluated in feasible range of material parameters and used as a reference data source for both the methods. Results are illustrated and compared in terms of precision and computing time. It was found that the variance calculation method required much less computation time compared to the Kalman filter method, which makes it suitable for real time identification procedures at high indentation rates. Although the Kalman filter method showed less scattering in identified parameters, it was prone to failure and, in some cases, was unable to achieve good convergence characteristics in contrast to the variance method. The proposed bounding methods for the Kalman filter estimation were implemented and their results compared. It was found that the Nearest Neighbor extrapolation method yields better results in

certain estimation processes such as if the estimate is selected on the state space boundary. However, during the normal identification processes, the Projection and Penalty methods yielded better results compared to the Nearest Neighbor method. The performance of both algorithms were assessed in material parameter identification and was found to yield a performance success rate of greater than 90% based on experiments in which random indentations (150 indentations per experiment) and three different indentation rates were employed. It was also found that increasing the indentation rate leads to more accurate and repeatable results, which perhaps is due to the reduced time dependent behavior of the studied materials. Identification results, from both the variance and Kalman filter methods, were found to be comparable. However the way these methods work leads to discrete estimate space for the variance method and continuous space for the Kalman filter method with less scattering.

A novel magneto-rheological fluid (MRF) based tactile display is proposed and its magnetic FE model is constructed and validated by Gauss meter measurements. An accurate finite element (FE) model of human finger pad is constructed and validated in experiments of finger pad contact with soft and relatively rigid materials. Hyperfoam material parameters of the identified elastomers from the Chapter 2 are used for validation of the finger pad model. FE models of the human finger pad and the proposed tactile display are used in a model based control scenario for the proposed display. FE models of the elastomers developed in Chapter 2 are used for calculation of control curves for these elastomers. An experiment is set up for evaluation of the

proposed display. Experiments are performed on biological tissue and soft nonlinear foams. The results of experiments represented in this work show that the proposed control model and the display design are suitable for tactile applications such as displaying softness. Future work, such as recreation of softness for stiffer materials, will necessitate the use of stronger electromagnetic and amplifier circuits.

A novel system for displaying the softness of nonlinear materials was proposed and tested based on linear actuator. The main components consisted of a linear actuator, a force sensor, and processing software for each of which a detailed description was provided. Contact of human finger pad with the proposed display is modeled and deformation in finger pad is considered for controlling the actuator.The mechanical properties of various materials were characterized by conducting mechanical compression tests. These data were used by the processing software to actuate the display. A Proportional-Integral-Derivative (PID) controller was designed and optimized to control the shaft of the actuator to produce the same sensation of softness measured by the force sensor. Different materials were simulated by the tactile display and compared to the real objects. Experiments were conducted on the tactile display using human subjects and the results were recorded and presented. The results showed that the developed tactile display can replicate the softness of materials very closely and has great potential for identifying and categorizing objects by touch. In summation, it has proved to be a feasible technique with great potential use in robotic surgery, training facilities, virtual reality and minimally invasive surgery (MIS).

6.2 Future Work

Various optimization algorithms will yield different accuracy and performance for inverse modeling problems. Effect of each algorithm can be accurately investigated and compared to come up with an efficient (high accuracy) approach for the problem of material parameter identification with inverse FE modeling. For instance, results of inverse FE modeling on 2^{nd} order Hyperfoam model based on various local and global optimization methods are presented in Fig. 89. Efficient parallelization of the MultiStart method will also be investigated.

Based on our research on developing an in-house FE solution engine [124], it was found that a natively developed FE solver is efficient in orders of 600% compared to the solvers found in standard FE modeling software packages, e.g. Abaqus and ANSYS. Therefore, an efficient solver can be developed for the FE model of indentation to avoid use of pre-evaluated FE models.

Two perpendicular magnetic fields can be achieved on a plane by use of two ring shaped electromagnets as shown in Fig. 90. This particular design might help achieving more uniform and strong flux density in the MR fluid of the softness display. Next step will be 3D magnetic FE modeling of this proposed design and subsequent prototyping.

The simple linear actuator will be replaced by voice coil actuator for the softness display. Voice coil based actuators can attain higher actuation speeds compared to simple linear actuators based on rotary servos. Also, the voice coil based actuators

are almost noiseless.

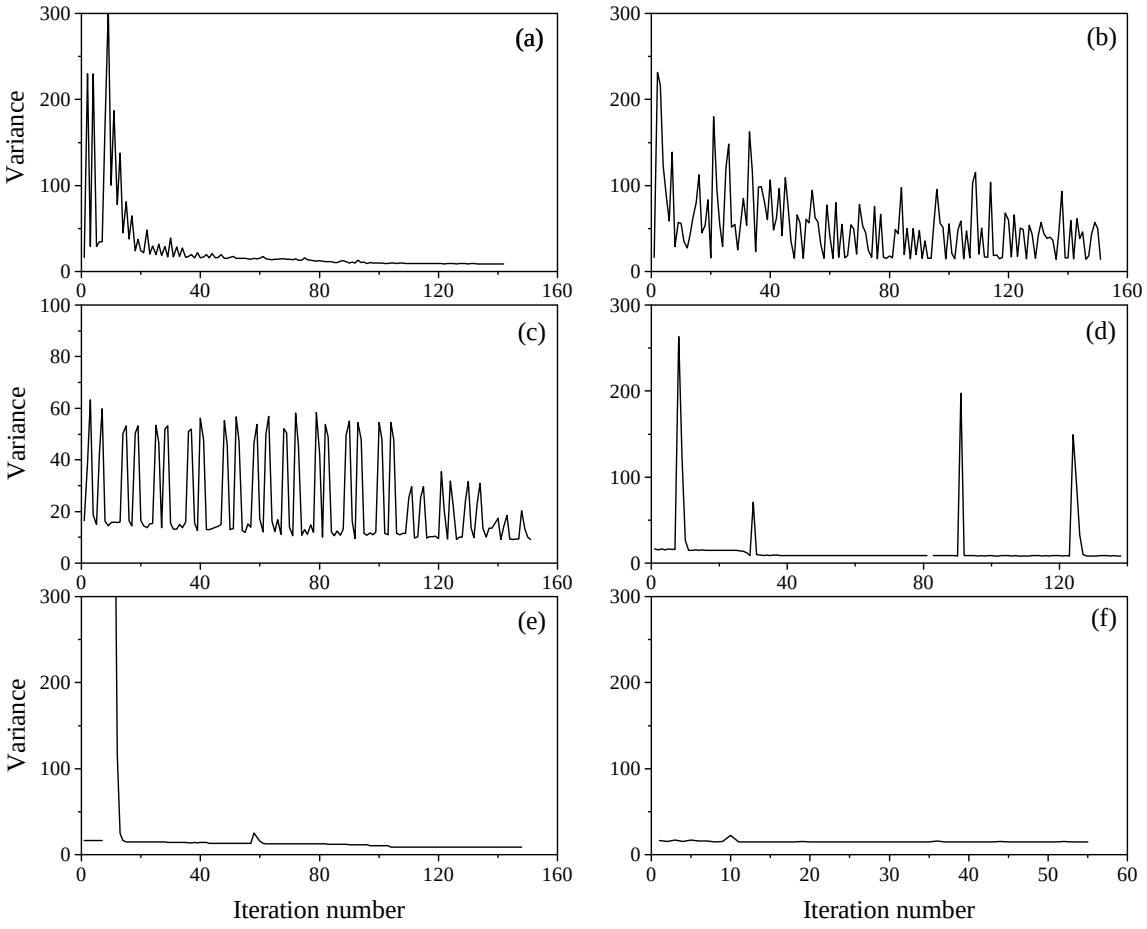

Figure 89: Objective function of optimization for material parameter identification based on inverse FE modeling using various optimization algorithms: (a) Nelder-Mead (Downhill Simplex), (b) Evolutionary algorithm, (c) Hooke-Jeeves, (d) Large Scale Generalized Reduced Gradient (LSGRG), (e) Mixed-Integer Sequential Quadratic Programming (MISQP) and (f) Modified Method of Feasible Directions (MMFD).

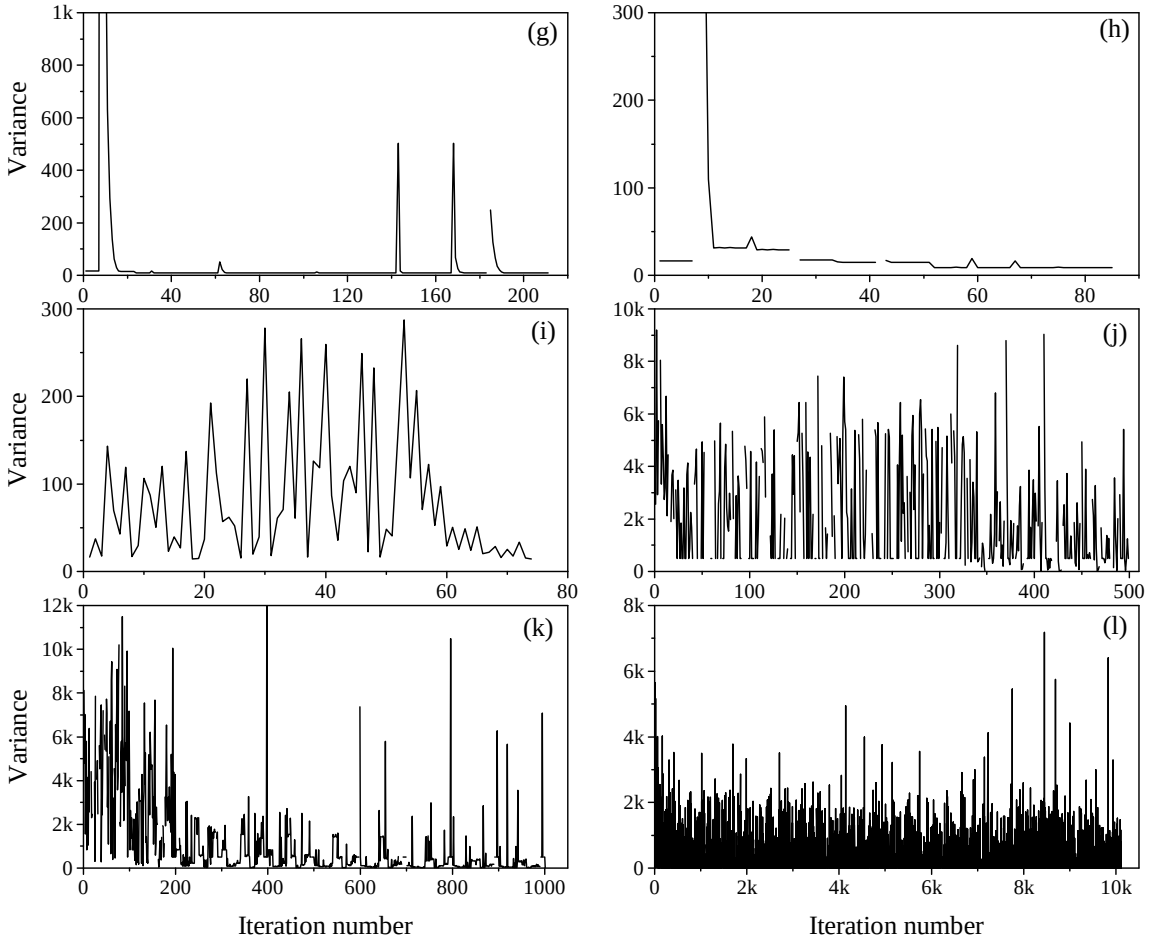

Figure 89 (cont'd.): (g) Multifunction Optimization System Tool (MOST), (h) Sequential Quadratic Programming (NLPQL), (i) Pointer Automatic Optimizer, (j) Multi-Objective Particle Swarm Optimization, (k) Multi-Island GA and (l) Adaptive simulated annealing (ASA).

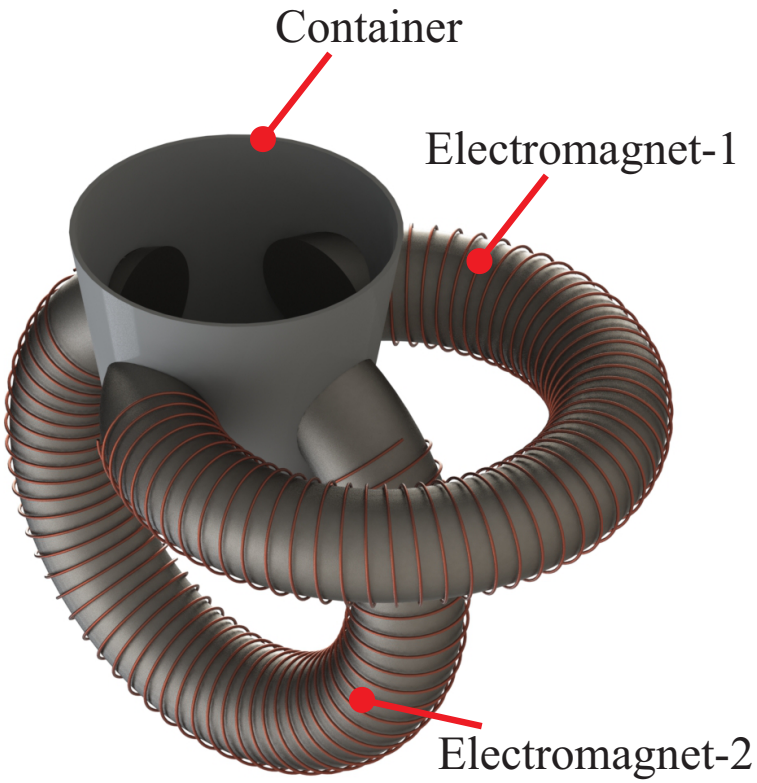

Figure 90: Proposed configuration for two ring shaped electromagnets in the MRF based softness display.

Bibliography

[1] T. Shannon, "Tactile communication attachment," 1973. US Patent 3,780,225.

[2] J. M. Loomis and S. J. Lederman, *Handbook of Perception and Human Performances Series*, vol. 2, ch. 31.Tactual Perception, pp. 2–3. John Wiley & Sons, 1986.

[3] F. J. Clark and K. W. Horch, *Handbook of Perception and Human Performance*, vol. 1, ch. Kinesthesia, pp. 1–62. John Wiley & Sons, 1986.

[4] L. A. Jones and E. Piateski, "Contribution of tactile feedback from the hand to the perception of force," *Experimental Brain Research*, vol. 168, pp. 298–302, Jan 2006.

[5] S. Kilbreath, K. Refshauge, and S. Gandevia, "Differential control of the digits of the human hand: evidence from digital anaesthesia and weight matching," *Experimental brain research*, vol. 117, no. 3, pp. 507–511, 1997.

[6] A. S. Augurelle, A. M. Smith, T. Lejeune, and J. L. Thonnard, "Importance of

cutaneous feedback in maintaining a secure grip during manipulation of hand-held objects," *Journal of neurophysiology*, vol. 89, no. 2, pp. 665–671, 2003.

[7] G. Cadoret and A. M. Smith, "Friction, not texture, dictates grip forces used during object manipulation.," *Journal of Neurophysiology*, vol. 75, no. 5, pp. 1963–9, 1996.

[8] E. Olivier, M. Davare, M. Andres, and L. Fadiga, "Precision grasping in humans: from motor control to cognition," *Current Opinion in Neurobiology*, vol. 17, pp. 644–648, Dec 2007.

[9] R. S. Johansson and J. R. Flanagan, "Coding and use of tactile signals from the fingertips in object manipulation tasks," *Nature reviews. Neuroscience*, vol. 10, no. 5, pp. 345–359, 2009.

[10] M. Graziano and M. M. Botvinick, "How the brain represents the body: insights from neurophysiology and psychology," *Common Mechanisms in Perception and Action: Attention and Performance*, vol. 19, pp. 136–157, 2002.

[11] M. Gentilucci, I. Toni, E. Daprati, and M. Gangitano, "Tactile input of the hand and the control of reaching to grasp movements," *Experimental Brain Research*, vol. 114, no. 1, pp. 130–137, 1997.

[12] R. S. Johansson and G. Westling, "Roles of glabrous skin receptors and sensorimotor memory in automatic control of precision grip when lifting rougher or

more slippery objects," *Experimental Brain Research*, vol. 56, no. 3, pp. 550–564, 1984.

[13] C. R. Wagner and R. D. Howe, "Force feedback benefit depends on experience in multiple degree of freedom robotic surgery task," *Robotics, IEEE Transactions on*, vol. 23, no. 6, pp. 1235–1240, 2007.

[14] E. P. Scilingo, M. Bianchi, G. Grioli, and A. Bicchi, "Rendering softness: Integration of kinesthetic and cutaneous information in a haptic device," *Haptics, IEEE Transactions on*, vol. 3, no. 2, pp. 109–118, 2010.

[15] J. R. Phillips and K. O. Johnson, "Tactile spatial resolution. iii. a continuum mechanics model of skin predicting mechanoreceptor responses to bars, edges, and gratings.," *Journal of Neurophysiology*, vol. 46, no. 6, 1981.

[16] R. S. Johansson, U. Landstrm, and R. Lundstrm, "Responses of mechanoreceptive afferent units in the glabrous skin of the human hand to sinusoidal skin displacements.," *Brain Research*, vol. 244, no. 1, pp. 17–25, 1982.

[17] D. Purves and et. al., *Neuroscience*. Sinauer Associates, Inc, 4th ed., 2008.

[18] R. Aster, B. Borchers, and C. Thurber, *Parameter Estimation and Inverse Problems*. Elsevier, 2013.

[19] R. Marti, M. G. C. Resende, and C. C. Ribeiro, "Multi-start methods for combinatorial optimization," *European Journal of Operational Research*, vol. 226, no. 1, pp. 1–8, 2013.

[20] G. Szekely, "Surgical simulators," *Minimally Invasive Therapy and Allied Technologies*, vol. 12, no. 1-2, pp. 14–18, 2003.

[21] J. G. Snedeker, P. Niederer, F. R. Schmidlin, M. Farshad, C. K. Demetropolous, J. B. Lee, and K. H. Yang, "Strain-rate dependent material properties of the porcine and human kidney capsule," *Journal of Biomechanics*, vol. 38, no. 5, pp. 1011–1021, 2005.

[22] J. Z. Wu, B. M. Wimer, D. E. Welcome, and R. G. Dong, "An analysis of contact stiffness between a finger and an object when wearing an air-cushioned glove: The effects of the air pressure," *Medical engineering & physics*, vol. 34, no. 3, pp. 386–393, 2012.

[23] M. Wiertlewski and V. Hayward, "Mechanical behavior of the fingertip in the range of frequencies and displacements relevant to touch," *Journal of Biomechanics*, vol. 45, no. 11, pp. 1869–1874, 2012.

[24] A. Andrade-Campos, P. Pilvin, J. Simes, and F. Teixeira-Dias, *Software engineering and development*, ch. Software Development for Inverse Determination of Constitutive Model Parameters, pp. 93–124. Nova Science Publishers, Inc, 2009.

[25] R. de Carvalho, R. Valente, and A. Andrade-Campos, "Optimization strategies for non-linear material parameters identification in metal forming problems," *Computers & Structures*, vol. 89, no. 1-2, pp. 246–255, 2011.

[26] L. Bilston, *Neural Tissue Biomechanics*. Springer Berlin Heidelberg, 2011.

[27] T. Nakamura, T. Wang, and S. Sampath, "Determination of properties of graded materials by inverse analysis and instrumented indentation," *Acta Materialia*, vol. 48, no. 17, pp. 4293–4306, 2000.

[28] B. Li, D. Gu, R. English, G. Rothwell, and X. Ren, "Characterisation of non-linear material parameters of foams based on indentation tests," *Materials & Design*, vol. 30, no. 7, pp. 2708–2714, 2009.

[29] Z. Chen and S. Diebels, "Nanoindentation of soft polymers: Modeling, experiments and parameter identification," *TECHNISCHE MECHANIK*, vol. 34, pp. 166–189, Oct 2013.

[30] Z. Chen and S. Diebels, "Parameter re-identification in nanoindentation problems of viscoelastic polymer layers: small deformation," *Journal of Applied Mathematics and Mechanics/Zeitschrift fr Angewandte Mathematik und Mechanik*, vol. 93, pp. 88–101, Feb 2012.

[31] M. G. Zhang, Y. P. Cao, G. Y. Li, and X. Q. Feng, "Spherical indentation method for determining the constitutive parameters of hyperelastic soft materials," *Biomechanics and Modeling in Mechanobiology*, vol. 13, pp. 1–11, Jan 2014.

[32] J. Hadamard, *Lectures on Cauchys problems in linear partial differential equations*. Yale University Press, 1923.

[33] A. Bummo, K. Yeongjin, K. O. Cheol, and K. Jung, "Robotic palpation and mechanical property characterization for abnormal tissue localization," *Med Biol Eng Comput*, vol. 50, no. 9, pp. 961–971, 2012.

[34] S. Singh, L. L. Fujii, M. H. Murad, Z. Wang, S. K. Asrani, R. L. Ehman, P. S. Kamath, and J. A. Talwalkar, "Liver stiffness is associated with risk of decompensation, liver cancer, and death in patients with chronic liver diseases: A systematic review and meta-analysis," *Clinical Gastroenterology and Hepatology*, vol. 11, no. 12, pp. 1573–1584, 2013.

[35] D. Klein, H. Freimuth, G. J. Monkman, S. Egersdrfer, A. Meier, H. Bse, M. Baumann, H. Ermert, and O. T. Bruhns, "Electrorheological tactel elements," *Mechatronics*, vol. 15, no. 7, pp. 883–897, 2005.

[36] J. A. Norton, T. H. Shawker, J. L. Doppman, D. L. Miller, D. L. Fraker, D. T. Cromack, P. Gorden, and R. T. Jensen, "Localization and surgical treatment of occult insulinomas," *Annals of Surgery*, vol. 212, no. 5, pp. 615–620, 1990.

[37] A. Gardner, "Annual breast exams, mammograms still key to detecting breast cancer." Internet, September 7, 2011 2011.

[38] C. Nies, R. Leppek, H. Sitter, H. J. Klotter, J. Riera, K. J. Klose, W. B. Schwerk, and M. Rothmund, "Prospective evaluation of different diagnostic techniques for the detection of liver metastases at the time of primary resection of colorectal carcinoma," *The European journal of surgery*, vol. 162, no. 10, pp. 811–816, 1996.

[39] T. S. Ravikumar, S. Buenaventura, R. R. Salem, and B. D'Andrea, "Intraoperative ultrasonography of liver: detection of occult liver tumors and treatment by cryosurgery," *Cancer detection and prevention*, vol. 18, no. 2, pp. 131–138, 1994.

[40] H. Xin, J. S. Zelek, and H. Carnahan, "Laparoscopic surgery, perceptual limitations and force: A review," in *First Canadian student Conference on Biomedical Computing*, 2006.

[41] G. Moy, "Bidigital teletaction system design and performance," 2002.

[42] J. P. Ruurda and I. M. A. J. Broeders, "Feasibility of robot-assisted laparoscopic cholecystectomy," in *International Congress Series*, vol. 1230, pp. 160–165, Elsevier, 2001.

[43] D. Ota, "Laparoscopic colectomy for cancer: A favorable opinion," *Annals of Surgical Oncology*, vol. 2, no. 1, pp. 3–5, 1995.

[44] W. A. Bemelman, J. Ringers, D. W. Meijer, C. W. M. de Wit, and J. J. G. Bannenberg, "Laparoscopic-assisted colectomy with the dexterity pneumo sleeve," *Diseases of the colon and rectum*, vol. 39, pp. S59–S61, Oct 1996.

[45] M. Beccani, C. Di Natali, M. Rentschler, and P. Valdastri, "Uniaxial wireless tissue palpation device for minimally invasive surgery," *Journal of Medical Devices*, vol. 7, no. 2, pp. 020919–22, 2013.

[46] M. Beccani, C. Di Natali, C. E. Benjamin, C. S. Bell, N. E. Hall, and P. Valdastri, "Wireless tissue palpation: Head characterization to improve tumor detection in soft tissue," *Sensors & Actuators: A.Physical*, vol. 223, pp. 180–190, 2015.

[47] X. Wang, C. Di Natali, M. Beccani, M. Kern, P. Valdastri, and M. Rentschler, "Novel medical wired palpation device: A validation study of material properties," in *The 17th International Conference on Solid-State Sensors, Actuators and Microsystems (TRANSDUCERS & EUROSENSORS XXVII), 2013 Transducers & Eurosensors XXVII*, pp. 1653–1658, Jun 2013.

[48] H. Liu, J. Li, X. Song, L. D. Seneviratne, and K. Althoefer, "Rolling indentation probe for tissue abnormality identification during minimally invasive surgery," *IEEE Transactions on Robotics*, vol. 27, no. 3, pp. 450–460, 2011.

[49] A. Chiorean, M. D. Magdalena, S. M. Dudea, A. Iancu, D. Dumitriu, R. Roman, and S. Sfringeu, "Real-time ultrasound elastography of the breast: state of the art," *Medical Ultrasonography*, vol. 10, no. 2, pp. 73–82, 2008.

[50] K. Kato, H. Sugimoto, N. Kanazumi, S. Nomoto, S. Takeda, and A. Nakao, "Intra-operative application of real-time tissue elastography for the diagnosis of liver tumours," *Liver International*, vol. 28, no. 9, pp. 1264–1271, 2008.

[51] K. Miller and K. Chinzei, "Constitutive modelling of brain tissue: Experiment and theory," *Journal of Biomechanics*, vol. 30, no. 1112, pp. 1115–1121, 1997.

[52] K. Miller, "Constitutive model of brain tissue suitable for finite element analysis of surgical procedures," *Journal of Biomechanics*, vol. 32, no. 5, pp. 531–537, 1999.

[53] C. H. King, M. Franco, M. O. Culjat, A. T. Higa, J. W. Bisley, E. Dutson, and W. S. Grundfest, "Fabrication and characterization of a balloon actuator array for haptic feedback in robotic surgery," *Journal of Medical Devices*, vol. 2, no. 4, pp. 041006–13, 2008.

[54] J. Dargahi, S. Arbatani, S. Sokhanvar, W. F. Xie, and R. Ramezanifard, "A novel tactile softness display for minimally invasive surgery," *Mechatronics*, vol. 24, no. 8, pp. 1144–1156, 2014.

[55] N. Sgambelluri, E. Scilingo, R. Rizzo, and A. Bicchi, *A Free-Hand Haptic Interface Based on Magnetorheological Fluids*, vol. 45, pp. 155–178. Springer Berlin Heidelberg, 2008.

[56] N. Sgambelluri, E. P. Scilingo, A. Bicchi, R. Rizzo, and M. Raugi, "Advanced modelling and preliminary psychophysical experiments for a free-hand haptic device," in *Intelligent Robots and Systems, 2006 IEEE/RSJ International Conference on*, pp. 1558–1563, 2006.

[57] E. P. Scilingo, N. Sgambelluri, D. De Rossi, and A. Bicchi, "Towards a haptic black box for free-hand softness and shape exploration," in *Robotics and Automation, 2003. Proceedings. ICRA '03. IEEE International Conference on*, vol. 2, pp. 2412–2417, 2003.

[58] A. Bicchi, M. Raugi, R. Rizzo, and N. Sgambelluri, "Analysis and design of an electromagnetic system for the characterization of magneto-rheological fluids for haptic interfaces," *Magnetics, IEEE Transactions on*, vol. 41, no. 5, pp. 1876–1879, 2005.

[59] R. Rizzo, "A permanent-magnet exciter for magneto-rheological fluid-based haptic interfaces," *Magnetics, IEEE Transactions on*, vol. 49, no. 4, pp. 1390–1401, 2013.

[60] G. Moy, S. Singh, E. Tan, and R. S. Fearing, "Human psychophysics for teletaction system design," *Haptics-e*, vol. 1, no. 3, pp. 1–20, 2000.

[61] W. J. Peine, P. S. Wellman, and R. D. Howe, "Temporal bandwidth requirements for tactile shape displays," in *Proceedings of the IMECE Haptics Symposium*, pp. 107–113, 1997.

[62] K. O. Johnson and J. R. Phillips, "Tactile spatial resolution. i. two-point discrimination, gap detection, grating resolution, and letter recognition," *Journal of Neurophysiology*, vol. 46, pp. 1177–92, Dec 1981.

[63] R. Perline, R. Kornbluh, J. Joseph, R. Heydt, Q. Pei, and S. Chiba, "High-field deformation of elastomeric dielectrics for actuators," *Materials Science and Engineering: C*, vol. 11, no. 2, pp. 89–100, 2000.

[64] M. Jungmann and H. Schlaak, "Miniaturised electrostatic tactile display with high structural compliance," in *Proc. of the Eurohaptics*, (Edinburgh, U.K.), 2002.

[65] A. Yamamoto, S. Nagasawa, H. Yamamoto, and T. Higuchi, "Electrostatic tactile display with thin film slider and its application to tactile telepresentation systems," *IEEE Transactions on Visualization and Comput. Graphics*, vol. 12, pp. 168–177, 2006.

[66] M. V. Ottermo, . Stavdahl, and T. A. Johansen, "A remote palpation instrument for laparoscopic surgery: Design and performance," *Minimally Invasive Therapy & Allied Technologies*, vol. 18, no. 5, pp. 259–272, 2009.

[67] M. V. Ottermo, . Stavdahl, and T. A. Johansen, "Design and performance of a prototype tactile shape display for minimally invasive surgery," *Haptics-e: The Electronic Journal of Haptics Research*, vol. 4, pp. 1–13, 2008.

[68] P. Wellman, W. J. Peine, G. Favalora, and R. D. Howe, "Mechanical design and control of a high-bandwidth shape memory alloy tactile display," in *Proceedings of the 5th International Symposium on Experimental Robotics V*, (Barcelona, Catalonia), 1997.

[69] R. Velazquez, E. Pissaloux, M. Hafez, and J. Szewczyk, "A low-cost highly-portable tactile display based on shape memory alloy micro-actuators," in *Virtual Environments, Human-Computer Interfaces and Measurement Systems (VECIMS 2005)*, (Sicily, Italy), 2005.

[70] J. Pasquero and V. Hayward, "Stress: A practical tactile display system with one millimeter spatial resolution and 700 hz refresh rate," in *Proceedings of Eurohaptics*, (Dublin), 2003.

[71] Y. Seung-kook, K. Sungchul, K. Dong-Soo, and C. Hyoukreol, "Tactile sensing to display for tangible interface," in *IEEE/RSJ International Conference on Intelligent Robots and Systems*, (Beijing, China), 2006.

[72] Y. Makino and H. Shinoda, "Suction pressure tactile display using dual temporal stimulation modes," in *Proc. SICE Annual Conference*, (Okayama, Japan), Aug 2005.

[73] Y. Makino, N. Asamura, and H. Shinoda, "Multi primitive tactile display based on suction pressure control," in *Proc. IEEE 12th Symposium on Haptic Interfaces for Virtual Environment and Teleoperator Systems, (Haptic Symposium 2004)*, (Chicago), pp. 90–96, Mar 2004.

[74] Y. Makino, N. Asamura, and H. Shinoda, "A whole palm tactile display using suction pressure," in *Proc. 2004 IEEE Int. Conf. on Robotics & Automation*, (New Orleans), pp. 1524–1529, Apr 2004.

[75] O. C. Jeong and S. S. Yang, "Fabrication and test of a thermopneumatic micropump with a corrugated p+ diaphragm," *Journal of Sensors and Actuators A: Physical*, vol. 83, pp. 249–255, 2000.

[76] F. V. Verdu and R. N. Gonzalez, "Thermopneumatic actuator for tactile displays," in *18th Conference on Design of Circuits and Integrated Systems DCIS*, 2003.

[77] J. S. Lee and S. Lucyszyn, "A micromachined refreshable braille cell," *Journal of Microelectromechanical Systems*, vol. 14, pp. 673–682, 2005.

[78] W. K. Vos, D. G. Buma, and P. H. Veltink, "Towards the optimisation of spatial electrocutaneous display parameters for sensory substitution," in *7th Annual Conf. of the International Functional Electrical Stimulation Society*, (Ljubljana, Slovenia), 2004.

[79] K. Hayashi and M. Takahata, "Objective evaluation of tactile sensation for tactile communication," *NTT DoCoMo Technical Journal*, vol. 7, pp. 39–43, 2005.

[80] T. Yamamoto, B. Vagvolgyi, K. Balaji, L. Whitcomb, and A. M. Okamura, "Tissue property estimation and graphical display for teleoperated robot-assisted surgery," in *IEEE International Conference on Robotics and Automation*, (Kobe, Japan), 2009.

[81] M. Kalantari, M. Ramezanifard, J. Dargahi, and J. Kovecses, "3d graphical rendering of localized lumps and arteries for robotic assisted mis," *Journal of Medical Devices Devices*, vol. 5, pp. 021002–10, 2011.

[82] I. M. Koo, K. Jung, J. C. Koo, J.-D. Nam, Y. K. Lee, and H. R. Choi, "Development of soft-actuator-based wearable tactile display," *IEEE Transactions on Robotics*, vol. 24, pp. 549–558, Jun 2008.

[83] M. O. Culjat, C. H. King, M. Franco, J. W. Bisley, W. S. Grundfest, and E. Dutson, "Pneumatic balloon actuators for tactile feedback in robotic surgery," *Industrial Robot: An International Journal*, vol. 35, no. 5, pp. 449–455, 2008.

[84] S.-C. Kim, C. H. Kim, T.-H. Yang, G.-H. Yang, S.-C. Kang, and D.-S. Kwon, "Salt: Small and lightweight tactile display using ultrasonic actuators," in *Robot and Human Interactive Communication, 2008. RO-MAN 2008. The 17th IEEE International Symposium on*, pp. 430–435, Aug 2008.

[85] F. Kimura, A. Yamamoto, and T. Higuchi, "Development of a 2-dof softness feeling display for tactile tele-presentation of deformable surfaces," in *Robotics and Automation (ICRA), 2010 IEEE International Conference on*, pp. 1822–1827, May 2010.

[86] J. Liu, "Real-time softness display system for the perception of virtual objects," in *Audio Language and Image Processing (ICALIP), 2010 International Conference on*, 2010.

[87] D. Burch and D. Pawluk, "Using multiple contacts with texture-enhanced graphics," in *World Haptics Conference (WHC), 2011 IEEE*, pp. 287–292, Jun 2011.

[88] C. Cameron, L. DiValentin, R. Manaktala, A. McElhaney, C. Nostrand, O. Quinlan, L. Sharpe, A. Slagle, C. Wood, Y. Y. Zheng, and G. Gerling, "Using electroactive polymers to simulate the sense of light touch and vibration in a virtual reality environment," in *Systems and Information Engineering Design Symposium*, pp. 121–126, Apr 2011.

[89] F. Chinello, M. Malvezzi, C. Pacchierotti, and D. Prattichizzo, "A three dofs wearable tactile display for exploration and manipulation of virtual objects," in *IEEE Haptics Symposium (HAPTICS)*, pp. 71–76, Mar 2012.

[90] J. Watanabe, H. Ishikawa, X. Arouette, Y. Matsumoto, and N. Miki, "Artificial tactile feeling displayed by large displacement mems actuator arrays," in *IEEE 25th International Conference on Micro Electro Mechanical Systems (MEMS)*, pp. 1129–1132, Jan 2012.

[91] Y. Gu, T. Nakamura, L. Prchlik, S. Sampath, and J. Wallace, "Micro-indentation and inverse analysis to characterize elastic-plastic graded materials," *Materials Science and Engineering: A*, vol. 345, no. 12, pp. 223–233, 2003.

[92] L. Li, *Development of inverse modeling programs for material parameter identification in testing soft materials*. PhD thesis, Liverpool John Moores University, 2008.

[93] "Section 22.5.2, abaqus analysis user's manual," 2012.

[94] "Section 4.8.2. abaqus theory manual," 2012.

[95] M. Grdiac and A. Vautrin, "A new method for determination of bending rigidities of thin anisotropic plates," *Journal of Applied Mechanics*, vol. 57, no. 4, pp. 964–968, 1990.

[96] A. Tarantola, *Inverse Problem Theory and Methods for Model Parameter Estimation*. Society for Industrial and Applied Mathematics, 2005.

[97] D. S. Schnur and N. Zabaras, "An inverse method for determining elastic material properties and a material interface," *International Journal for Numerical Methods in Engineering*, vol. 33, no. 10, pp. 2039–2057, 1992.

[98] J. C. Gelin and O. Ghouati, "An inverse method for determining viscoplastic properties of aluminium alloys," *Journal of Materials Processing Technology*, vol. 45, no. 1-4, pp. 435–440, 1994.

[99] J. A. Nelder and R. Mead, "A simplex method for function minimization," *The Computer Journal*, vol. 7, no. 4, pp. 308–313, 1965.

[100] T. Kolda, R. Lewis, and V. Torczon, "Optimization by direct search: New perspectives on some classical and modern methods," *SIAM Review*, vol. 45, no. 3, pp. 385–482, 2003.

[101] S. Kucharski and Z. Mrz, "Identification of yield stress and plastic hardening parameters from a spherical indentation test," *International Journal of Mechanical Sciences*, vol. 49, no. 11, pp. 1238–1250, 2007.

[102] H. C. Hyun, J. H. Lee, M. Kim, and H. Lee, "A spherical indentation technique for property evaluation of hyperelastic rubber," *Journal of Materials Research*, vol. 1, no. 1, pp. 1–14, 2012.

[103] L. P. Tendela and G. H. Kaufmann, "Evaluation of coating adhesion using a radial speckle interferometer combined with a micro-indentation test," *Optics and Lasers in Engineering*, vol. 50, no. 6, pp. 817–822, 2012.

[104] J. E. Zorzi and C. A. Perottoni, "Estimating youngs modulus and poissons ratio by instrumented indentation test," *Materials Science and Engineering: A*, vol. 574, pp. 25–30, 2013.

[105] M. L. Wilkins, "Calculation of elastic-plastic flow," in *Methods of Computational Physics*, vol. 3, Academic Press, 2002.

[106] K. Bathe, E. Ramm, and E. Wilson, "Finite element formulations for large deformation dynamic analysis," *International Journal for Numerical Methods in Engineering*, vol. 9, pp. 353–386, 1975.

[107] K. Bathe, "An assessment of current finite element analysis of nonlinear problems in solid mechanics," in *Numerical solution of partial differential equations – III*, Univ. Maryland, 1975.

[108] R. W. Shen and G. Lei, *Introduction to the Explicit Finite Element Method for Nonlinear Transient Dynamics.* John Wiley & Sons, 2012.

[109] R. E. Kalman, "A new approach to linear filtering and prediction problems," *Journal of Fluids Engineering*, vol. 82, no. 1, pp. 35–45, 1960.

[110] M. S. Grewal and A. P. Andrews, *Kalman Filtering: Theory and Practice*. Upper Saddle River, NJ, USA: Prentice-Hall, Inc, 1993.

[111] D. Simon and T. L. Chia, "Kalman filtering with state equality constraints," *Aerospace and Electronic Systems, IEEE Transactions on*, vol. 38, no. 1, pp. 128–136, 2002.

[112] S. Ungarala, E. Dolence, and K. Li, "Constrained extended kalman filter for nonlinear state estimation," in *Proceedings of the Eighth International IFAC Symposium on Dynamics and Control of Process Systems*, vol. 2, pp. 63–68, 2007.

[113] M. Gao, Z. He, and Y. Liu, "Improved unscented kalman filter for bounded state estimation," in *2011 International Conference on Electronics, Communications and Control (ICECC)*, pp. 2101–2104, 2011.

[114] C. D. Clemente, *Anatomy, a regional atlas of the human body*. Urban & Schwarzenberg, 1981.

[115] J. Z. Wu, R. G. Dong, and D. E. Welcome, "Analysis of the point mechanical impedance of fingerpad in vibration," *Medical engineering & physics*, vol. 28, no. 8, pp. 816–826, 2006.

[116] P. E. Allaire, *Basics of the finite element method*. Brooks/Cole, 1985.

[117] N. Wereley, *Magnetorheology: advances and applications*, vol. 6. Royal Society of Chemistry, 2013.

[118] M. Ramezanifard, "Design and development of new tactile softness displays for minimally invasive surgery," Master's thesis, Concordia University, 2008.

[119] E. R. Serina, E. Mockensturm, C. M. Jr., and D. Rempel, "A structural model of the forced compression of the fingertip pulp," *Journal of Biomechanics*, vol. 31, no. 7, pp. 639–646, 1998.

[120] D. T. V. Pawluk and R. D. Howe, "Dynamic lumped element response of the human fingerpad," *Journal of Biomechanical Engineering*, vol. 121, no. 2, pp. 178–183, 1999.

[121] Y. C. Fung, *Biomechanics: Mechanical Properties of Living Tissues*. Springer-Verlag New York, 1993.

[122] K. L. Johnson, *Contact Mechanics*. Cambridge University Press, 1987.

[123] A. Bicchi, E. P. Scilingo, and D. De Rossi, "Haptic discrimination of softness in teleoperation: the role of the contact area spread rate," *Robotics and Automation, IEEE Transactions on*, vol. 16, pp. 496–504, Oct 2000.

[124] S. Arbatani, A. Callejo, J. Kövecses, M. Kalantari, N. R. Marchand, and J. Dargahi, "An approach to directional drilling simulation: finite element and finite segment methods with contact," *Computational Mechanics*, pp. 1–15, 2016.

[125] "Matlab 7, function reference," 2008.

[126] J. C. Lagarias, J. A. Reeds, M. H. Wright, and P. E. Wright, "Convergence properties of the nelder-mead simplex method in low dimensions," *SIAM Journal on Optimization*, vol. 9, no. 1, pp. 112–147, 1998.

[127] M. H. Wright, "Direct search methods: Once scorned, now respectable," in *Proceedings of the 1995 Dundee Biennial Conference in Numerical Analysis*, vol. 334, 1995.

[128] K. Bathe in *Finite element procedures*, Prentice Hall, 1996.

[129] K. Bathe and S. Bolourchi, "Large displacement analysis of three-dimensional beam structures," *International Journal for Numerical Methods in Engineering*, vol. 14, pp. 961–986, 1979.

Appendices

Appendix A

Nelder-Mead Simplex Algorithm

Different methods of implementation are proposed for Nelder-Mead simplex method based on construction of the initial simplex and convergence or termination tests. The main algorithm is implemented as shown in the following steps [125, 126]:

a) Construct the initial simplex by $(n+1)$ vertices, P_0, P_1, ..., P_n around a given vertex P_{in}

$$P_i = P_0 + h_j e_j, \quad P_0 = P_{in}, \quad j = 1, \ldots, n \tag{57}$$

where h_j is the step size in direction of the unit vector e_j.

b) Determine the best, worst and second worst vertices in current simplex, f_l, f_h and f_s, respectively.

$$f_h = max\left(f_j\right), \quad f_l = min\left(f_j\right), \quad f_s = max\left(f_{j\neq h}\right), \quad j = 0, \ldots, n \tag{58}$$

where f_j is the value of function at vertex j.

c) Calculate the centroid c between vertices with index of $j \neq h$.

$$c = \frac{1}{n} \sum_{j \neq h} P_j, \quad j = 0, \ldots, n \tag{59}$$

d) Construct a new working simplex (simplex transformation). In this step, first try

to replace the worst vertex (P_h) by a new one. Replacing the worst vertex would be done by means of reflection, expansion or contraction processes. If replacement fails, then shrink the simplex toward P_l and calculate n new vertices. Four parameters are defined in this step of Nelder-Mead algorithm, α, γ, ρ and σ each for reflection, expansion, contraction and shrinkage, respectively with following constraints:

$$\alpha > 0,\ \gamma > 1,\ 0 < \rho < 1 \quad and \quad \sigma < 0 \tag{60}$$

Values used in this implementation are as follows:

$\alpha = 1$, $\gamma = 2$, $\rho = -0.5$ and $\sigma = 0.5$

Lagarias et al. and Wright [126, 127] have described the step of new simplex construction and is shown in Fig. 91.

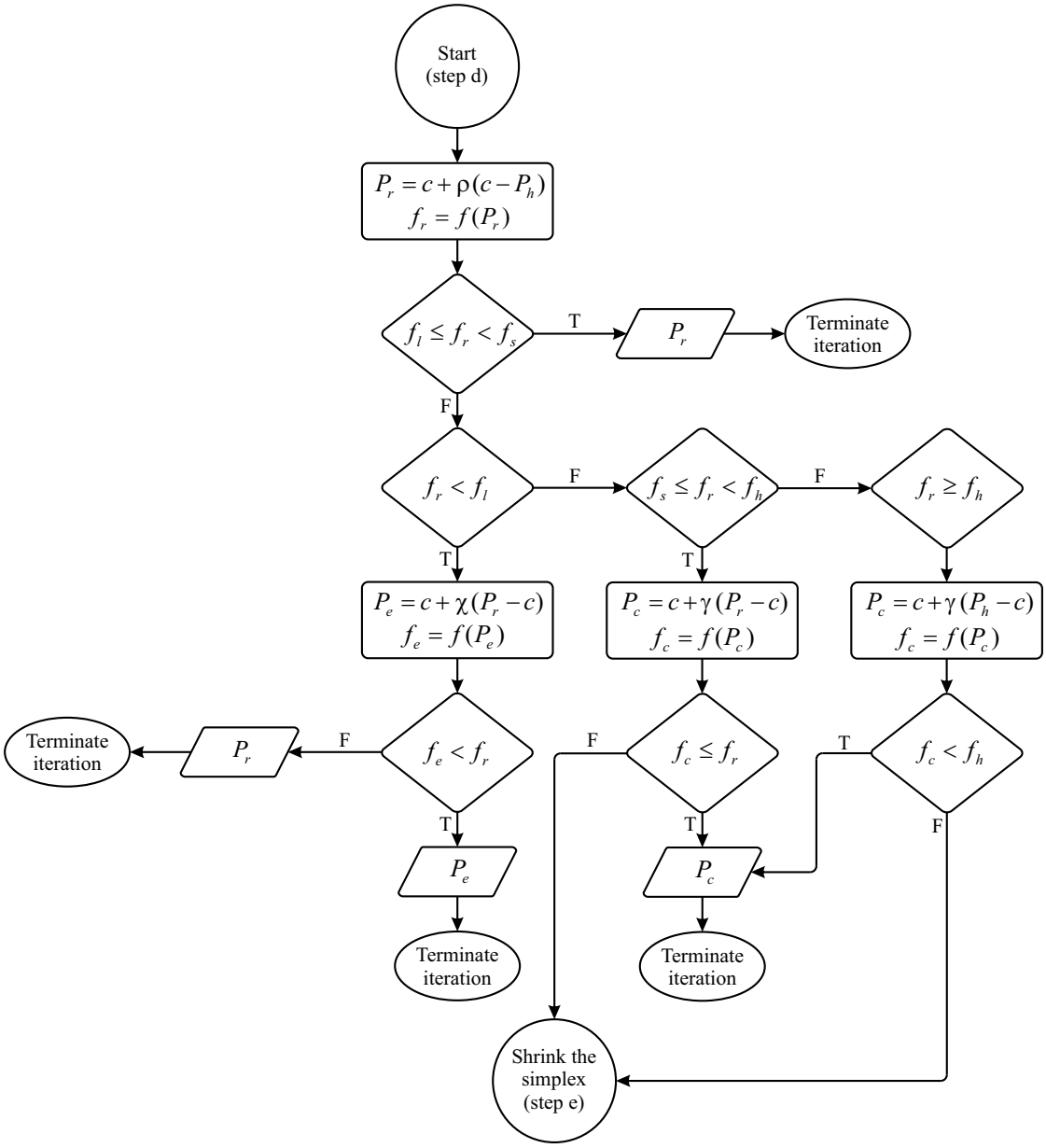

Figure 91: Flowchart of the transformation step of the Nelder-Mead algorithm.

Fig. 91 shows the flowchart of the transformation step (reflection, expansion and contraction) of the Nelder-Mead algorithm. In this flowchart, c is the centroid of the n best points, P_r, P_e and P_c are reflection, expansion and contraction points and f_x is value of function at point x. Effect of reflection, expansion, contraction and shrinkage in a two-dimensional space is shown in Fig. 92.

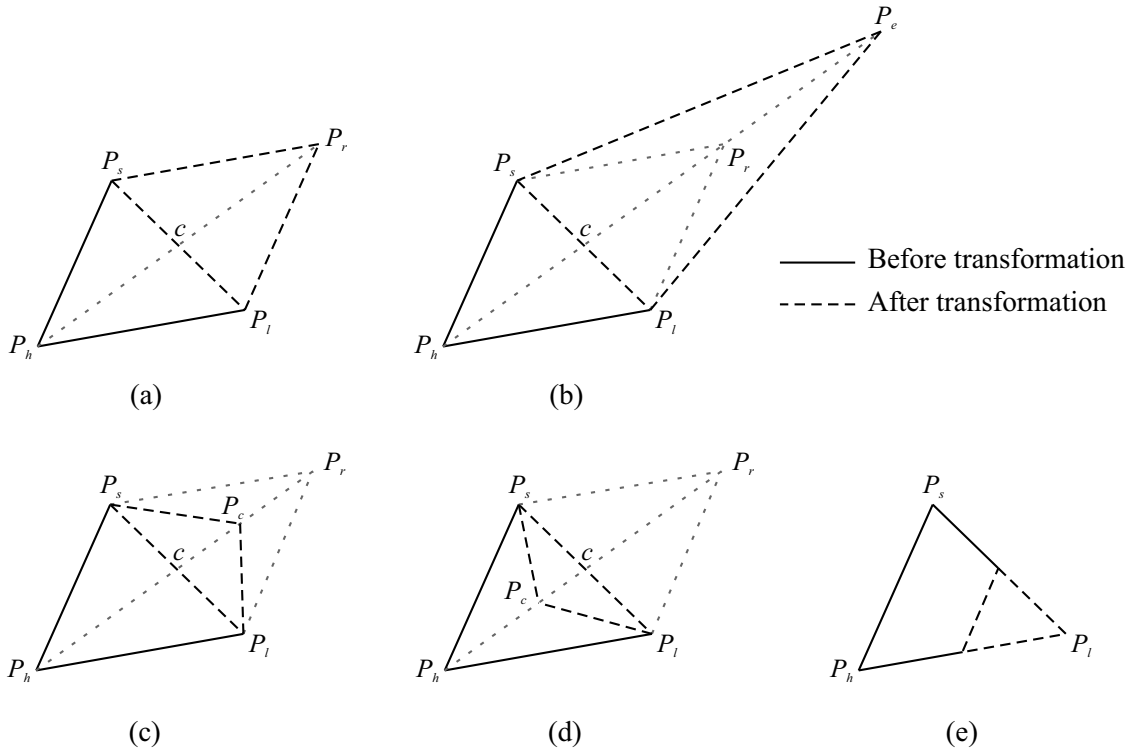

Figure 92: Transformation to a new simplex in two-dimensional space.

Fig. 92 shows the transformation to a new simplex (triangle) in two-dimensional space in the Nelder-Mead algorithm by (a) reflection, (b) expansion, (c) and (d) contraction, (e) shrink. The original simplex is shown in solid line.

***e*)** This step is suggested by Lagarias [126] to prevent failure of the algorithm during the contraction step in case of a curved valley and a vertex far away from the valley compared to the other vertices. In this case, n new vertices would be calculated as below, and the algorithm will continue with new vertices P_l, V_1, ..., V_n (Fig. 92-e)

$$V_j = P_l + \sigma\left(P_j + P_l\right), \quad j = 1, \ldots, n, \quad j \neq l \tag{61}$$

***f*)** Test convergence and terminate the process. Three scenarios would be checked in this step as follows:

Scenario 1. If the distance between vertices P_j is smaller than a given value (simplex is sufficiently small), terminate the process.

Scenario 2. If f_j is close enough to a certain value, terminate the process.

Scenario 3. If the number of iterations exceed a certain allowed value, terminate the process.

In this research, the Nelder-Mead algorithm is implemented using Python programming language in order to couple with the Abaqus FE modeling software.

Appendix B

Updated Lagrangian Method

Effectiveness of the Updated Lagrangian algorithm employed in the Abaqus software lies in the use of a lumped or diagonal mass matrix, which makes the integration steps trivial. The formulation accounts for large axial, bending and shear deformations as well as large translation and rotation of the elements used. Also, since there is no need for computing the system stiffness matrix, the solution is essentially carried out at the element level, and thus large systems can be efficiently handled.

Following the updated Lagrangian method with explicit integration, the nonlinear response is calculated at each time step by considering changes in the stiffness properties and boundary conditions [128]. The equilibrium of the finite element model at time t is considered to be:

$$\mathbf{M}\ {}^{t}\ddot{\mathbf{u}} + \mathbf{C}\ {}^{t}\dot{\mathbf{u}} = {}^{t}\mathbf{R} - {}^{t}\mathbf{F} \tag{62}$$

where ${}^{t}\dot{\mathbf{u}}$ and ${}^{t}\ddot{\mathbf{u}}$ are the velocity and acceleration vectors, $\mathbf{M} \in \mathbb{R}^{n\times n}$ is the mass matrix, $\mathbf{C} \equiv \alpha\mathbf{M} \in \mathbb{R}^{n\times n}$ is the damping matrix, α is the mass-proportional damping coefficient, ${}^{t}\mathbf{R} \in \mathbb{R}^{n}$ is the external load vector and ${}^{t}\mathbf{F} \in \mathbb{R}^{n}$ is the internal force vector in global coordinates.

The displacement vector ${}^{t+h}\mathbf{u}$ can be obtained by way of a central difference

approach, as explained in [129]:

$$(a_0\mathbf{M} + a_1\mathbf{C})\ {}^{t+h}\mathbf{u} = {}^{t}\hat{\mathbf{R}} \tag{63}$$

$${}^{t}\hat{\mathbf{R}} = {}^{t}\mathbf{R} - {}^{t}\mathbf{F} + a_2\mathbf{M}\ {}^{t}\mathbf{u} - (a_0\mathbf{M} - a_1\mathbf{C})\ {}^{t-h}\mathbf{u} \tag{64}$$

where ${}^{t}\hat{\mathbf{R}} \in \mathbb{R}^n$ is the effective load vector, h is the time step, $a_0 = 1/h^2$, $a_1 = 1/(2h)$ and $a_2 = 2a_0$ are integration constants. As it can be seen in Eq. (63), the use of diagonal or lumped mass and damping matrices enables a trivial evaluation process for the displacement vector (${}^{t+h}\mathbf{u}$). The lumped mass matrix can be assembled based on the individual diagonal element mass matrices.

The nodal force vector is assembled in terms of individual force vectors, based on the element connectivity:

$${}^{t}\mathbf{F}_j = \mathbf{K}\ {}^{t}\mathbf{u}_j \tag{65}$$

$$\mathbf{K} \equiv \mathbf{K}_{\mathrm{L}} + \mathbf{K}_{\mathrm{NL}} \tag{66}$$

where ${}^{t}\mathbf{F}_j \in \mathbb{R}^6$ is the internal force vector of the jth element, consisting of two axial components and one torque per node, $\mathbf{K}$ is the sum of the linear ($\mathbf{K}_{\mathrm{L}}$) and nonlinear ($\mathbf{K}_{\mathrm{NL}}$) stiffness matrices of the jth element, and ${}^{t}\mathbf{u}_j$ is the displacement vector of the jth element.

An important consideration in this approach is the use of a time step h smaller than a critical value, h_{cr}. The critical time step can be calculated through the stiffness properties and mass of the system. As an example, in a system of planar beam elements, h_{cr} is the smallest travel time of the stress wave between two neighboring nodes [128]:

$$h < h_{\mathrm{cr}} \tag{67}$$

$$h_{\mathrm{cr}} = \frac{L}{\sqrt{E/\rho}} \tag{68}$$

where L is the length of the smallest element or the smallest distance between two neighboring nodes, and ρ is the mass density of the element.

Appendix C

Python Code for Parameter Identification with Optimization

The following Python code can be executed under Abaqus's Python interface. Open source mathematic libraries, *scipy* and *numpy* are employed for the Nelder-Mead implementation.

Begin (optim.py)

```
from numpy import *
from scipy import minimize
import copy
from abaqusConstants import *
from abaqus import *
import csv
from odbAccess import *

####Input parameters
mdb_path='G:/Abaqus_temp/optim_paper/liver/model.cae'
report_file_name='report_liver.txt'
model_name='Model-1'
material_name='Material-1'
job_name_prefix='liver_r635_opt_'
initial_parameters=(0.012,7.429,2.5,0.8,0.0,1.0) #(mu, alpha, D1, gi, ki, ti)
```

```
node_number=0 # Indentation load measurement node number
file_path='G:/Abaqus_temp/optim_paper/liver/'
file_name_prefix='liver_r635_opt_'
exp_data_file_name='exp_data.txt'
####
counter=1
openMdb(pathName=mdb_path)
exp_file_handle=open(exp_data_file_name,'r')
report_file=open(report_file_name,'w')
report_file.write('mu\t'+'alpha\t'+'D1\t'+'gi\t'+'ki\t'+'ti\t'+'variance
    \n')#+'gi\t'+'ki\t'+'ti\t'
report_file.close()

exp_data=[]
for line in exp_file_handle:
    exp_data.append(float(line))

exp_file_handle.close()

def variance_func(x):
    global counter
    mu=fabs(x[0])
    alpha=fabs(x[1])
    d1=fabs(x[2])
    gi=fabs(x[3])
    ki=fabs(x[4])
    ti=fabs(x[5])
    mdb.models[model_name].materials[material_name].hyperelastic.
        setValues(table=((mu, alpha, d1), ))
    mdb.models[model_name].materials[material_name].viscoelastic.
        setValues(domain=TIME, time=PRONY, table=((gi, ki, ti), ))
    job = mdb.Job(name=job_name_prefix+str(counter), model=model_name,
        numCpus=4, numDomains=4,)
    mdb.jobs[job_name_prefix+str(counter)].submit()
    mdb.jobs[job_name_prefix+str(counter)].waitForCompletion()
```

```
    mdb.save()
    print('Job'+str(counter)+'done')
    odb=openOdb(path=file_path+file_name_prefix+str(counter)+'.odb',
        readOnly = True)
    counter=counter+1
    vari=0
    for i in range(200):
        current_frame = odb.steps['Step-1'].frames[i]
        reaction_force=current_frame.fieldOutputs['RF']
        nodepos = odb.rootAssembly.instances['PART-2'].nodes[node_number
            ]
        node_reaction_force = reaction_force.getSubset(region=nodepos)
        node_values = node_reaction_force.values
        v = node_values[0]
        vari=vari+fabs(v.data[1]-exp_data[i])
    for i in range(100):
        current_frame = odb.steps['Step-2'].frames[i+1]
        reaction_force=current_frame.fieldOutputs['RF']
        nodepos = odb.rootAssembly.instances['PART-2'].nodes[node_number
            ]
        node_reaction_force = reaction_force.getSubset(region=nodepos)
        node_values = node_reaction_force.values
        v = node_values[0]
        #disp_sublist.append(v.data[1])
        vari=vari+fabs(v.data[1]-exp_data[i+200])
    odb.close()
    report_file=open(report_file_name,'a')
    report_file.write(str(mu)+'\t'+str(alpha)+'\t'+str(d1)+'\t'+str(gi)+
        '\t'+str(ki)+'\t'+str(ti)+'\t'+str(vari)+'\n')#+'\t'+str(gi)+'\t
        '+str(ki)+'\t'+str(ti)+'\t'
    report_file.close()
    return vari;

def nelder_mead(f, x_start,
                step=0.1, no_improve_thr=10e-6,
```

```
                no_improv_break=10, max_iter=0,
                alpha=1., gamma=2., rho=-0.5, sigma=0.5):
    '''
        @param f (function): function to optimize
        @param x_start (numpy array): initial position
        @param step (float): look-around radius in initial step
        @no_improv_thr,  no_improv_break (float, int): break after
            no_improv_break iterations with an improvement lower than
            no_improv_thr
        @max_iter (int): always break after this number of iterations.
            Set it to 0 to loop indefinitely.
        @alpha, gamma, rho, sigma: parameters of the algorithm (see
            Wikipedia page for reference) return: tuple (best parameter
            array, best score)
    '''

    # initialization
    dim = len(x_start)
    prev_best = f(x_start)
    no_improv = 0
    res = [[x_start, prev_best]]

    for i in range(dim):
        x = copy.copy(x_start)
        x[i] = x[i] + step
        score = f(x)
        res.append([x, score])

    # simplex iter
    iters = 0
    while 1:
        # order
        res.sort(key=lambda x: x[1])
        best = res[0][1]
```

```
# break after max_iter
if max_iter and iters >= max_iter:
    return res[0]
iters += 1

# break after no_improv_break iterations with no improvement
print '... best so far:', best

if best < prev_best - no_improve_thr:
    no_improv = 0
    prev_best = best
else:
    no_improv += 1

if no_improv >= no_improv_break:
    return res[0]

# centroid
x0 = [0.] * dim
for tup in res[:-1]:
    for i, c in enumerate(tup[0]):
        x0[i] += c / (len(res)-1)

# reflection
xr = x0 + alpha*(x0 - res[-1][0])
rscore = f(xr)
if res[0][1] <= rscore < res[-2][1]:
    del res[-1]
    res.append([xr, rscore])
    continue

# expansion
if rscore < res[0][1]:
    xe = x0 + gamma*(x0 - res[-1][0])
    escore = f(xe)
```

```
            if escore < rscore:
                del res[-1]
                res.append([xe, escore])
                continue
            else:
                del res[-1]
                res.append([xr, rscore])
                continue

        # contraction
        xc = x0 + rho*(x0 - res[-1][0])
        cscore = f(xc)
        if cscore < res[-1][1]:
            del res[-1]
            res.append([xc, cscore])
            continue

        # reduction
        x1 = res[0][0]
        nres = []
        for tup in res:
            redx = x1 + sigma*(tup[0] - x1)
            score = f(redx)
            nres.append([redx, score])
        res = nres

#bnds = array([[0.01, 0.4], [0.2, 10]], dtype=float)
#x_max = minimize(variance_func,initial_parameters, method='SLSQP',
    bounds=bnds, options={'disp':True, 'ftol':10})
x_max = nelder_mead(variance_func,initial_parameters)
report_file=open(report_file_name,'a')
report_file.write(str(x_max))
report_file.close()
#print x_max
mdb.close()
```

End (optim.py)

Appendix D

Kalman Filter Implementation with Matlab Code

The following Matlab code is employed for parameter identification based on the Kalman filter.

Begin (kalman.m)

```
clear all;
clc;
dataproc_fine_r4;
%gradient
for i=1:200
    clc
    i
    [t(i).gradian.alpha,t(i).gradian.mu]=gradient(t(i).f,5/(200-1)
        ,0.3/(200-1));
end
x(1).alpha=8;
x(1).mu=0.8;
P(1).cov=[25 0;0 0.09];
Rt=0.1;
for i=1:199
    i
    if x(i).alpha>11
```

```
        x(i).alpha=11;
    end
    if x(i).mu>0.8
        x(i).mu=0.8;
    end
    if x(i).alpha<6
        x(i).alpha=6;
    end
    if x(i).mu<0.5
        x(i).mu=0.5;
    end
    delta=[griddata(t(i).alpha,t(i).mu,t(i).gradian.alpha,x(i).alpha,x(i
        ).mu,'cubic'), griddata(t(i).alpha,t(i).mu,t(i).gradian.mu,x(i).
        alpha,x(i).mu,'cubic')];
    P(i+1).cov=P(i).cov-P(i).cov*delta'*((delta*P(i).cov*delta'+Rt)^(-1)
        )*delta*P(i).cov;
    K(i+1).t=P(i+1).cov*delta'*(1/Rt);
    x(i+1).alpha=x(i).alpha+K(i+1).t(1)*[exp_data_r4(i)-griddata(t(i).
        alpha,t(i).mu,t(i).f,x(i).alpha,x(i).mu,'cubic')];
    x(i+1).mu=x(i).mu+K(i+1).t(2)*[exp_data_r4(i)-griddata(t(i).alpha,t(
        i).mu,t(i).f,x(i).alpha,x(i).mu,'cubic')];
    alpha_out(i)= x(i+1).alpha;
    mu_out(i)=x(i+1).mu;
end
```

End (kalman.m)

Appendix E

MATLAB Code for PID Parameter Optimization

Begin (run.m)

```
pid0 = [3.0 10 0.1 1.0];
a1 = 1; a2 = 23.4;
options = optimset('Display', 'iter-detailed','MaxFunEvals', 1000, 'TolX
    ', 0.001, 'TolFun', 0.001);
pid = fmincon(@tracklsq, pid0, [], [], [], [], [0 0 0 0], [],
    @constraint, options)
```

End (run.m)

Begin (constraint.m)

```
function [c,ceq] = constraint(pid)
assignin('base', 'kp', pid(1));
assignin('base', 'ki', pid(2));
assignin('base', 'kd', pid(3));
assignin('base', 'kn', pid(4));
simopt = simset('solver','ode14x');
[~,~,yout] = sim('ident_model',[0 10],simopt);
c(1)=0; %input signal
c(2)=0; %overshoot
c(3)=0; %undershoot
```

```
os_flag=0;
for i = 1:1001
    if abs(yout(i,2))>c(1)
        c(1)=abs(yout(i,2));
    end
end

for i = 1:1001%overshoot
    if (yout(i,1)-1)>0
        if os_flag==0
            os_flag=i;
        end
        if (yout(i,1)-1)>c(2)
            c(2)=yout(i,1)-1;
        end
    end
end

if os_flag==0
    os_flag=1;
end

for i = os_flag:1001 %undershoot
    if (yout(i,1)-1)<0 %undershoot
        if (1-yout(i,1))>c(3)
            c(3)=1-yout(i,1);
        end
    end
end

c(1)=c(1)-5.0; %volts
c(2)=abs(c(2)-0.05); %mm
c(3)=abs(c(3)-0.05); %mm
ceq=[];
end
```

End (constraint.m)

Begin (tracklsq.m)

```
function F = tracklsq(pid)
assignin('base', 'kp', pid(1));
assignin('base', 'ki', pid(2));
assignin('base', 'kd', pid(3));
assignin('base', 'kn', pid(4));
simopt = simset('solver','ode14x');
[~,~,yout] = sim('ident_model',[0  10],simopt);
F = 0;
for i = 1:1001
    F = F+(abs(yout(i,1)-1));
end
end
```

End (tracklsq.m)